ABSTRACT

Title of dissertation: EVALUATING OCEANOGRAPHIC HYPOTHESES: THREE METHODS FOR TESTING IDEAS

Benjamin K. Johnson
Doctor of Philosophy, 2020

Dissertation directed by: Professor Eugenia Kalnay, Chair
Professor Jacob Wenegrat, Co-Chair
Department of Atmospheric and Oceanic Science

The disciplines of meteorology and oceanography are both vital to understanding the earth system. Throughout most of the last half century, meteorology has largely been a prognostic discipline. Forecasts made by meteorologists have been widely used and scrutinized, allowing for countless opportunities to test and improve ideas about atmospheric circulation and physics. Since weather forecasts involve integrating numerical models and updating the model state via data assimilation, forecasting demands frequent use of the principles of Bayesian inference. This requirement essentially confronts the physics contained within numerical models at recurring intervals and can reveal systematic model bias.

In contrast, prognostic applications have been less prevalent in oceanography. Oceanographic forecasts are much rarer than atmospheric forecasts and, perhaps as a consequence of this disparity, many ideas concerning oceanic circulation have not been tested to the same degree as ideas concerning atmospheric circulation. This dissertation presents three methods for testing oceanographic ideas: applying common methodologies to analogous regions of different ocean basins; creating synthetic time series to mimic the properties of oceanographic time series in order to construct null distributions for hypothesis testing; and using water mass census information to interpret the results of water mass transformation analysis.

EVALUATING OCEANOGRAPHIC HYPOTHESES: THREE METHODS FOR TESTING IDEAS

by

Benjamin K. Johnson

Dissertation submitted to the Faculty of the Graduate School of the
University of Maryland, College Park in partial fulfillment
of the requirements for the degree of
Doctor of Philosophy
2020

Advisory Committee:

Professor Eugenia Kalnay (Chair)
Dr. Frank Bryan (Special Member)
Professor Michael Evans (Dean's Representative)
Professor Brian Hunt
Professor Jonathan Poterjoy
Professor Jacob Wenegrat (Co-Chair)

© Copyright by
Benjamin K. Johnson
2020

Dedication
To my teachers

Acknowledgments

This dissertation would not have been possible without the education and encouragement provided by my teachers: Melvin Nakao, Michelle Fragas, Joy Hirayama, Lynda Usui, Kathy Herring, Yoko Shimana, Laura Yokoyama, Vicki Kloetzel, Peter Wagner, William Stephenson, Gladys Miura, Melvin Kaetsu, Dane Nelson, Bill McMahon, Richard Mortemore, Don Memmer, Helen Nakamura, Debra Yamamoto, Joell Kerr, Art and Rene Kimura, Robert Holt, Ipolani Wright, Erin Niezman, Lynn Del Rosario, Lorrin Chock, Erin Williams, Kathryn Crayton-Shay, Cathy Ikeda, Diana Morales, Karen Chang, Sharon Iwasaki, Janet Luh, Joanne Berryman, Faye Shiroma, Jerry Quist, Lisa Soares, Joy Ito-Carver, Tana Rosehill & Jeanette Wong. The lessons I learned from you have been invaluable in my development as a scientist.

This work was enabled by a university large allocation award of 2.3 million core hours on the Yellowstone Supercomputing Resource (ark:/85065/d7wd3xhc) provided by the Computational and Information Systems Laboratory (CISL) of the National Center for Atmospheric Research (NCAR), which is sponsored by the National Science Foundation (NSF). Thank you to the developers of the Community Earth System Model (CESM), the Parallel Ocean Program 2 (POP2), the Community Ice CodE 4 (CICE4), the CISL staff and David Bailey for your assistance with the integration.

Thank you to my family for your unwavering support: my grandparents, mother, Aunty Kay, Uncle David, Aunty Deedee, Corey, Laine, Stephen, Trisha & Jodi. I am sorry I have missed so much at home. Thank you Katy for believing in me – I can't fathom how this would've turned out had we never met.

Thank you to the writers who have taught me that certain truths are timeless and that the key to creating works of lasting importance is to seek them out – E.T. Jaynes, Vic Ketchman, Michael S. McCartney, Alejandro Orsi and Daniel S. Wilks.

To my committee – Dr. Frank Bryan, Professor Michael Evans, Professor Brian Hunt, Professor Eugenia Kalnay, Professor Jonathan Poterjoy & Professor Jacob Wenegrat – thank you for serving and for providing a rigorous critique of my research.

Thank you to my research mentors over the years: Mike Mendez of Northrop Grumman, Professors Stephen Elkin, Daniel Kirk-Davidoff and Oscar W. Greenberg of the University of Maryland (UMD), and Dr. Isaac Held of the Geophysical Fluid Dynamics Laboratory.

Thank you to the Physics faculty at UMD for an excellent education. I often reminisce in appreciation for the rigor and wonder that is emphasized by the undergraduate curriculum. Thank you to Professor Markus Luty (now at the University of California at Davis) for inspiring me to switch majors. Thank you to the instructors of the laboratory courses – Professors Elizabeth Beise, Carter Hall, Sarah Eno & Richard Greene. While theory is a critical part of an education, the laboratory courses were an illuminating exercise in the basics of conducting research. Thank you especially to Tom Gleason for your efforts to enable me to successfully complete my degree.

Thank you to the Atmospheric & Oceanic Science faculty, particularly Professors Kalnay, Kousky and Nigam, for your instruction. Thank you James Carton & Semyon Grodsky for providing me the opportunity to work on the salinity project. Thank you Sonja Junek, June Sherer, Bernadette Gatewood, Tammy Paolino & Tameka Jones for your administrative support and Dave Yanuk, James Crawford, José Cáceres & Jeff Henrikson for your technical support. Thank you especially to Tammy Hendershot for your tireless care – beyond helping me to survive, I hope you see me thrive.

Thank you Professor Ruoying He at North Carolina State University for enabling me to continue research while this situation at Maryland was resolved and to Jasen Jacobsen and Jeff Willison for being dutiful scholars with me during my time in Raleigh. Thank you to my brothers in arms in dissertation writing: Corey Johnson, Byron Kilbourne & Goutham Ganesan. Kudos especially to Goutham for completing both an MD and a PhD in less time than it took for me to defend a PhD.

Thank you to my hiring committee at NCAR – Mohamad El Gharamti, Jeffrey Anderson and Timothy Hoar – for giving me a job I love, one that gives me the opportunity to help others and to do meaningful work. It is difficult for me to express the enthusiasm and gratitude I have for the opportunity to work with you. Finally, thank you again to Frank Bryan: I would not have been able to complete this without your guidance – I will emulate your generosity throughout my career.

Contents

Dedication **ii**

Acknowledgements **iii**

Contents **v**

List of Tables **ix**

List of Figures **xii**

List of Acronyms **xxv**

Introduction **1**

1 Climatological Annual Cycle of the Salinity Budgets of the Subtropical Maxima **4**

1.1 Abstract 4

1.2 Introduction 5

1.3 Background 6

1.4 Numerical Experiment and Results 10

1.4.1 Model description 10

1.4.2 Model experiment 10

1.4.3 Model analysis 11

1.4.4 Model Results and Discussion 12
1.5 Argo Float Selection and Analysis 23
1.5.1 Float Selection and Methodology 23
1.5.2 Argo Results 23
1.6 Summary and Conclusions 26
1.7 Chapter Acknowledgements 28

2 Salinity Budget of the Equatorial Pacific Salinity Minimum 29

2.1 Abstract 29
2.2 Introduction 29
2.3 Results 31
2.3.1 Climatological Simulation of the Eastern Pacific Fresh Pool 31
2.3.2 Salinity Budget of the Eastern Pacific Fresh Pool 31
2.4 Discussion 36

3 Hypothesis Testing and Climate Change: Four Complications (and How to Account for Three of Them) 37

3.1 Abstract 37
3.2 Introduction 38
3.3 Background 40
3.3.1 Hypothesis Testing 40
3.3.2 Synthetic-Data Time Series 41
3.3.3 Complications 43
3.3.4 Temperature and Salinity Data 47
3.3.5 Multiple Testing (Field Significance) 49
3.3.6 Model Misspecification 53
3.4 An Example Test for Difference of Means 55

3.5 Discussion 59
3.6 Chapter Acknowledgements 63

4 Combining Water Mass Census and Transformation in θ-S Coordinates: an Illustration in the Southern Ocean 64

4.1 Abstract 64
4.2 Introduction 65
4.3 Southern Ocean State Estimate (SOSE) Model Configuration 68
4.4 Background on Fronts, Surface Zones, and Water Masses 68
  4.4.1 Fronts and Surface Zones 69
  4.4.2 Relevant Water Masses 72
4.5 Methodology 74
  4.5.1 $\theta - S$ censuses 74
  4.5.2 Criteria for Distinguishing each Water Mass 75
  4.5.3 Transformations 76
4.6 Results 80
  4.6.1 Census Results 80
  4.6.2 Transformation Results 89
4.7 Discussion 91
  4.7.1 Water Mass Transformations 92
  4.7.2 Surface Fluxes 99
  4.7.3 Misconceptions about the Southern Ocean 99
4.8 Summary 102
4.9 Chapter Acknowledgements 103

Overview and Prospects for Future Research 104

A Experiment Setup **106**

A.1 Community Earth System Model 106

A.2 Forcing Fields and Availability 107

A.3 POP2 Namelists Groups, Options and Values 109

Bibliography **123**

List of Tables

1.1 Isohaline, in practical salinity units (psu), bounding each salinity maxima (S$_{max}$). . 5

1.2 Climatological annual mean magnitude of each budget term and the percent of evaporation minus precipitation (E-P) balanced by each of the remaining budget terms (Sverdrups (Sv) psu). Since the mean advection term should vanish from Eq. 1.7 it provides an estimate of the error in Eq. 1.8. We include its magnitude as an error estimate in the rightmost column. 16

1.3 The Float ID #s and data duration for the Argo data include in Section 1.5. Each float provides 73 profiles (approximately 2 years) of data within the eastward and poleward region of each S$_{max}$. 24

3.1 False Discovery Rate levels (α_{FDR}), the corresponding level of the global test (α_{global}), and the number of grid points for surface salinity and temperature fields falling below each threshold. 62

4.1 Density range for Circumpolar Deep Water (CDW) and its variants in water mass transformation studies. Note well: Sloyan and Rintoul (2001b) supplement their density calculations using $\theta - S$ composition and conclude that CDW is transformed into Antarctic Surface Water (AASW) which then is transformed into Antarctic Intermediate Water (AAIW). 92

4.2 Studies which replicate Fig. 8 of Speer et al. (2000). 101

A.1 The variables and data sources incorporated into the Coordinated Ocean-Ice Reference Experiments (CORE)v2 data set. This is a modified version of Table 1 of Large and Yeager (2009) updated to reflect the extension of the dataset (Griffies et al., 2012). . 108

A.2 The forcing fields used in the simulation with their temporal availability and units. This information is a truncated form of Table 1 of Griffies et al. (2012). 108

A.3 Domain Namelist Group 109

A.4 IO Namelist Group 110

A.5 Time_manager Namelist Group 110

A.6 Grid Namelist Group 111

A.7 Init_ts Namelist Group 111

A.8 Diagnostics Namelist Group 112

A.9 Budget_diagnostics Namelist Group 112

A.10 Bsf_diagnostic Namelist Group 112

A.11 Restart Namelist Group 112

A.12 Tavg Namelist Group 113

A.13 History Namelist Group 113

A.14 Movie Namelist Group 113

A.15 Solvers Namelist Group 114

A.16 Vertical_mix Namelist Group 114

A.17 Vmix_const Namelist Group 114

A.18 Vmix_rich Namelist Group 114

A.19 Tidal Namelist Group 114

A.20 Vmix_kpp Namelist Group 115

A.21 Advect Namelist Group 115

A.22 Hmix Namelist Group 115

A.23 Hmix_del2u Namelist Group 115

A.24 Hmix_del2t Namelist Group 115

A.25 Hmix_del4u Namelist Group 116

A.26 Hmix_del4t Namelist Group 116

A.27 Hmix_gm Namelist Group 116

A.28 Mix_submeso Namelist Group 116

A.29 Hmix_aniso Namelist Group 117

A.30 State Namelist Group 117

A.31 Baroclinic Namelist Group 117

A.32 Ice Namelist Group 117

A.33 Pressure_grad Namelist Group 118

A.34 Topostress Namelist Group 118

A.35 Forcing_ws Namelist Group 118

A.36 Forcing_shf Namelist Group 118

A.37 Forcing_sfwf Namelist Group 119

A.38 Forcing_pt_interior Namelist Group 119

A.39 Forcing_s_interior Namelist Group 120

A.40 Forcing_ap Namelist Group 120

A.41 Coupled Namelist Group 120

A.42 Sw_absorption Namelist Group 120

A.43 Transports Namelist Group 121

A.44 Context Namelist Group 121

A.45 Overflows Namelist Group 121

A.46 Niw Namelist Group 121

A.47 Passive_tracers_on Namelist Group 122

A.48 Iage Namelist Group 122

List of Figures

1.1 A schematic of an open-ocean S$_{max}$. Solid lines represent isohaline contours, with contour thickness representing salinity. The dark (light) shaded region depicts that in the mixed layer eastward & poleward (westward & equatorward) of the surface layer salinity (SLS) max ∂_z S is stabilizing (destabilizing) due to the displacement of subtropical underwater (STUW) with respect to the SLS maximum. 7

1.2 The climatological annual cycle of surface heat flux (W/m^2) over each S$_{max}$ in CESM. The x-axis is offset by six months for the Southern Hemisphere (SH) S$_{max}$ (top x-axis labels) with respect to the Northern Hemisphere (NH) S$_{max}$ (bottom x-axis labels) to account for the hemispheric phase shift of the seasons. 8

1.3 The model climatological mean SLS. Black contours are the mean position of isohaline surface outcrops for each S$_{max}$. Gray contours are isohalines at 100m depth. Each of the open-ocean S$_{max}$ contours at 100m depth is positioned westward and equatorward of the surface outcrop. The North Indian (NI) S$_{max}$ surface and 100m contours are at roughly the same position. White lines depict transects along which depth profiles are shown in Figs. 1.8 & 1.9. 13

1.4 The annual cycle of outcrop extent anomaly (m^2) from annual mean value for CESM (black) and Monthly Isopycnal & Mixed-layer Ocean Climatology (MIMOC) (light blue). 14

1.5 Model climatological mean SLS (psu, shaded) and comparison of climatological mean S_{max} outcrops of the integration (black contours) and MIMOC (light blue). In all cases, with the exception of North Pacific (NP) S_{max}, the MIMOC outcrops are larger, with the largest discrepancy in South Pacific (SP) S_{max}, where MIMOC outcrop area is nearly double that of the model. The white paths along the eastward and poleward edges of each MIMOC outcrop are the position of the Argo floats over the two-year periods described in Section 1.5. 15

1.6 The climatological annual cycle of the salinity budget (Sv psu) for each S_{max}. The net flux term is the sum of horizontal diffusion, eddy advection, and vertical diffusion. 17

1.7 The simulation's climatological mean vertical diffusive flux of salt though the base of the mixed layer (psu m/s, shaded). Black and gray contours are isohaline contours as in Fig. 1.3. Light blue contours are regions where salt finger convection penetrates the base of the mixed layer. In the vicinity of the S_{max} these regions of salt finger convection are on the eastward and poleward edges of each S_{max} & correspond with regions of negative vertical diffusive salt fluxes through the mixed layer base (magenta shaded regions). 18

1.8 Transect plots through each NH S_{max} along the paths shown in Fig. 1.3. Climatological January PV ($m^{-1}s^{-1}$, shaded), isohaline bounding each S_{max} (white contours) and volumes where $|PV| < 3.0\times10^{-10}m^{-1}s^{-1}$ (magenta). Climatological mixed layer depth for January, March and May is shown by mustard yellow contours ranging from dark/thick to light/thin. Climatological areas of salt finger convection for January, March and May are shown by blue contours ranging from dark/thick to light/thin. . 20

1.9 Transect plots through each SH S_{max} along the paths shown in Fig. 1.3. Climatological July PV ($m^{-1}s^{-1}$, shaded), isohaline bounding each S_{max} (white contours) and volumes where $|PV| < 3.0 \times 10^{-10}m^{-1}s^{-1}$ (magenta). Climatological mixed layer depth for July, September and November is shown by mustard yellow contours ranging from dark/thick to light/thin. Climatological areas of salt finger convection for July, September and November are shown by blue contours ranging from dark/thick to light/thin. 21

1.10 A simplified schematic of the seasonal deepening of the mixed layer. The solid lines depict isohaline contours. Dashed-dotted lines surrounding the white volumes depict low-PV layers. Dotted lines surrounding dark gray volumes depict areas of salt finger convection. 22

1.11 73 depth profiles from each of the Argo floats with data durations listed in Table 1.3. Depths where $|PV| < 3.0 \times 10^{-10}m^{-1}s^{-1}$ depicted in magenta. Salt finger convection diffusivity as estimated by 1.2 (blue shading). Depth of the mixed layer depicted in mustard yellow. 25

2.1 (a) Climatological model SLS (shaded, psu) and mean 34.0 psu contours for the simulation (black) and MIMOC (light blue). (b) Surface area bound by each of the outcrops in (a) as a function of month. 32

2.2 Annual cycle of surface flux (shaded, psu m/s) with isohaline contours in purple (psu) and isotherms in black (°C). 33

2.3 Annual cycle of SSH anomaly (shaded, cm) with surface velocity vectors (cm/s) and isohaline contours (purple, psu). 33

2.4 The annual cycle of salt budget terms (Sv psu) of the salinity budget volume-averaged within the 34.0 isohaline contour computed on 5-day data and averaged into monthly means (dashed lines) and computed on climatological monthly mean data (solid lines). 34

2.5 The seasonal mean patterns of vertical diffusive flux through the base of the mixed layer (shaded, psu×m/s). Seasonal mean isohalines in purple and seasonal mean mixed layer depth in mustard. 35

2.6 The annual cycle of vertical diffusion (shaded, psu/s) as a function of depth at 10°N and 100°W (depicted by the black marker in Fig. 2.5). Isohaline contours in purple, mixed layer depth in mustard. 36

3.1 An example parametric probability distribution function, where the curve is specified by the Gaussian distribution. The shaded regions on each tail of the distribution indicate the regions where observing a test statistic would exceed the test level $\alpha = 0.05$. 42

3.2 The elements of synthetic data times series and samples taken from it. A) A parametric probability distribution (dashed black line), representing the parent distribution, from which the values in the time series are drawn with $\mu = 0$ and $\sigma = 1$. B) A histogram (solid blue fill) of 10,000 values drawn from the parent distribution. C) A time series (solid blue line) constructed from the values in (B). Only the first 100 values are shown although the time series consists of all 10,000 values from (B). D) Sample means (horizontal sky blue lines) sampled from the time series, with the averaging period N=10. The first 10 sample means are depicted but 1000 samples, spanning the entirety of the time series are collected. E) A histogram of the 1000 sample means (sky blue fill) drawn from the time series. This distribution is known as the sample distribution of the sample mean. F) A parametric distribution (dashed orange line) meant to approximate the shape of the sample distribution of the sample mean where $s = \sigma/\sqrt{N}$. This parametric distribution does not match the shape of the sample distribution in (E) because the time series exhibits autocorrelation. 44

3.3 Each row contains a condensed version of the elements depicted in Fig. 3.2. In the left column the parametric parent distribution (dashed black line) is overlaid atop the histogram of values drawn from it (solid blue fill). In the middle column, the first 100 values of time series (solid blue lines) constructed from the histograms in the left columns are depicted along with the first 10 sample means (horizontal sky blue lines) sampled from each of the time series. Each of these sets of time series and samples consists of 10,000 observations and 1,000 sample means even though not all of these are shown. The right column shows the histogram of sample means drawn from each time series (solid sky blue fill) and parametric distributions used to estimate the shape of the sample distribution where the variance of the distribution is specified assuming $s^2 = \sigma^2/N$ (dashed orange curve) and $s^2 = V\sigma^2/N$ (dashed vermilion curve). The lag-1 autocorrelation of the time series is different for each row where in A it equals 0.0, in B it equals 0.25, in C it equals 0.5 and in D it equals 0.75. 46

3.4 A time series with measurement error and its effect on the sample distribution. A) parent distribution (dashed black line) overlaid atop the histogram of values drawn from it (solid blue fill). B) The first 100 values of the time series (solid blue lines) constructed from the histograms in the left columns, depicted along with the first 10 sample means (horizontal sky blue lines) sampled from the time series. The magnitude of measurement error is depicted using vertical lines extending from each observation (solid reddish-purple lines). A random draw from the error distribution is collected for each observation and a second set of sample means (horizontal yellow lines) are sampled to account for the effect of measurement error. Each of these sets of time series and samples consists of 10,000 observations and 1,000 sample means even though not all of these are shown. C) The histogram of sample means drawn from the time series (solid sky blue fill) and the histogram of sample means drawn from the time series after random errors have been added to each observation (solid yellow fill). Dashed curves depict parametric distributions used to estimate the shape of the sample distribution where the variance of the distribution is specified assuming $s^2 = \sigma^2/N$ (dashed orange curve), $s^2 = V\sigma^2/N$ (dashed vermilion curve), and $s^2 = V\sigma^2/N + s_\epsilon^2$ (dashed bluish-green curve). 48

3.5 Three parametric distributions from Fig. 3.4C where the variance of each distribution is estimated using $s^2 = \sigma^2/N$ (dashed orange curve), $s^2 = V\sigma^2/N$ (accounting for autocorrelation; dashed vermilion curve), $s^2 = V\sigma^2/N + s_\epsilon^2$ (accounting for autocorrelation and measurement error dashed bluish-green curve). The filled regions beneath each dashed curve correspond to the regions that an observed test statistic would be rejected at the $\alpha = 0.05$ level. Incorrectly applying the threshold for the orange distribution for data represented by the bluish-green distribution results in an effective level of $\alpha = 0.3$. 48

3.6 The mean SLS field and the mean uncertainty of the Hadley EN4.2.1 dataset. The black and white dots in each panel correspond to regions of high and low interannual variability of SLS, respectively. Time series taken from these points are shown in Fig. 3.8. 49

3.7 The mean sea surface temperature (SST) field and the mean uncertainty of the Hadley EN4.2.1 dataset. The black and white dots in each panel correspond to regions of high and low interannual variability of SST, respectively. Time series taken from these points are shown in Fig. 3.9. 50

3.8 Time series of annual mean SLS values (solid blue line) and measurement error (solid reddish-purple lines) from two different points in the Hadley EN4.2.1 dataset. A) Region of high interannual variability in SLS. B) Region of low interannual variability in SLS. In both cases the magnitude of error is comparable to the magnitude of interannual variability. 51

3.9 Time series of annual mean SST values (solid blue line) and measurement error (solid reddish-purple lines) from two different points in the Hadley EN4.2.1 dataset. A) Region of high interannual variability in SST. B) Region of low interannual variability in SST. As with SLS, in both cases the magnitude of error is comparable to the magnitude of interannual variability. 52

3.10 Results of applying the Harvey-Collier model misspecification test (p-values, shaded) to annual means of salinity and temperature in the Hadley EN4.2.1 data set. 55

3.11 Regions of significant differences of observed SLS, following the methodology of Hosoda et al. (2009), evaluated at $\alpha = 0.05$. A) Shaded areas (solid orange fill) correspond to regions where a t-test infers significant change in SLS when $s^2 = \sigma^2/N$. B) Shaded areas (solid vermilion fill) correspond to regions where a t-test infers significant change in SLS when $s^2 = V\sigma^2/N$. C) Shaded areas (solid bluish-green fill) correspond to regions where a t-test infers significant change in SLS when $s^2 = \sigma^2/N + s_\epsilon^2$. D) The result of applying the false discovery rate (FDR) test to infer regions of significant change in SLS after accounting for autocorrelation and measurement error. No grid points are highlighted. 57

3.12 Regions of significant differences of observed SST, following the methodology of Hosoda et al. (2009), evaluated at $\alpha = 0.05$. A) Shaded areas (solid orange fill) correspond to regions where a t-test infers significant change in SST when $s^2 = \sigma^2/N$. B) Shaded areas (solid vermilion fill) correspond to regions where a t-test infers significant change in SST when $s^2 = V\sigma^2/N$. C) Shaded areas (solid bluish-green fill) correspond to regions where a t-test infers significant change in SST when $s^2 = \sigma^2/N + s_\epsilon^2$. D) The result of applying the FDR test to infer regions of significant change in SST after accounting for autocorrelation and measurement error. No grid points are highlighted. 58

3.13 A) Sorted p_i values from the difference of mean test on SLS data, as depicted in Fig. 3.11 (shaded curve). Dotted lines indicate various FDR thresholds where α_{FDR}= 0.1, 0.2, ... 1.0. B) A map of the corresponding α_{FDR} thresholds that each grid point falls below. 61

3.14 A) Sorted p_i values from the difference of mean test on SST data, as depicted in Fig. 3.12 (shaded curve). Dotted lines indicate various FDR thresholds where α_{FDR}= 0.1, 0.2, ... 1.0. B) A map of the corresponding α_{FDR} thresholds that each grid point falls below. 62

4.1 A depiction of the water mass transformation framework applied to the potential density field. Dotted lines represent isopycnal surfaces through which water can be transformed either by surface fluxes or subsurface diabatic mixing. 66

4.2 A) The mean surface salinity field (g/kg; shaded) for years 2005-2010 from SOSE (Mazloff et al., 2010) and climatological positions of the four Southern Ocean fronts from (Orsi et al., 1995). The fronts, from north to south: Subtropical Front (STF) (black dashed line), Subantarctic Front (SAF) (white solid line), Polar Front (PF) (black solid line), and Southern Antarctic Circumpolar Current Front (sACCF) (white dashed line). B) Same as A except showing the mean surface θ field (°C; shaded). C) The surface zone masks delineated by the fronts of the ACC (shaded according to the colorbar above the panel). The extent of each mask is used to assign each surface grid point into a specific zone when conducting the $\theta - S$ census. 71

4.3 A) $\theta - S$ surface area census of the zones depicted in Fig. 4.2C (m^2, shaded for each section according to the corresponding color bar at the right of the panel). Solid contours outline the 90% surface area contour of each surface zone as described in Section 4.5.1. B) $\theta - S$ volume census of the SOSE domain (m^3, shaded $\log_{10}$ scale). Dashed contours outline the 90% volume contour of three water masses (Subantarctic Mode Water (SAMW), AAIW, CDW) as described in Section 4.5.1. Since the 26.5-27.1σ_θ density range is typically used to delineate the SAMW density class, the corresponding isopycnals are drawn in a heavier weight within the θ-S diagrams. . . 81

4.4 These figures depict mode water extent and the range of surface fluxes caused by the formation and melting of sea ice. A) Mean vertically integrated mode water volume (10^{10}m^3) where the mode water extent is delineated by the SAMW density range (26.5-27.1 σ_θ) and by the potential vorticity threshold $|PV| \leq 3.0 \times 10^{-10} m^{-1} s^{-1}$ (shaded in blue). We exclude the upper 100m from the integral so as to exclude the surface mixed layer. Also shown is sea ice redistribution freshwater flux (m/year) where negative flux due to brine rejection is shaded in magenta and positive flux due to ice melt is shaded in green. The climatological positions of the Southern Ocean fronts are the same as in Fig. 4.2. B) The same mean vertically integrated mode water volume except we use the Turner angle to partition the mode water into two different volumes in order to highlight the extent of waters with unstable vertical gradient of salinity (10^{10}m^3; shaded in bluish-green) and unstable vertical gradient of temperature (10^{10}m^3; shaded in orange). 83

4.5 The mean surface $\theta - S$ composition along the A12/S2, SR3 and P19 transects where each marker is the average along a given transect within a surface zone in February 2005 (star markers) and September 2005 (triangle markers). The coloring of each marker corresponds to the surface zone within which the mean is computed and the winter and summer markers for each zone are connected by a dotted line. Each winter marker is annotated with the name of the transect. The solid and dashed sector contours for the surface zones and water masses are the same as in Fig. 4.3. The subtropical markers for the A12/S2 and P19 transects are all warmer than 16°C and thus exceed the θ limit for the figure. 84

4.6 Latitude-depth transects along 7°E (approximating the track of the World Ocean Circulation Experiment (WOCE) A12/S2 meridional section) for February 2005 (left column) and September 2005 (right column) for S (g/kg; top row), θ (°C; middle row), and PV ($m^{-1}s^{-1}$; bottom row). Climatological positions of the Southern Ocean fronts depicted by vertical lines: STF (dashed black), SAF (solid white), PF (solid black) and sACCF (dashed white). Gray contours are SAMW density class isopycnals (26.5 and 27.1 σ_θ). Dashed gray contour denotes the extent of CDW, dashed reddish-purple contour denotes the extent of AAIW, dashed bluish-green contour denotes the extent of SAMW with unstable vertical salinity gradient. 85

4.7 Latitude-depth transects along 145°E (approximating the track of the the WOCE SR3 meridional section). Contours and shading same as in Fig. 4.6 with an additional contour: dashed orange contour denotes the extent of SAMW with unstable vertical temperature gradient. 86

4.8 Latitude-depth transects along 89°W – approximating the track of the AAIW05 cruise (Chereskin, 2005) transect along the WOCE P19 meridional section. Contours and shading same as in Fig. 4.7. There is low-stability water that would be classified as a mode water using the low-PV criteria near the PF but it is not outlined with an SAMW contour in these panels because its density (approximately 27.2-27.3 σ_θ) lies beyond the SAMW density range used throughout this study. Comparing the September PV transect in E to the contemporaneous transects observed during AAIW05 (Hartin et al., 2011) reveals a discrepancy in the location of the deep near-surface low-PV layer in SOSE. The deepest penetration of low-PV water in SOSE is centered poleward of the polar front at roughly 62°S while the deep near-surface low-PV layer observed during the same time period during the AAIW05 Cruise was centered equatorward of the PF at roughly 57°S (Fig. 2a of Hartin et al. 2011). 87

4.9 Number of months that water matching the $\theta - S$ composition of AAIW was detected at each surface grid point (shaded, out of a possible 60 total months). The shading was created by iterating through each surface grid point at each time step and checking whether the $\theta - S$ composition of the surface was within the overlapping Subantarctic Zone and AAIW sectors in the $\theta - S$ plane. 89

4.10 $T(\theta, S)$ surface transformations (in Sverdrups [Sv]; left column) and the resulting $F(\theta, S)$ formations (Sv; right column). X-axis for each panel is S (g/kg). Y-axis is θ (°C). The dashed blue contour corresponds to the SAMW sector, the dashed reddish-purple contour corresponds to the AAIW sector and the dashed dark gray contour corresponds to the CDW sector. 90

4.11 Phase (month) of maximum transformation by each surface component. The x-axis of each panel is salinity (g/kg); y-axis is potential temperature (°C). Contours are the same as the left column of Fig. 4.10. 91

4.12 Net heat transformation (Sv, shaded) for surface heat flux and surface freshwater flux. The x-axis of each panel is S (g/kg); y-axis is θ (°C). The dashed lines depicting the 26.75 σ_θ isopycnal corresponds to the dashed vertical lines in Fig. 4.16. 93

4.13 Sea ice concentration and density flux due to heat loss during March, May, July and September, 2005 (austral fall and winter). The areas of heat loss density flux correspond to sensible-heat polynyas and embayments. Similar, but smaller, polynyas and embayments also occur in 2006. The green dot at 67.0416°S, 10.083°W indicates the point at which polynya-induced deep convection occurs for the longest duration during the simulation. 94

4.14 A time versus depth (y-axis depicted using $\log_{10}$ scale) plot of θ and S for the point at 67.0416°S, 10.083°W. The dark gray dashed line denotes the extent of CDW, which typically exists beneath the cold and fresh surface layer but reaches the surface from May through September of 2005. A weaker convection event is also visible in 2006 but composition of the surface mixed layer is not warm and salty enough to be considered CDW. 96

4.15 Latitude-depth transects along 89°W for February and September 2008. Contours and shading same as in Fig. 4.8. The deep convection mixing AAIW up to the surface is visible in the vicinity of the Subantarctic Front in panels B, D, and F. . . 98

4.16 One dimensional surface transformations computed by applying Eq. 4.16 to the $T(\theta, S)$ transformations in Fig. 4.10 and applying a smoothing filter since the $T(\theta, S)$ transformations are computed at discrete grid points in the $\theta - S$ plane. Comparing this figure to Fig. 4.10 demonstrates how a mean transformation by a single component does not necessarily represent a conversion from dense water to lighter water (or vice versa) because in the subpolar region the seasonal cycle of heating and cooling is accomplished by different components of the coupled atmospheric, cryospheric and oceanic system. 100

Acronyms

AABW Antarctic Bottom Water. 68, 92

AAIW Antarctic Intermediate Water. ix, xx, xxii–xxiv, 65, 66, 72, 73, 76, 80–82, 85, 88–92, 95, 97–99, 101–103

AASW Antarctic Surface Water. ix, 65, 67, 70, 76, 88, 92, 95, 100–102

ACC Antarctic Circumpolar Current. 65

CDW Circumpolar Deep Water. ix, xx, xxii–xxiv, 65, 66, 70, 73, 74, 76, 81, 85, 88, 90–92, 95, 96, 102

CESM Community Earth System Model. iii, xii, 8, 10, 12, 14, 27, 28, 31, 106

CICE4 Community Ice CodE 4. iii, 10, 106

CISL Computational and Information Systems Laboratory. iii, 28, 63

CMAP Climate Prediction Center Merged Analysis of Precipitation. 10, 106

CORE Coordinated Ocean-Ice Reference Experiments. x, 10, 11, 31, 106–108

CSW continental shelf water. 101

E-P evaporation minus precipitation. ix, 4, 5, 7, 12, 13, 15, 16, 26, 39

ENSO El Niño/Southern Oscillation. 9, 29, 30, 36

EPFP Eastern Pacific Fresh Pool. 29–31, 34, 36

FDR false discovery rate. xix, 39, 57, 58, 61, 62

GPCP Global Precipitation Climatology Project. 11, 106

IDW Indian Deep Water. 73, 92

ITCZ Intertropical Convergence Zone. 29, 30, 34, 36

KPP K-profile parameterization. 10, 11, 28, 106

LCDW Lower Circumpolar Deep Water. 73

MCDW Modified Circumpolar Deep Water. 73, 74

MIMOC Monthly Isopycnal & Mixed-layer Ocean Climatology. xii–xiv, 12–15, 23, 31, 32

MITgcm Massachusetts Institute of Technology General Circulation Model. 68, 103

MLD mixed layer depth. 13, 16

MSU Microwave Sounding Unit. 10, 106

MW mode water. 7, 9, 18, 19, 23, 26, 27, 75

NA North Atlantic. 5, 6, 9, 13, 15, 16, 24, 26, 27

NADW North Atlantic Deep Water. 73, 76, 92

NCAR National Center for Atmospheric Research. iii, iv, 28, 63, 105

NCEP National Centers for Environmental Prediction. 10, 106, 108

NECC North Equatorial Counter Current. 30, 31

NH Northern Hemisphere. xii, xiii, 4, 5, 8, 15, 19, 20

NI North Indian. xii, 4–6, 13, 15, 16, 19, 24, 26

NP North Pacific. xiii, 9, 10, 13, 15, 16, 18, 19, 23, 24, 26, 27

NSF National Science Foundation. iii, 28, 63, 103

OGCM ocean general circulation model. 4–6

PDW Pacific Deep Water. 73, 92

PF Polar Front. xx, xxii, 70, 71, 76, 85, 87, 88, 97

POP2 Parallel Ocean Program 2. iii, 10, 105, 106

psu practical salinity units. ix, xiii–xv, 5, 11, 15–18, 30–36

RHS right-hand side. 12, 77

S$_{max}$ salinity maxima. ix, xii–xiv, 4–9, 12, 13, 15–21, 23, 24, 26–28, 30, 31, 36

S$_{min}$ salinity minimum. 29, 30

SA South Atlantic. 13, 15, 16, 24, 27

sACCF Southern Antarctic Circumpolar Current Front. xx, xxii, 70, 71, 85, 88, 97

SAF Subantarctic Front. xx, xxii, 69, 71–73, 82, 85

SAMW Subantarctic Mode Water. xx–xxiii, 65, 66, 72, 73, 75, 76, 80–83, 85–88, 90–92, 95, 97, 101–103

SASW Subantarctic Surface Water. 69, 70, 101

SH Southern Hemisphere. xii, xiv, 4, 5, 8, 15, 19, 21

SHF surface heat flux. 5, 6, 16, 26, 27

SI South Indian. 5, 13, 15, 16, 24, 26

SLS surface layer salinity. xii–xiv, xviii, xix, 4, 5, 7, 13, 15, 16, 23, 26–28, 30–32, 34, 39, 40, 49, 51, 52, 54, 55, 57, 59, 61, 63

SMOS Soil Moisture and Ocean Salinity. 30

SOSE Southern Ocean State Estimate. vii, xx, xxii, 67–69, 71, 74–78, 81, 82, 87, 93, 95, 97, 102, 103, 105

SP South Pacific. xiii, 9, 13, 15, 16, 18, 19, 23, 24, 26

SPURS-2 Salinity Processes in the Upper Ocean Regional Study 2. 30

SSH sea surface height. 31

SST sea surface temperature. xviii, xix, 7, 39, 40, 50, 52, 54, 55, 58, 59, 61, 62

STC subtropical cell. 9, 19, 23, 27, 30

STF Subtropical Front. xx, xxii, 69, 71, 72, 85

STMW subtropical mode water. 27

STSW subtropical surface water. 101

STUW subtropical underwater. xii, 6, 7, 12, 13, 19, 26

Sv Sverdrups. ix, xiii, xiv, 16, 17, 34

UCDW Upper Circumpolar Deep Water. 70, 73, 92, 102

UMD University of Maryland. iv

WOCE World Ocean Circulation Experiment. xxii, 11, 82, 85–87, 97, 107

Introduction

The disciplines of meteorology and oceanography are both vital to understanding the earth system. Throughout most of the last half century, meteorology has largely been a prognostic discipline. Forecasts made by meteorologists have been widely used and scrutinized, allowing for countless opportunities to test and improve ideas about atmospheric circulation and physics. Since weather forecasts involve integrating numerical models and updating the model state via data assimilation, forecasting demands frequent use of the principles of Bayesian inference. This requirement essentially confronts the physics contained within numerical models at recurring intervals and can reveal systematic model bias.

In contrast, prognostic applications have been less prevalent in oceanography. Oceanographic forecasts are much rarer than atmospheric forecasts and, perhaps as a consequence of this disparity, many ideas concerning oceanic circulation have not been tested to the same degree as ideas concerning atmospheric circulation.

This dissertation presents three methods for testing oceanographic ideas:

- Applying methodologies to analogous features from different ocean basins allows for the isolation of relevant processes. In the first chapter we study the six salinity maxima that manifest in the subtropical oceans using an isohaline salinity budget. These maxima manifest because evaporation exceeds precipitation in the subtropics. Five of the salinity maxima form in the open ocean while the sixth, the North Indian, forms in the Arabian Sea. Comparing the salinity budgets and vertical structures of the maxima allows us to find that despite different surface forcing, all of the open-ocean salinity maxima have vertical diffusive fluxes that peak in the late winter. The eastward and poleward edges of these maxima are susceptible to a type of mixing known as salt finger convection that enhances the diffusive flux of salinity out of the maxima in the late winter. In contrast, the North Indian salinity maximum is not susceptible to salt finger convection and its vertical diffusive flux remains relatively constant throughout the year. We also contrast these regions to the Equatorial Pacific Fresh Pool in a short additional chapter.

- Synthetic time series can be used to understand the properties of oceanographic time series in order to construct null distributions for hypothesis testing. We use synthetic time series to mimic observed properties of time series of surface layer salinity and sea surface temperature to examine how samples taken from such time series are affected by three complications: autocorrelation, measurement error, and multiple simultaneous hypothesis tests. We then discuss techniques that can be used to account for these complications in order to correctly construct null distributions for hypothesis testing. These complications are critical to understand, because surface layer salinity is used by the oceanographic community to detect changes in the hydrological cycle. We find that the salinity changes discussed in previous studies, while believed to be significant by many members of the oceanographic community, are not significant at the levels reported in the literature when the complications are taken into account. This work suggests that many of the conclusions within this subset of the oceanographic literature should be reevaluated.

- The water mass transformation framework is used to relate air-sea fluxes of heat and freshwater to the rate of change of the density of seawater. This rate is known as the transformation rate and its convergence, the formation rate, is used to infer the rate at which the ocean's water masses are formed and destroyed. These estimates of water mass formation and destruction are used by the oceanographic community to understand how air-sea fluxes influence broad-scale ocean circulation. These inferences, however, are rarely compared against the observational descriptions of the water masses. We conduct potential temperature-salinity censuses of the water masses and compare the census results against the surface transformations. This technique reveals that many of the surface fluxes that are believed to be relevant to water mass transformation are actually related to the seasonal cycle of surface water transformation rather than the transformation of the subsurface water masses.

These chapters share common threads, most importantly the use of conserved tracers to understand the ocean. The first, second and third chapters use the ocean's salinity field to infer circulation within the ocean and changes in the hydrological cycle. The first, second and fourth chapters use isosurface budgets to study the ocean's structure and circulation. The third and fourth chapters offer critiques of the previously published literature and suggestions for improving our understanding of ocean structure and the changes observed within it.

We speculate on the implications of this dissertation in a final concluding chapter.

Chapter 1

Climatological Annual Cycle of the Salinity Budgets of the Subtropical Maxima

1.1 Abstract

Six subtropical S$_{max}$ exist: two each in the Pacific, Atlantic, and Indian Ocean basins. The NI S$_{max}$ lies in the Arabian Sea while the remaining five lie in the open ocean. The annual cycle of E-P flux over the S$_{max}$ is asymmetric about the equator. Over the NH S$_{max}$, the semiannual harmonic is dominant (peaking in local summer and winter), while over the SH S$_{max}$, the annual harmonic is dominant (peaking in local winter). Regardless, the SLS for all six S$_{max}$ reaches a maximum in local fall and a minimum in local spring. This study uses a multidecade integration of an eddy-resolving ocean general circulation model (OGCM) to compute salinity budgets for each of the six S$_{max}$. The NI S$_{max}$ budget is dominated by eddy advection related to the evolution of the seasonal monsoon. The five open-ocean S$_{max}$ budgets reveal a common annual cycle of vertical diffusive fluxes that peak in winter. These S$_{max}$ have regions on their eastward and poleward edges in which the vertical salinity gradient is destabilizing. These destabilizing gradients, in conjunction with wintertime surface cooling, generate a gradually deepening wintertime mixed layer. The vertical salinity gradient sharpens at the base of the mixed layer, making the water column susceptible to salt finger convection and enhancing vertical diffusive salinity fluxes out of the S$_{max}$ into the ocean interior. This process is also observed in Argo float profiles and is related to the formation regions of subtropical mode waters.

Table 1.1: Isohaline, in psu, bounding each S$_{max}$.

S$_{max}$	*NA* S$_{max}$	*SA* S$_{max}$	*NI* S$_{max}$	*SI* S$_{max}$	*NP* S$_{max}$	*SP* S$_{max}$
Isohaline	37.0	37.0	35.8	35.6	35.2	36.1

1.2 Introduction

The broad patterns of SLS are set by the interaction of surface waters with the atmosphere (Wust, 1935). The descending branch of the Hadley Cell drives anticyclonic flow over the ocean basins causing evaporation to exceed precipitation, elevating SLS and creating six subtropical salinity maxima (hereafter S$_{max}$). Five of the S$_{max}$ lie primarily in the open-ocean: the Pacific and Atlantic S$_{max}$ are located around 25°N and 20°S; the South Indian (SI) S$_{max}$ is around 30°S (Gordon et al., 2015). The NI S$_{max}$ lies in the Arabian Sea and Gulf of Oman around 18°N. Coasts bound it to the north and west. For brevity we will refer to each S$_{max}$ by the first initial of its hemisphere and ocean basin, e.g. North Atlantic (NA) S$_{max}$ denotes the North Atlantic subtropical salinity maxima. The S$_{max}$ are bounded by different isohaline values given in Table 1.1. We selected these values as those that define the maximum volume that is confined to the subtropical region of each basins' corresponding hemisphere.

The annual cycle of E-P flux over the subtropical regions is asymmetric about the equator (Large and Yeager, 2009). Over the NH S$_{max}$ the semiannual harmonic dominates (peaking in local summer and winter) while over the SH S$_{max}$ the annual harmonic dominates (peaking in local winter). In spite of this asymmetry in E-P forcing, the SLS of all six S$_{max}$ reaches a maximum in local fall and minimum in local spring (open-ocean S$_{max}$: Gordon et al., 2015; NI S$_{max}$: Rao and Sivakumar, 2003). On the eastward and poleward edges of each open-ocean S$_{max}$, the vertical gradient of salinity, $\partial_z S$, is destabilizing and the net surface heat flux (SHF) changes sign during the transition from summer to winter. Bingham et al. (2012) depict seasonal SLS variability in these areas (see their Fig. 4), which suggests that the position of the S$_{max}$ within each basin influences SLS variability in the surrounding regions.

This study employs an eddy-resolving OGCM to compute salinity budgets for all six S$_{max}$ to address two objectives: determine the importance of individual ocean processes in balancing climatological mean E-P forcing and to discover why, in spite of their different annual cycles of E-P, the annual cycle of SLS for all six S$_{max}$ is dominated by the annual harmonic. Following Bryan and Bachman (2015), who studied NA S$_{max}$, these budgets are computed within a control volume that is bounded by an isohaline surface in order to eliminate the mean advection term from the budget. NA S_{max} is perhaps the most well-studied S_{max}, as it was the site of the Salinity Processes in the Upper Ocean Regional Study (SPURS; Lindstrom et al., 2015) and is a region of high-coverage by the Ship of Opportunity Program (Reverdin et al., 2007). Previous observation-based studies have emphasized the importance of different processes in the subtropical salinity balance: horizontal advection by Ekman and geostrophic flow (Yu, 2011), vertical fluxes (Qu et al., 2011, who only examined NA S_{max}; Bingham et al., 2012), and eddy fluxes (Gordon and Giulivi, 2014, who only examined NA S_{max}).

While OGCMs have the ability to simulate regularly gridded fields of oceanographic variables, including diffusion terms that are difficult to measure in situ, they experience a particular challenge that is relevant to the salinity budget. Of the two components that determine the density and stability of seawater, potential temperature, θ, and salinity, S, the latter has been more difficult for OGCMs to model with fidelity (Durack et al., 2013). Because modeled S distributions can be biased – even in this precise model configuration, as discussed by Bryan and Bachman (2015) – this study reinforces its key results with comparisons to Argo float data.

1.3 Background

The subsurface structure of each S_{max} creates gradients that constrain large-scale patterns of vertical mixing. The open-ocean S_{max} each have a subsurface salinity maximum known as STUW (O'Connor et al., 2002). The STUW are located westward and equatorward of the sea surface salinity maxima (shown schematically in Fig. 1.1). This displacement creates contrasting regions of $\partial_z S$ along the edges of the open-ocean S_{max}. On their eastward and poleward edges, $\partial_z S$ is destabilizing – S decreases with depth, creating a top-heavy salinity distribution. Conversely, on their westward and equatorward edges, $\partial_z S$ is stabilizing – S increases with depth, creating a bottom-heavy salinity distribution. Unlike the open-ocean S_{max}, the subsurface salinity maximum beneath NI S_{max} is located approximately beneath the surface maximum and thus $\partial_z S$ is weak.

In addition to these regions of contrasting $\partial_z S$, the stratification of subtropical oceans is affected by an annual cycle of SHF, which changes sign during the course of a year. All of the S_{max} experience net heating during the summer and net cooling during the winter (Fig. 1.2), however the annual cycle of SHF over NI S_{max} is distinct. It has the shortest period of surface cooling (typically from

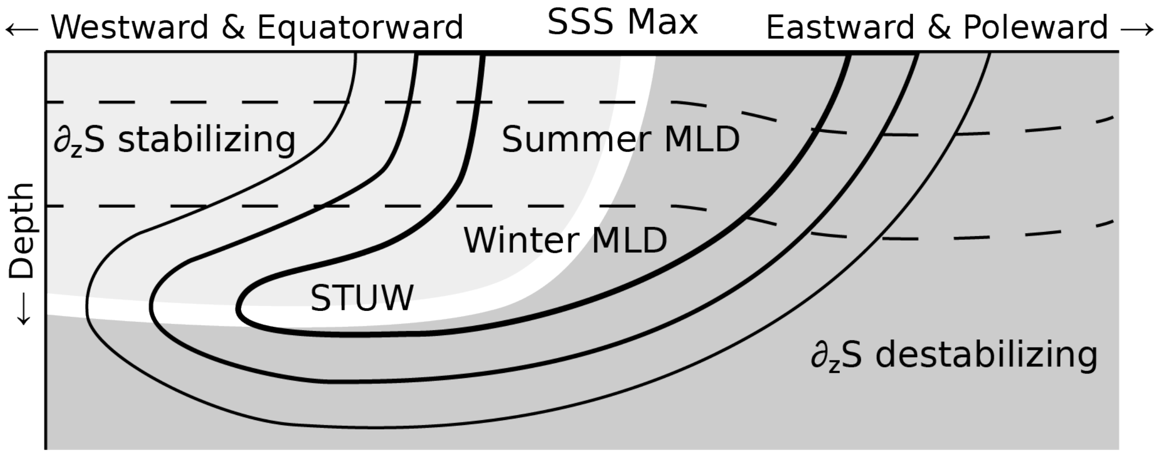

Figure 1.1: A schematic of an open-ocean S_{max}. Solid lines represent isohaline contours, with contour thickness representing salinity. The dark (light) shaded region depicts that in the mixed layer eastward & poleward (westward & equatorward) of the SLS max ∂_z S is stabilizing (destabilizing) due to the displacement of STUW with respect to the SLS maximum.

mid-November to early February) and its period of surface heating is interrupted by a relatively weak period during local summer. Consequently, its mixed layer exhibits maximum depth in January and has a secondary maximum in July (Weller et al., 2002). The open-ocean S_{max} have mixed layers that gradually deepen throughout local winter and rapidly shoal in local spring. For the open-ocean S_{max}, the coldest wintertime SSTs exist on their eastward and poleward edges.

Since $\partial_z S$ and the vertical gradient of potential temperature, $\partial_z \theta$, can compensate for each other (i.e. a column with destabilizing $\partial_z S$ can be stabilized by $\partial_z \theta$) a measure of their composite influence on stability is the density ratio,

$$R_\rho = \alpha_T \partial_z \theta / (\beta_S \partial_z S) \tag{1.1}$$

where α_T and β_S are the thermal expansion and haline contraction coefficients, respectively. The density ratio in the surface layer changes throughout the year as E-P fluxes alter $\partial_z S$ and surface cooling in the autumn and winter weakens (warming in the spring and summer strengthens) $\partial_z \theta$.

A notable manifestation of this air-sea interaction is the generation of various types of subtropical mode waters (MWs). In a review of subtropical MWs, Hanawa and Talley (2001) develop a classification system organizing them into types, two of which are relevant to this study: Type I – the archetype of which is 18° MW (Worthington, 1959) – which form on the equatorward side of western boundary current extensions due to convection induced by intense winter cooling and are

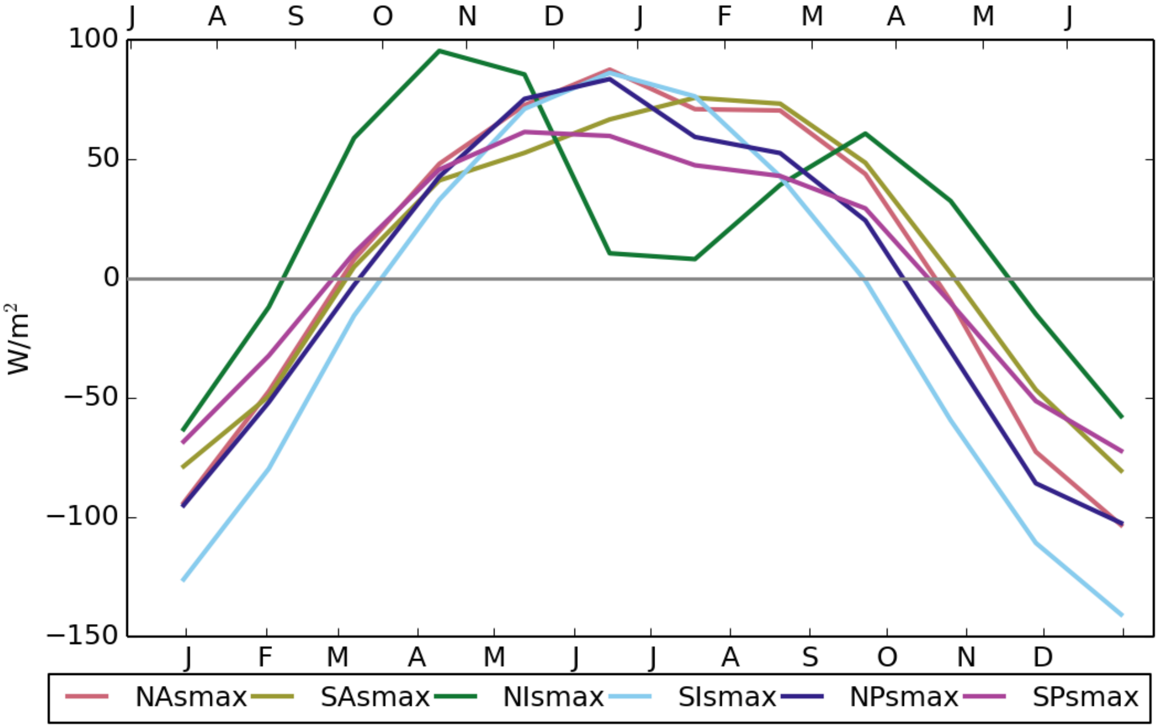

Figure 1.2: The climatological annual cycle of surface heat flux (W/m^2) over each S$_{max}$ in CESM. The x-axis is offset by six months for the SH S$_{max}$ (top x-axis labels) with respect to the NH S$_{max}$ (bottom x-axis labels) to account for the hemispheric phase shift of the seasons.

relatively uniform in potential density, ρ_θ; and Type II – the archetype of which is Madiera MW (Käse et al., 1985; Siedler et al., 1987) – which form on the eastward and poleward edges of the S$_{max}$, have variable ρ_θ and density-compensating $\partial_z S$ and $\partial_z \theta$ (Toyama and Suga, 2010).

Type II MWs are of particular interest in regard to the subtropical cells (STCs) (McCreary and Lu, 1994), which are shallow overturning circulations that connect the subtropical and tropical oceans. STCs provide a mechanism by which the properties of subtropical oceans can propagate subsurface through the Central Waters of the thermocline (e.g. Schmitt, 1981; Sprintall and Tomczak, 1993) to the tropical oceans where they can potentially influence the frequency or intensity of El Niño/Southern Oscillation (ENSO) events (e.g. Gu and Philander, 1997; Cane et al., 1997). The formation region of Type II MWs coincides with the source region of the descending branch of the STCs (e.g. Joyce et al., 1998; Johnson, 2006) and these MWs have been identified within the vicinity of NA S$_{max}$ (Käse et al., 1985), NP S$_{max}$ (Hautala and Roemmich, 1998) and SP S$_{max}$ (Tsuchiya and Talley, 1996).

Type II MW volumes vary significantly throughout the year. After decaying to minimum thickness in the summer, they build throughout the fall and reach peak thickness in the late winter as surface cooling weakens $\partial_z \theta$, which, in conjunction with the destabilizing $\partial_z S$ component, decreases the stability of the column and enhances mixing. This wintertime buildup deepens the mixed layer and increases S at depth. $\partial_z S$ sharpens below the MW layer near the base of the mixed layer, which, in conjunction with the weakened $\partial_z \theta$, decreases R_ρ. This enhances S fluxes from the mixed layer into the thermocline (Yeager and Large, 2004) and makes water columns susceptible to salt finger convection (Johnson, 2006). Salt finger convection is a type of double diffusive convection arising in water columns in which θ and S both decrease with depth and R_ρ is sufficiently low (typically when $1 < R_\rho < 2$). Since the diffusivity of θ is roughly two orders of magnitude greater than the diffusivity of S, water parcels lose heat much faster than they lose salt and become negatively buoyant (Stern, 1960) creating finger-like convective plumes. Salt finger convection acts to reduce the potential energy stored in the top-heavy S distribution by transporting salt downward in the convective plumes at a faster rate than they transport heat (which diffuses out of the walls of the convective plumes). This allows salt finger convection to transport density upgradient in a fluid, increase its stability and, in the context of this discussion, hasten the decay of the MW. Salt finger convection has been inferred from in situ data beneath the Type II MW formation regions of the NA (St. Laurent and Schmitt, 1999; Kolodziejczyk et al., 2015), SP (Wong and Johnson, 2003;

Kolodziejczyk and Gaillard, 2013), and NP (Sugimoto and Hanawa, 2007; Toyama and Suga, 2010).

1.4 Numerical Experiment and Results

1.4.1 Model description

We used the POP2 (Smith et al., 2010) and CICE4 (Bailey et al., 2010) components of CESM in an eddy-resolving oceanic tripole grid (Murray, 1996) with zonal resolution of 0.1°, meridional resolution of 0.1° cos(lat) and 62 vertical levels (10m spacing above 160m and gradually increasing spacing towards the sea floor).

The equation of state is computed using the method of McDougall et al. (2003). Freshwater forcing is imposed as a virtual salt flux. Vertical mixing is represented using the K-profile parameterization (KPP) of Large et al. (1994). Turbulent shear mixing and double diffusive convection are represented by increasing vertical diffusivity above the background diffusivity, κ. Shear mixing is a function of the gradient Richardson number. Salt finger convection is a function of R_ρ, as defined in Eq. 1.1, according to the empirical parameterization of St. Laurent and Schmitt (1999):

$$\kappa_{DD}(R_\rho) = \kappa_d^0[1 - (R_\rho - 1)/(R_\rho^0 - 1)]^3 \tag{1.2}$$

where $R_\rho^0 = 2.55$ and κ_d^0 is $1 \times 10^{-2} m^2/s$ and $7 \times 10^{-3} m^2/s$ for salt and heat, respectively. The mixed layer depth is computed as the shallowest local maximum of the buoyancy gradient.

1.4.2 Model experiment

We forced the ocean and ice components of CESM in accordance with the CORE (Griffies et al., 2009) guidelines. The COREv2 dataset is composed of a blend of National Centers for Environmental Prediction (NCEP) reanalysis (Kalnay et al., 1996) and a variety of satellite-based reconstructions of surface atmospheric state and flux fields (Large and Yeager, 2009). COREv2 includes interannually varying forcing data, spanning the years 1948-2009 and a single “normal year” which is an exactly repeating synthetic year derived from the interannually varying data. The interannual dataset incorporates observational and reanalysis data from a variety of sources with irregular start and stop times. In 1979, COREv2 begins incorporating data from the Microwave Sounding Unit (MSU) (Spencer, 1993), the Climate Prediction Center Merged Analysis of Precipitation (CMAP) product

(Xie and Arkin, 1996) and Global Precipitation Climatology Project (GPCP) data (Huffman et al., 1997). Coastal runoff is imposed using the Dai and Trenberth (2002) climatology. The model was initialized with temperature and salinity distributions from the WOCE climatology (Gouretski and Koltermann, 2004) and spun up for 15 model years with COREv2 normal year forcing. This spin up was shared by the experiment described in Bryan and Bachman (2015) but the integrations branched after spinup: Bryan and Bachman continued by extending their integration for another 5 years under normal-year forcing; the integration in this study continued for another 33 years under interannually varying forcing corresponding to the years 1977-2009. Since the transition from normal-year forcing to interannual forcing makes the forcing fields discontinuous, we started the interannual forcing in 1977 to mitigate the effects of these perturbations and restricted our analysis to the output from 1979-2009. Output was saved as five-day averages and converted to monthly averages using a weighted mean.

1.4.3 Model analysis

To derive our salinity budget we start with the model's salinity conservation equation:

$$\frac{\partial S}{\partial t} = -\nabla \cdot (\mathbf{u}S) + \left[\frac{\partial}{\partial z}\kappa\left(\frac{\partial S}{\partial z} - \Gamma\right)\right] + A_S \nabla_h^4 S \tag{1.3}$$

where S is the salinity, κ is the vertical diffusivity, $\kappa\Gamma$ is the KPP counter gradient flux, and A_s is the horizontal hyperdiffusivity. The surface boundary conditions for Eq. 1.3 are:

$$\kappa \frac{\partial S}{\partial z}|_{z=0} = S_{ref}(E - P) \tag{1.4}$$

$$\kappa\Gamma|_{z=0} = 0 \tag{1.5}$$

where E is evaporation, P is precipitation, and $S_{ref} = 34.7$ psu is the model's constant reference salinity used to convert freshwater fluxes to a virtual salt flux. We compute the integral of Eq. 1.3 upon climatological monthly mean output (denoted by the bar, $\bar{\cdot}$) within a volume, V, that is bounded in the ocean interior by an isohaline surface ∂V, upon which $\bar{S} = S_o$ and at the surface by a time-dependent outcrop area, A within which $\bar{S} > S_o$:

$$\begin{aligned}\iiint_{V(\bar{S}>S_o)} \frac{\partial \overline{S}}{\partial t} dv = -\iint_{\partial V(\overline{S}=S_o)} \overline{\mathbf{u}S} \cdot d\mathbf{a} + \iint_{\partial V(\bar{S}=S_o)} \overline{\left(\kappa \frac{\partial S}{\partial z} - \Gamma\right) \mathbf{k}} \cdot d\mathbf{a} + \\ \iint_{A(\bar{S}>S_o)} S_{ref}\overline{(E-P)} dA + \iiint_{V(\bar{S}>S_o)} A_S \nabla_h^4 \overline{S} dv\end{aligned} \tag{1.6}$$

Since the first term of the right-hand side (RHS) of Eq. 1.6 is a covariance, we can partition it into time-mean and eddy terms:

$$\iint_{\partial V(\overline{S}=S_o)} \overline{\mathbf{u}S} \cdot d\mathbf{a} = S_o \iint_{\partial V(\overline{S}=S_o)} \overline{\mathbf{u}} \cdot d\mathbf{a} + \iint_{\partial V(\overline{S}=S_o)} \overline{\mathbf{u}'S'} \cdot d\mathbf{a} = \iint_{\partial V(\overline{S}=S_o)} \overline{\mathbf{u}'S'} \cdot d\mathbf{a} \tag{1.7}$$

The term describing time-mean velocity advection vanishes, resulting in:

$$\begin{aligned}\iiint_{V(\bar{S}>S_o)} \frac{\partial \overline{S}}{\partial t} dv = -\iint_{\partial V(\overline{S}=S_o)} \overline{\mathbf{u}'S'} \cdot d\mathbf{a} + \iint_{\partial V(\bar{S}=S_o)} \overline{\left(\kappa \frac{\partial S}{\partial z} - \Gamma\right) \mathbf{k}} \cdot d\mathbf{a} + \\ \iint_{A(\bar{S}>S_o)} S_{ref}\overline{(E-P)} dA + \iiint_{V(\bar{S}>S_o)} A_S \nabla_h^4 \overline{S} dv\end{aligned} \tag{1.8}$$

We denote the terms of Eq. 1.8 from left to right, as tendency, eddy advection, vertical diffusion, E-P and horizontal diffusion. Since CESM imposes no-flux boundary conditions at solid surfaces, the volume described here can intersect coastlines and the seafloor. We use Eq. 1.8 to compute the budget on the climatological monthly mean output of the years 1979-2009 of the integration. Bryan and Bachman (2015) demonstrate that since eddy mixing is a two-stage process where eddies first stir the fluid, enhancing local θ/S gradients, and small-scale mixing then acts upon these gradients, computing the budget on climatological monthly mean data allows for the inference of the total mixing induced by the eddies. Finally, to evaluate model bias, we compare the outcrop area for each S_{max} to the MIMOC climatology (Schmidtko et al., 2013). Since MIMOC is largely based on Argo data, we use only the model years that overlap with the Argo era (2000-2009) during this comparison.

1.4.4 Model Results and Discussion

Climatological Description of the S_{max}

Consistent with observations of STUW, subsurface isohaline contours are displaced westward and equatorward of the surface outcrops (Fig. 1.3) of each open-ocean S_{max} (resembling Fig. 1.1). The

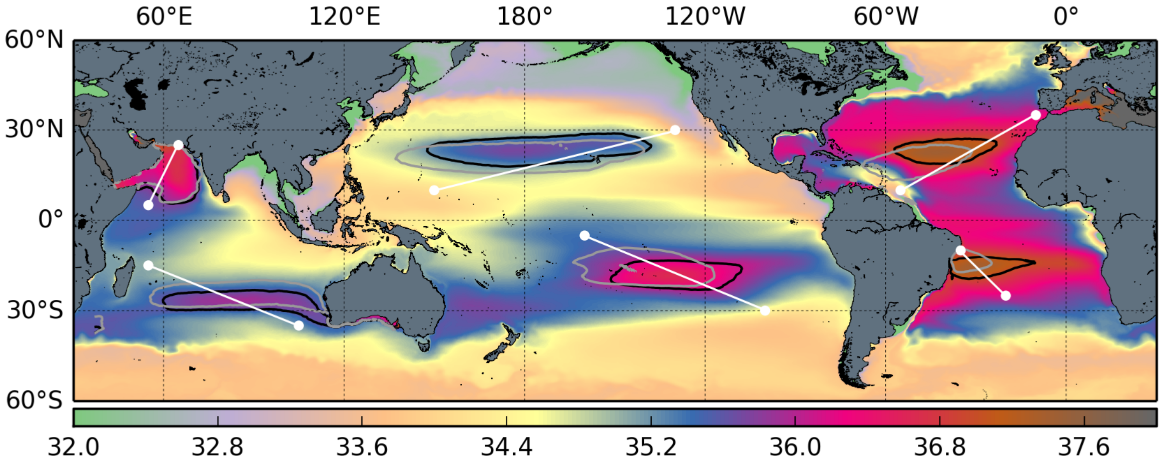

Figure 1.3: The model climatological mean SLS. Black contours are the mean position of isohaline surface outcrops for each S_{max}. Gray contours are isohalines at 100m depth. Each of the open-ocean S_{max} contours at 100m depth is positioned westward and equatorward of the surface outcrop. The NI S_{max} surface and 100m contours are at roughly the same position. White lines depict transects along which depth profiles are shown in Figs. 1.8 & 1.9.

subsurface isohaline contour is not displaced for NI S_{max}. The STUW of South Atlantic (SA) S_{max} is displaced more equatorward and less westward in comparison with the other S_{max} because it abuts the coast of Brazil. In the vicinity of the open-ocean S_{max}, the mean mixed layer depths (MLDs) range from around 50m in the summer months to around 100-130m in the winter months. The simulation's annual SLS cycles, as indicated by outcrop extent (Fig. 1.4), are roughly in phase with MIMOC observations although the amplitude of the MIMOC annual cycles is larger for all S_{max}. The phase of these annual SLS cycles is also consistent with in situ observations (NI S_{max}: Rao and Sivakumar, 2003; open-ocean S_{max}: Gordon et al., 2015) with seasonal maxima (minima) in local fall (spring). The model tends to have a fresh bias (Fig. 1.5), with smaller outcrops for each S_{max}, with the exception of NP S_{max}. The open-ocean S_{max} outcrops tend to have a spatial bias, with the MIMOC outcrops extending farther eastward and poleward. This bias suggests the model may overestimate vertical diffusive fluxes in regions that have destabilizing $\partial_z S$.

Climatological S_{max} Salinity Budgets

We consider the percentage of the climatological annual mean E-P that is balanced by each budget term (Table 1.2). Eddy advection balances the largest percent of E-P in NI S_{max} (-77%), SI S_{max} (-70%), NP S_{max} (-60%) and NA S_{max} (-55%). Vertical diffusion balances the largest percent of E-P in SP S_{max} (-60%) and SA S_{max} (-55%). The tendency term is small but of the same sign as E-P in

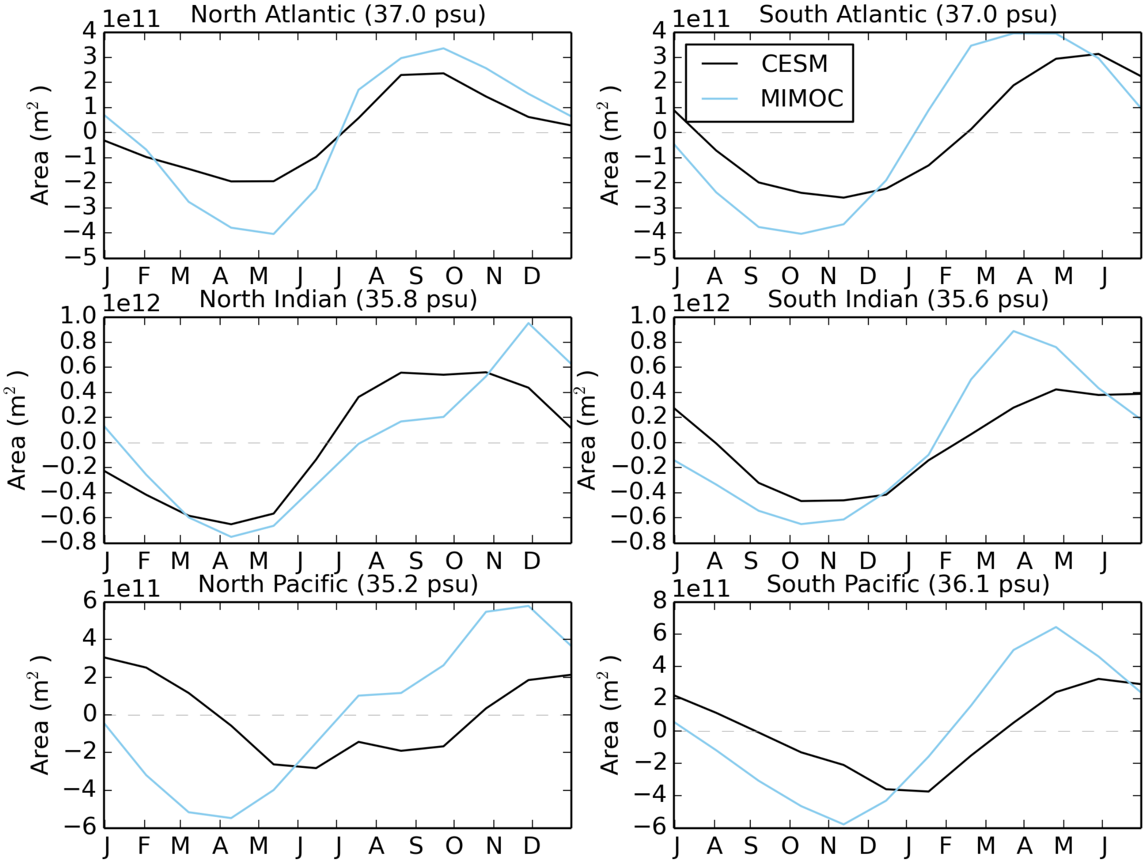

Figure 1.4: The annual cycle of outcrop extent anomaly (m^2) from annual mean value for CESM (black) and MIMOC (light blue).

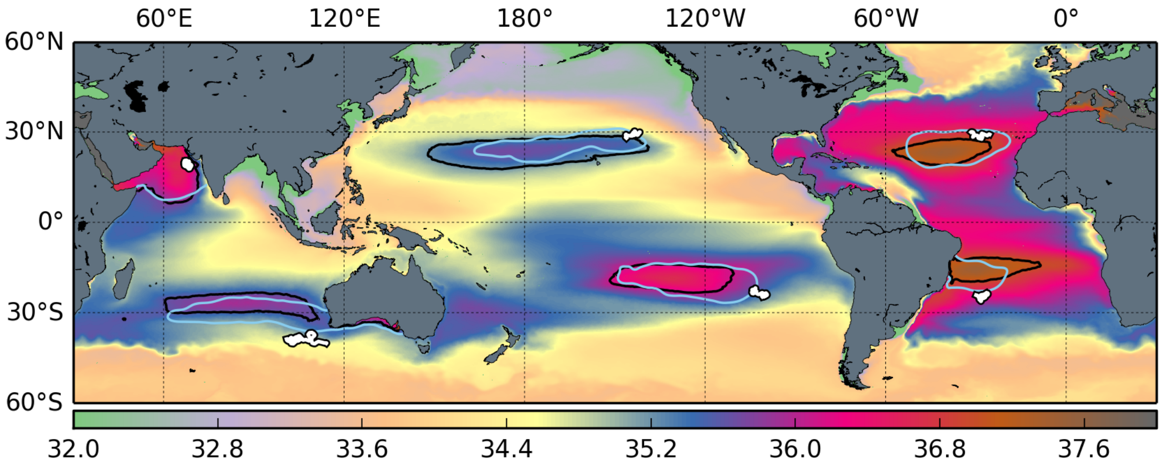

Figure 1.5: Model climatological mean SLS (psu, shaded) and comparison of climatological mean S_{max} outcrops of the integration (black contours) and MIMOC (light blue). In all cases, with the exception of NP S_{max}, the MIMOC outcrops are larger, with the largest discrepancy in SP S_{max}, where MIMOC outcrop area is nearly double that of the model. The white paths along the eastward and poleward edges of each MIMOC outcrop are the position of the Argo floats over the two-year periods described in Section 1.5.

all six S_{max}, indicating that the mean salinity of each S_{max} increased during the integration. While this is consistent with the amplification of SLS variance (Durack and Wijffels, 2010) in response to a strengthening hydrological cycle (Held and Soden, 2006) this result could also be a consequence of model drift (Durack et al., 2013).

Turning our attention to the annual cycles of each budget (Fig. 1.6), the SH S_{max} exhibit E-P minima in the late spring (November for SA and SI; December for SP) and maxima in the winter (June for SP; July for SA and SI). The NH S_{max} exhibit an annual cycle of E-P dominated by the semiannual harmonic with wintertime maxima in January and summertime maxima in June (NP) or July (NA and NI). In spite of this difference in the annual cycle of E-P, the annual cycle of net S flux out of the S_{max} into the ocean interior (which is the sum of the horizontal diffusion, vertical diffusion and eddy advection terms) is roughly in phase for all of the S_{max}. In each of the open-ocean S_{max}, the magnitude of net flux is greatest in the winter while the net flux for NI S_{max} peaks in the late fall. The magnitude of the vertical diffusion term peaks in the winter for all of the open-ocean S_{max}. The magnitude of the eddy advection term nearly doubles in the winter for SI S_{max} and is slightly enhanced for NA and SA S_{max}. It does not have a noticeable seasonality in NP and SP S_{max}. In NI S_{max}, the magnitude of eddy advection reaches a minimum in April and maximum in October. This is likely related to the onset of the Southwest Monsoon, which develops during the

Table 1.2: Climatological annual mean magnitude of each budget term and the percent of E-P balanced by each of the remaining budget terms (Sv psu). Since the mean advection term should vanish from Eq. 1.7 it provides an estimate of the error in Eq. 1.8. We include its magnitude as an error estimate in the rightmost column.

S_{max}	*E - P*	*Tendency*	*Hor Diff*	*Eddy Adv*	*Ver Diff*	*Error*
NA Mag	2.90	0.05	-0.01	-1.58	-1.37	1E-3
% of E-P	100%	2%	0%	-55%	-47%	N/A
SA Mag	2.49	0.05	-0.02	-1.16	-1.36	2E-3
% of E-P	100%	2%	-1%	-46%	-55%	N/A
NI Mag	3.58	0.13	0.03	-2.74	-1.01	7E-3
% of E-P	100%	4%	1%	-77%	-28%	N/A
SI Mag	4.4	0.1	0.0	-3.1	-1.5	2E-2
% of E-P	100%	3%	0%	-70%	-34%	N/A
NP Mag	5.8	0.1	0.0	-3.5	-2.4	2E-2
% of E-P	100%	1%	0%	-60%	-42%	N/A
SP Mag	3.6	0.0	0.0	-1.5	-2.2	1E-2
% of E-P	100%	1%	0%	-41%	-60%	N/A

summer and dissipates during the fall and is associated with freshening in the Arabian Sea (Rao and Sivakumar, 2003).

Vertical Diffusion in the Subtropics

Since the annual cycle of S flux from NI S_{max} into the ocean interior is governed by a distinct process, eddy advection, we continue by examining why the magnitude of the vertical diffusion term peaks in the late winter for the open-ocean S_{max}. However, since the vertical diffusion term peaks in winter in the open-ocean S_{max} and is approximately constant throughout the year in the NI S_{max}, we analyze NI S_{max} in parallel with the open-ocean S_{max} because this contrast demonstrates how the annual cycle of vertical diffusion is influenced by the annual cycle of SHF.

Fig. 7 of Bingham et al. (2012) shows that in the regions eastward and poleward of the open-ocean S_{max}, a vertical flux term, $([\partial h']/\partial t)(\partial \bar{S})/\partial z$, where h' is the seasonal variation of the MLD, dominates their SLS budget in winter and spring. While this process is captured in the entrainment term, Bingham et al. describe it as a "seasonal heaving of the mixed layer." We begin by interpolating the vertical diffusion term in the model output to the depth of the mixed layer (Fig. 1.7), which demonstrates that on the eastward and poleward regions of the S_{max}, there is indeed a vertical flux of S through the base of the mixed layer into the deeper ocean. Since this process coincides with wintertime surface cooling and a decrease of $\partial_z \theta$, we also compute R_ρ and use Eq. 1.2 to determine

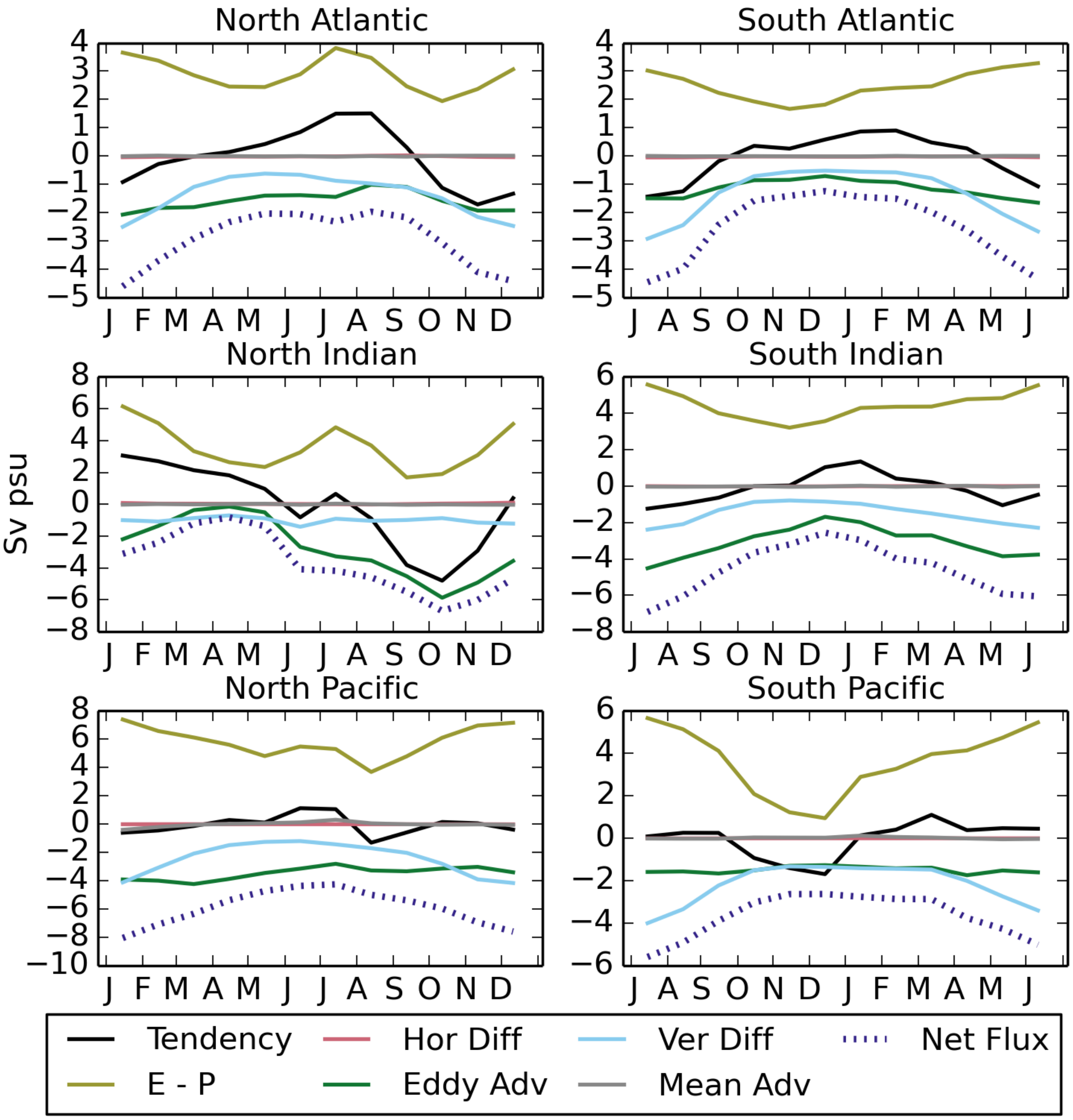

Figure 1.6: The climatological annual cycle of the salinity budget (Sv psu) for each S_{max}. The net flux term is the sum of horizontal diffusion, eddy advection, and vertical diffusion.

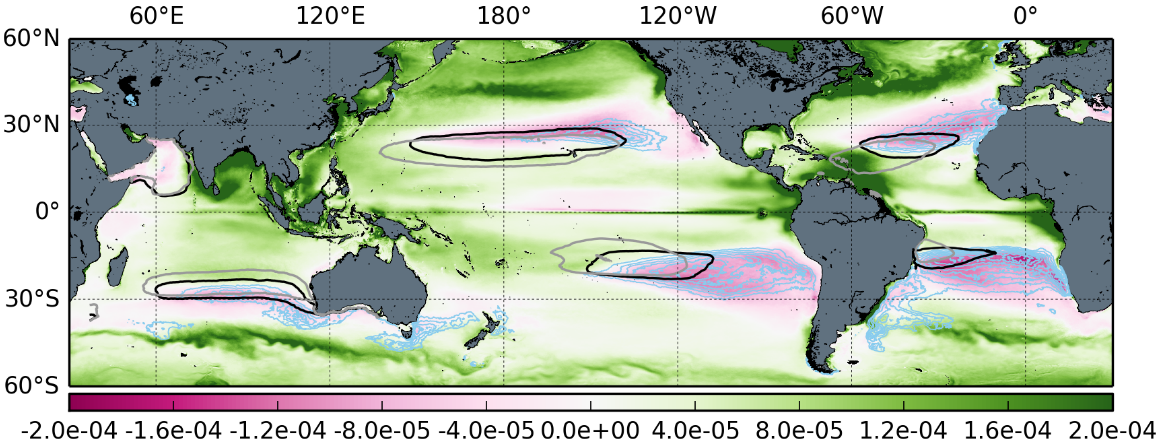

Figure 1.7: The simulation's climatological mean vertical diffusive flux of salt though the base of the mixed layer (psu m/s, shaded). Black and gray contours are isohaline contours as in Fig. 1.3. Light blue contours are regions where salt finger convection penetrates the base of the mixed layer. In the vicinity of the S_{max} these regions of salt finger convection are on the eastward and poleward edges of each S_{max} & correspond with regions of negative vertical diffusive salt fluxes through the mixed layer base (magenta shaded regions).

the regions where salt finger convection enhances diffusivity at the base of the mixed layer.

In the NA, NP and SP, these areas of S flux from the mixed layer into the ocean interior coincide with the regions of Type II MW formation. MWs are typically characterized using the planetary component of potential vorticity,

$$PV = \frac{f}{\rho}\frac{\partial \rho}{\partial z} \tag{1.9}$$

where f is the Coriolis parameter. PV is used in the study of MW since it quantifies vertical stability, is approximately conserved in geostrophic flow and is generally much larger in magnitude than the relative potential vorticity component (Hanawa and Talley, 2001). To account for the cross-equatorial change in the sign of f we use $|PV|$ in computations but refer to it as PV within the text. Type II MWs have a "core" (depth of minimum PV) found around 75-100 m during the late winter. While studies use different values of PV to demarcate the boundaries of mode waters, we use the value of Wong and Johnson (2003), where $|PV| < 3 \times 10^{-10} m^{-1} s^{-1}$, to examine the extent of low-PV water in all basins.

Since the contrasting regions of stability are on diagonally opposite sides of the open-ocean S_{max}, we create depth transects through each S_{max} (Fig. 1.8 & 1.9) along the paths in Fig. 1.3. Low-PV water forms in the surface layer along each transect however, the waters beneath these low-PV regions generate salt finger convection only on the eastward and poleward sides of the open-ocean

S$_{max}$. When low-PV water forms on the westward and equatorward side of the S$_{max}$, as visible in NP and SP, the waters underlying these low-PV volumes do not generate salt finger convection because $\partial_z S$ is stabilizing above the STUW. Similarly, the waters within NI S$_{max}$ are not susceptible to salt finger convection because $\partial_z S$ is weak. We also depict the seasonal evolution of the mixed layer depth and the salt finger convection diffusivity at intervals during the winter and spring. The NH (SH) open-ocean S$_{max}$ show mixed layer deepening from January through March (July through September) and rapid shoaling from March through May (September through November). Salt finger convection forms above the mixed layer base in January (July), penetrates the mixed layer base in March (September), and dissipates below the shoaled mixed layer in May (November). This process is depicted in a simplified schematic in Fig. 1.10.

Though we have not computed a buoyancy budget in this study, it is important to note that the locations of these regions where the waters become susceptible to salt finger convection are significant because of the connection between Type II MWs and the descending branch of the STCs. This seasonal propagation of salt finger convection provides a diapycnal mixing pathway that transforms near-surface water into deeper, subsurface Central Water. Furthermore, since it mixes density upgradient, the newly transformed Central Waters can escape reentrainment when the mixed layer deepens in subsequent winters.

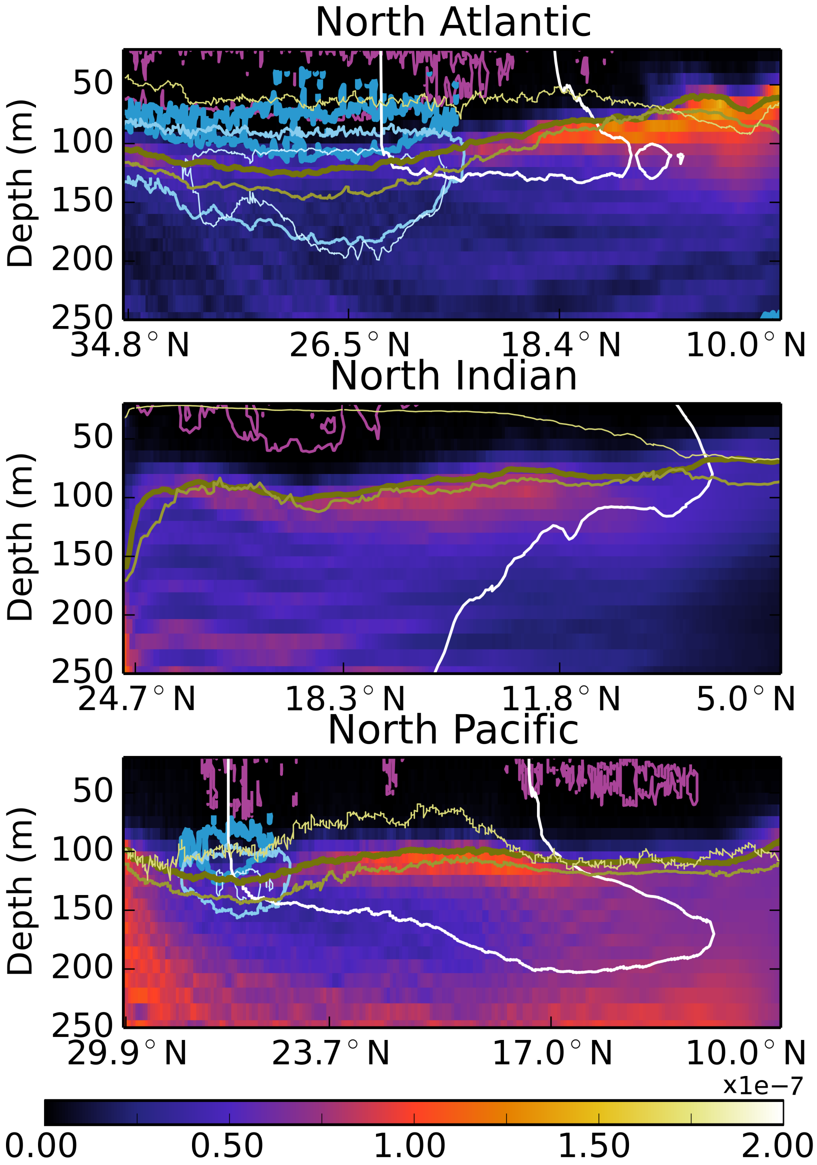

Figure 1.8: Transect plots through each NH S$_{max}$ along the paths shown in Fig. 1.3. Climatological January PV (m^{-1}s^{-1}, shaded), isohaline bounding each S$_{max}$ (white contours) and volumes where $|PV| < 3.0 \times 10^{-10} m^{-1} s^{-1}$ (magenta). Climatological mixed layer depth for January, March and May is shown by mustard yellow contours ranging from dark/thick to light/thin. Climatological areas of salt finger convection for January, March and May are shown by blue contours ranging from dark/thick to light/thin.

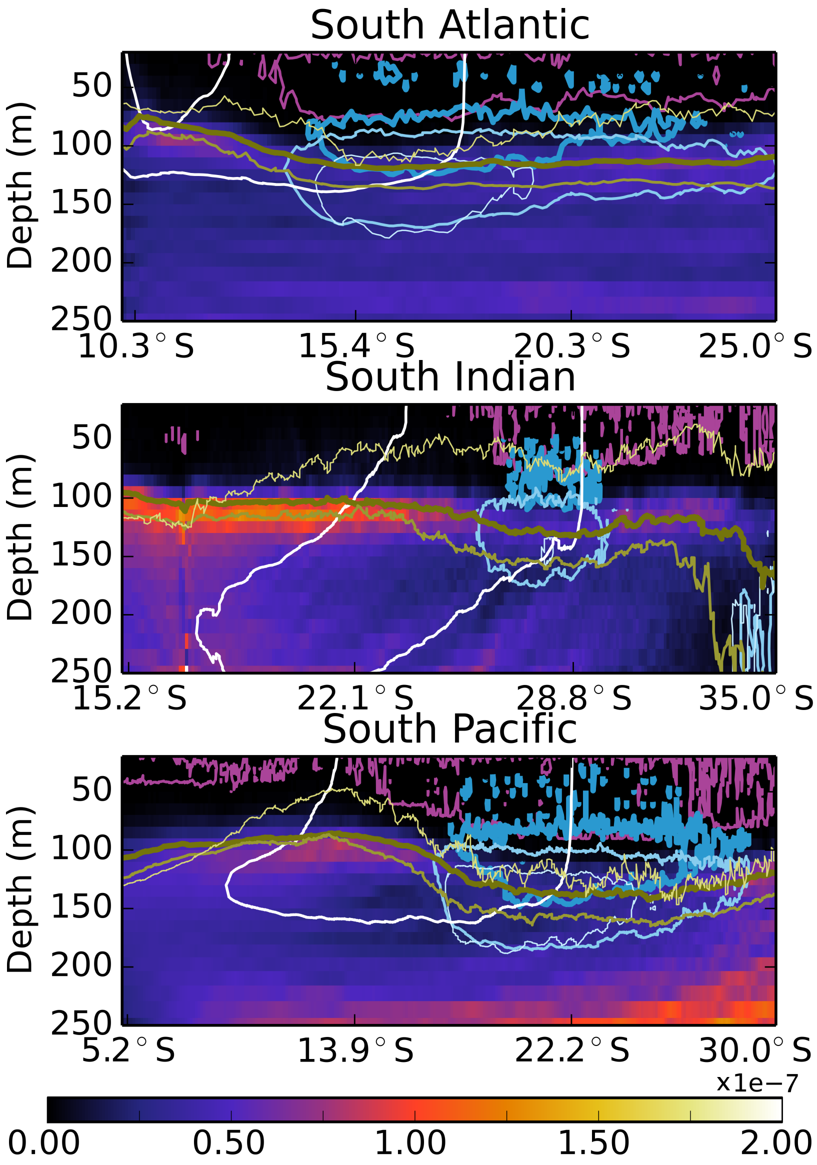

Figure 1.9: Transect plots through each SH S_{max} along the paths shown in Fig. 1.3. Climatological July PV ($m^{-1}s^{-1}$, shaded), isohaline bounding each S_{max} (white contours) and volumes where $|PV| < 3.0 \times 10^{-10} m^{-1}s^{-1}$ (magenta). Climatological mixed layer depth for July, September and November is shown by mustard yellow contours ranging from dark/thick to light/thin. Climatological areas of salt finger convection for July, September and November are shown by blue contours ranging from dark/thick to light/thin.

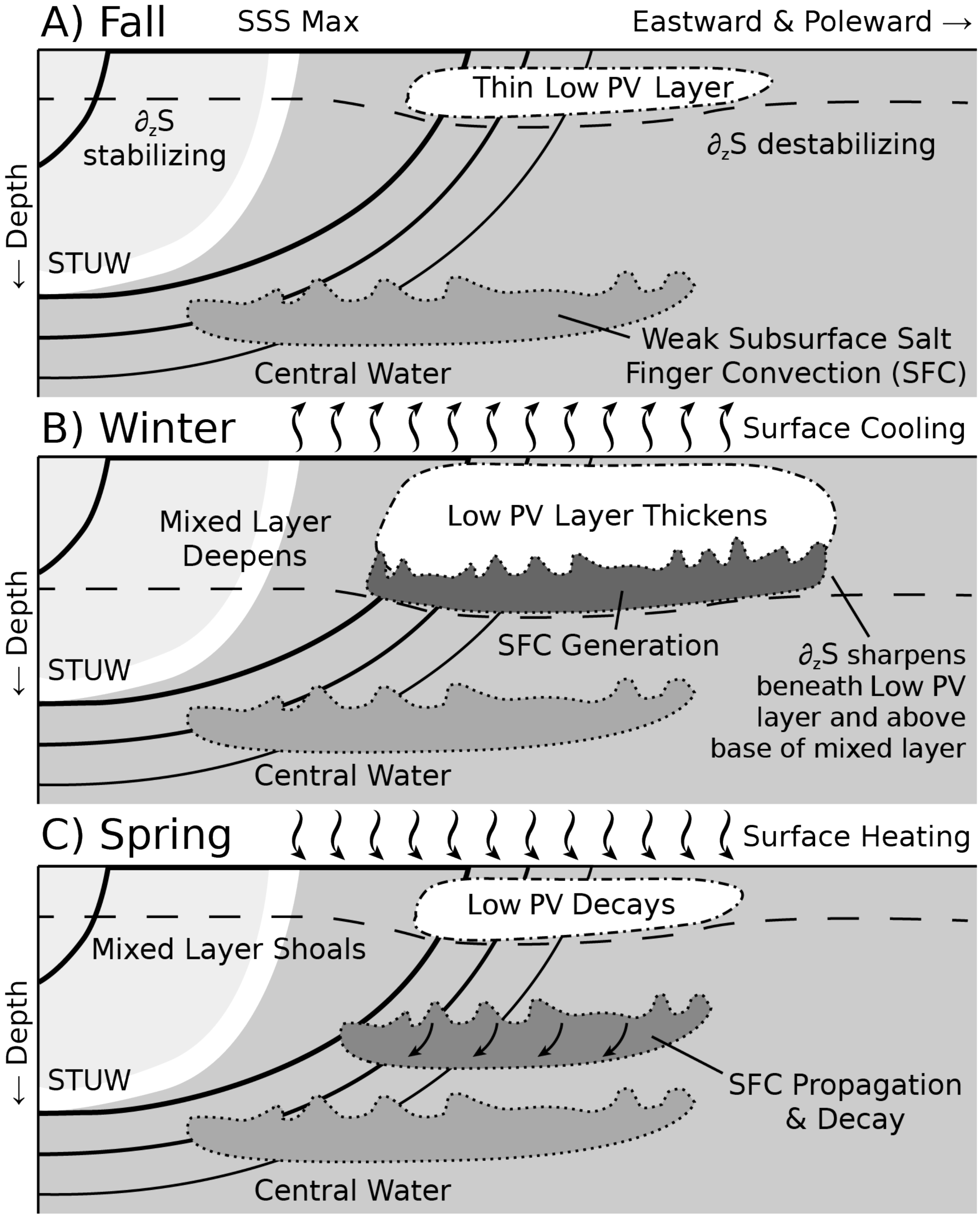
A) Fall
SSS Max
Eastward & Poleward →
Thin Low PV Layer
$\partial_z S$ stabilizing
$\partial_z S$ destabilizing
↓ Depth
STUW
Weak Subsurface Salt Finger Convection (SFC)
Central Water
B) Winter
Surface Cooling
Mixed Layer Deepens
Low PV Layer Thickens
SFC Generation
$\partial_z S$ sharpens beneath Low PV layer and above base of mixed layer
↓ Depth
STUW
Central Water
C) Spring
Surface Heating
Low PV Decays
Mixed Layer Shoals
↓ Depth
STUW
SFC Propagation & Decay
Central Water

Figure 1.10: A simplified schematic of the seasonal deepening of the mixed layer. The solid lines depict isohaline contours. Dashed-dotted lines surrounding the white volumes depict low-PV layers. Dotted lines surrounding dark gray volumes depict areas of salt finger convection.

1.5 Argo Float Selection and Analysis

The mixed layer deepening mechanism described in Section 1.4.4 is significant because it demonstrates how the annual cycle of the salinity budget, Type II MW formation, diapycnal mixing induced by salt finger convection and the descending branch of the STC may be connected. However these results come with the caveat that the model has a low SLS bias in this region. We reinforce our results using Argo (Roemmich et al., 2009) profiles to demonstrate that this process can be observed in situ. This analysis follows Johnson (2006) for SP and Toyama and Suga (2010) for NP and shows that the process occurs on the eastward and poleward edges of all five open-ocean S_{max}.

1.5.1 Float Selection and Methodology

We select Argo floats along the eastward and poleward edges of each MIMOC S_{max} outcrop. To provide assurance that the observed processes are not merely single-year anomalies (since this study attempts to explain processes in the climatological annual cycle) we select Argo floats that remain in the region long enough to provide approximately two years of data (73 depth profiles). As a consequence of this requirement, the Argo data are reported with varying start and stop dates. Table 1.3 displays the ID numbers and duration of data analyzed from each float. The white areas in Fig. 1.5 depict the path each float traversed during this duration. We follow the analysis of Section 1.4.4, using Eq. 1.2 to parameterize the salt finger convection diffusivity and Eq. 1.9 to detect the presence of low-PV water masses using the same value as in Section 1.4.4, $|PV| < 3\times10^{-10} m^{-1}s^{-1}$. There are many methods for determining the depth of the mixed layer from in situ data (de Boyer Montégut et al., 2004); we employ the criterion of Monterey and Levitus (1997) who use a threshold method specifically for the study of subtropical MWs: the base of the mixed layer is the pressure at which a profile's σ_θ increases from its linearly extrapolated surface value by a set interval, $\delta\sigma_\theta$=0.125 kg m^{-3}.

1.5.2 Argo Results

The Argo data (Fig. 1.11) from the open-ocean S_{max} depict a buildup of a low-PV layer within mixed layer as it gradually deepens in response to surface cooling throughout the winter months. Salt finger convection diffusivity peaks beneath the low-PV layer and above the base of the mixed layer as the mixed layer restratifies in the late spring. Salt finger convection diffusivity persists

Table 1.3: The Float ID #s and data duration for the Argo data include in Section 1.5. Each float provides 73 profiles (approximately 2 years) of data within the eastward and poleward region of each S_{max}.

Smax	*Float ID*	*Start (YYYY-MM-DD)*	*End (YYYY-MM-DD)*
NA	4901588	2013-09-23	2015-09-10
SA	1901001	2013-12-23	2015-12-13
NI	2901340	2011-12-25	2013-12-14
SI	5901711	2010-01-26	2012-01-16
NP	5903597	2011-11-11	2013-11-12
SP	3900664	2008-01-14	2010-02-20

year-round but weakens throughout the summer months. The open-ocean S_{max} have relatively deep maximum mixed layer depths: NP and SP ~160 dbar; SA and NA ~225 dbar; and SI ~240 dbar. In the NI S_{max} profiles, the maximum mixed layer depth is much shallower (reaching ~90 dbar); the salt finger convection diffusivity is both weak and inconstant.

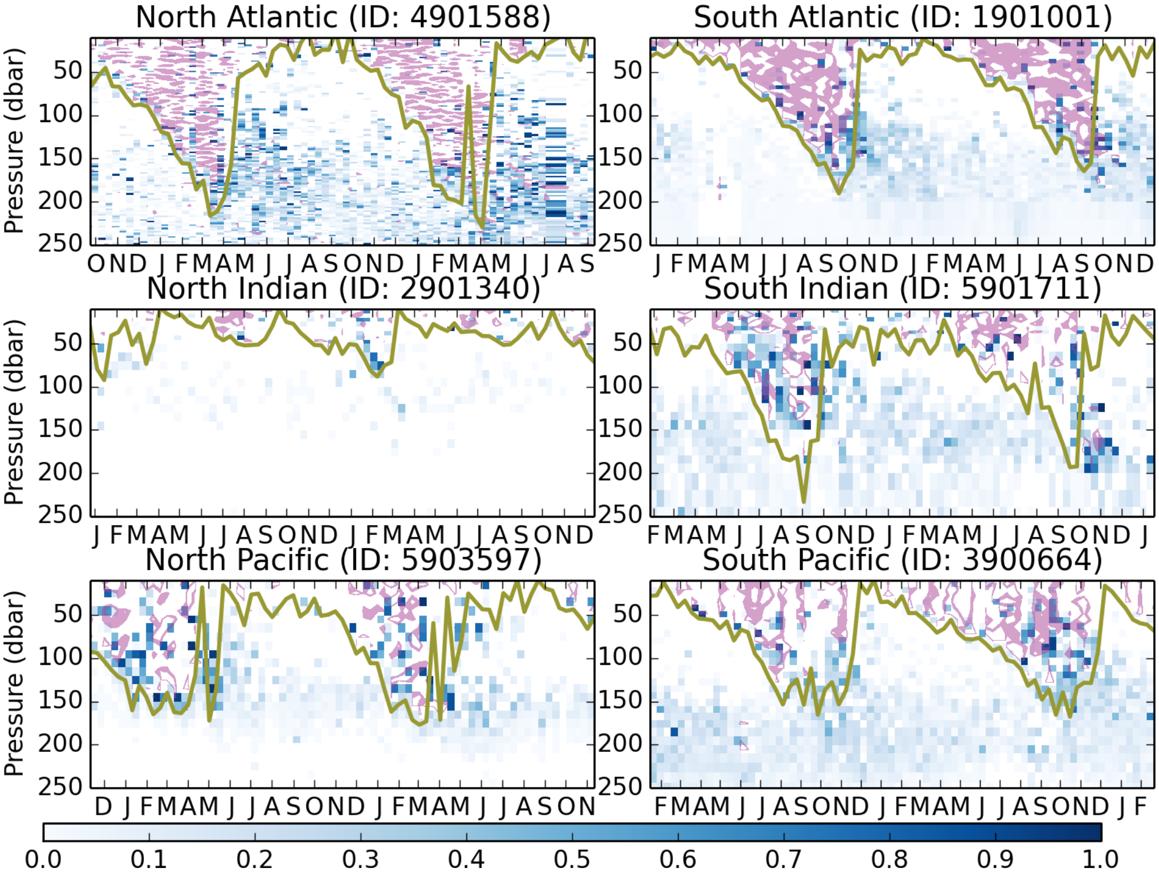

Figure 1.11: 73 depth profiles from each of the Argo floats with data durations listed in Table 1.3. Depths where $|PV| < 3.0 \times 10^{-10} m^{-1} s^{-1}$ depicted in magenta. Salt finger convection diffusivity as estimated by 1.2 (blue shading). Depth of the mixed layer depicted in mustard yellow.

1.6 Summary and Conclusions

This study aims to determine the relative importance of internal ocean processes for balancing climatological annual mean E-P fluxes and to explain why, in spite of their different annual cycles of E-P, the SLS of all six S$_{max}$ reaches a maximum in local fall and minimum in local spring. Eddy advection plays a primary role in the climatological balance of E-P fluxes, from a high of balancing 77% of climatological annual mean E-P for NI S$_{max}$ to a low of 41% for SP S$_{max}$. Vertical diffusion also plays a significant role in balancing E-P fluxes, from a high of 60% for SP S$_{max}$ to a low of 28% for NI S$_{max}$. The climatological annual mean tendency term is of the same sign as E-P fluxes for all six S$_{max}$, indicating that they all increased in mean S during the integration. This is consistent with the observed pattern amplification of SLS (Durack and Wijffels, 2010) but may be a consequence of model drift (Durack et al., 2013). The horizontal diffusion term is negligible in the budgets of all six S$_{max}$.

While the SLS of all six S$_{max}$ reaches a maximum (minimum) in local fall (spring), the salinity budget of NI S$_{max}$ is distinct: its annual cycle of net flux into the ocean interior is dominated by eddy advection. The annual cycle of SHF for NI S$_{max}$ is governed by the seasonal evolution of the monsoon circulation and thus it experiences a short period of surface cooling (typically from mid-November to early February) and relatively shallow mixed layers. The annual cycle of net flux in the open-ocean S$_{max}$ budgets is governed by a combination of eddy advection and vertical diffusion for SI S$_{max}$ and vertical diffusion for the remaining S$_{max}$.

The westward and equatorward displacement of STUW with respect to the surface outcrop of the open-ocean S$_{max}$ creates contrasting regions of stability in their vicinity. On the equatorward and westward regions $\partial_z S$ is stabilizing while on the eastward and poleward regions $\partial_z S$ is destabilizing. These regions of destabilizing $\partial_z S$ experience longer periods of wintertime surface cooling when compared to NI S$_{max}$ (typically four to six months) and develop thicker layers of near-surface low-PV water. This process gradually deepens the mixed layer and sharpens $\partial_z S$ below the "core" of the low-PV layer and above the base of the mixed layer. This makes waters susceptible to salt finger convection and enhances vertical diffusive fluxes of S from the S$_{max}$. The mixing induced by salt finger convection provides a diapycnal mixing pathway for near-surface low-PV waters to transform into subsurface Central Waters. These regions have been identified as Type II MW formation regions in NA (Joyce et al., 1998), NP (Ladd and Thompson, 2000), and SP (Wong and Johnson, 2003) and coincide with the source water regions of the descending branch of the STCs. Though our model results come with the important caveat that CESM has a low SLS bias in these regions compared to observations, this seasonal process is also observed in Argo floats.

This finding, that low-PV water is produced in response to wintertime surface cooling in regions of destabilizing $\partial_z S$ adjacent to the open-ocean S_{max}, has broader implications for our understanding of MW formation. A comparison of our Fig. 1.7 to Plate 5.4.3 of Hanawa and Talley (2001) shows that $\partial_z S$ tends to be stabilizing or neutral in Hanawa and Talley's Type I MW regions and the columns are not susceptible to salt finger convection except in the case of SA Subtropical MW (SA STMW). Unlike the other open-ocean S_{max}, SA S_{max} is located at the westward extent of the basin, and thus large areas within the central SA have destabilizing $\partial_z S$ and are susceptible to salt finger convection. This suggests that the Type II MW formation process may generate low-PV water in the central SA even though the classification implies that intense cooling associated with the Brazil Current is the source of low-PV for SA subtropical mode water (STMW).

Two other irregularities support this notion:

- Type I mode waters are typically uniform in ρ_θ. SA STMW is an outlier in this case because its ρ_θ is variable (Hanawa and Talley, 2001), a property generally associated with Type II MWs.
- Type I mode waters are typically associated with western boundary currents that experience intense wintertime SHF. Kållberg et al. (2005) estimate that the Kuroshio Current (adjacent to NP STMW) has a max wintertime SHF of -401 W/m^2 and the Gulf Stream Current (adjacent to NA STMW) has a max wintertime SHF of -396 W/m^2. In contrast, the Brazil Current (adjacent to SA S_{max}) has a max wintertime SHF of only -170 W/m^2.

The original study of MW in SA (Provost et al., 1999) was based on a sparse dataset that predates the Argo era. This suggests that further study may reveal a more detailed distribution of MWs in SA, analogous to recent findings in the NP (Oka and Qiu, 2012). The existence of Type II MW in the central SA would provide further evidence of the connection between the STCs and Type II MWs. The source water region for the descending branch of the SA STC (Fig. 1 of Snowden and Molinari, 2003) corresponds to the Type II MW formation region in Fig. 1.7.

Our results come with two important caveats: the S fluxes due to salt finger convection are not differentiated from other contributions to vertical mixing in the diagnosed budgets, and the model has a low S bias in the regions eastward and poleward of the S_{max}. It should be possible to use the KPP mixing scheme to explicitly quantify the magnitude of S fluxes due to salt finger convection by exporting contributions to κ from each physical process in addition to the total vertical diffusion term. Additionally, St. Laurent and Schmitt (1999) developed Eq. 1.2 by considering mixing schemes in parameter space and found that in low Richardson number conditions, turbulent shear mixing best fit observations while in high Richardson number and low R_ρ conditions, salt finger mixing best fit observations. Our configuration of CESM (1.0.4) does not screen for low Richardson numbers before imposing Eq. 1.2. It would be prudent to run a sensitivity study in which low Richardson numbers are screened to see if this helps to mitigate the SLS bias in the vicinity of the S_{max}.

1.7 Chapter Acknowledgements

This work was done in collaboration with Dr. Frank O. Bryan, Dr. Seymon A. Grodsky and Professor James Carton. Two awards supported this research: S.A.G. was supported by NNX12AF68G and F.O.B. was supported by NNX10AC16G. The model integration described in this paper was carried out on Yellowstone (CISL, 2012; ark:/85065/d7wd3xhc) provided by CISL at NCAR, which is sponsored by NSF. Furthermore, we thank David Bailey for his assistance in keeping the model integration progressing. This chapter was published in the *Journal of Physical Oceanography* as Johnson et al. (2016). We found the comments from the two anonymous reviewers and the guidance of the editor to be invaluable.

Chapter 2

Salinity Budget of the Equatorial Pacific Salinity Minimum

2.1 Abstract

The surface waters of the Equatorial Pacific exhibit low salinities, as they underlie the annual migration path of the Intertropical Convergence Zone (ITCZ). Ekman transport plays a key role not only in the tropics, but in the larger coupled climate system by influencing the transition between warm and cold phases of ENSO. In the Central Pacific, winds are zonal and, north of the Equator, Ekman transport advects low salinity water northward. In the Eastern Pacific, winds are southerly and, in the absence of strong meridional advection, the surface waters form a distinct salinity minimum (S_{min}), known as the Eastern Pacific Fresh Pool (EPFP). We apply an isohaline budget to study the EPFP. The budget reveals that precipitation is primarily balanced by vertical diffusion in the EPFP.

2.2 Introduction

The Equatorial Pacific is a region where the influence of salinity sharply contrasts with its influence in the subtropics. Tropical waters underlie regions of atmospheric convergence and experience high annual mean rates of precipitation with a strong annual cycle. Mixed layers tend to be shallow, ranging from roughly 20m in the Eastern Pacific to 70m in the Central Pacific (de Boyer Montégut et al., 2004). Although surface waters are doubly stable (You, 2002) as temperature decreases and salinity increases with depth, incorporating the effects of salinity improves the performance of ocean models by reducing equatorial SST gradients, improving the fidelity of the representation of the cold tongue and enhancing Indonesian throughflow (e.g. Murtugudde and Busalacchi, 1998; Vossepoel and Behringer, 2000). The region is the equatorward edge of the STC (e.g. McCreary and Lu, 1994; Liu, 1994) and salinity anomalies generated in the subtropics can influence the dynamics of the equatorial regions (Schneider, 2004). Ekman advection has a large influence on the salinity budget of the region since in the Eastern Pacific prevailing winds are southerly (Kessler, 2006).

In the Eastern Pacific, the lowest salinity values in the tropics are found in the EPFP. Its boundaries are defined by the 34.0 psu isohaline outcrop (Bennett, 1963), but SLS values can decrease below 32 psu. The EPFP typically remains between the Equator and 15°N and its extent is limited by equatorial upwelling to south, the coasts of Central and South America to the North & East and the North Equatorial Counter Current (NECC) to the west (Kessler, 2002). While our interest in the EPFP is to contrast its salinity budget with those of the subtropical S_{max}, early studies in the region were motivated by its ecological significance (Wyrtki, 1964) since it envelops the Panama Bight – a large marine ecosystem for corals and plankton (Marra et al., 1987) and the developmental stages of several large fish species such as the Spanish mackerel, sierra and black skipjack tuna (Margulies, 1993). Only recently has work in the region focused on the effects of salinity. Alory et al. (2012) qualitatively described the seasonal SLS dynamics of the EPFP using data from the Soil Moisture and Ocean Salinity (SMOS) (Kerr et al., 2001) satellite. The Salinity Processes in the Upper Ocean Regional Study 2 (SPURS-2) field campaign (Schmitt et al., 2015) also studied a nearby region of low salinity centered around 10°N, 125°W near the highest regions of tropical precipitation. Yu (2014, 2015) describes a contrast in the seasonal behavior of the S_{min} and precipitation maximum. The precipitation maximum follows the movement of the ITCZ, oscillating (in the zonal mean) roughly from 5°N in March to 8°N in September while the S_{min} forms around 4°N in January and propagates monotonically north before dissipating at 11°N in the following March (Fig. 9 of Yu, 2015).

The current system of the Eastern Tropical Pacific is complex. It includes zonal surface currents: the NECC and the South Equatorial Current (Kessler, 2006); and seasonally generated eddies: the Costa Rica Dome and the Tehuantepec Bowl (Willett et al., 2006). With respect to ENSO, this region is where coastal Kelvin waves are believed to be reflected into off-equatorial Rossby waves, as described by Kirtman (1997).

Since salinity values form a distinct local minimum, the waters of the EPFP are suitable for study using an isohaline salinity budget formulation, which eliminates the effects of mean advection. The objective of this chapter is to describe the mean annual salinity budget of the EPFP and to understand how the tropical oceans balance the large annual cycle of precipitation. Since the EPFP is a local minimum bound by an isohaline surface, S_o=34.0 psu, we modify the salinity budget shown in Eq. 1.8 by flipping the sign of the inequalities in the integral limits to account for the distinction that the EPFP is a minimum rather than a S$_{max}$:

$$\begin{aligned}\iiint_{V(\bar{S}<S_o)} \frac{\partial \overline{S}}{\partial t} dv = -\iint_{\partial V(\bar{S}=S_o)} \overline{\mathbf{u}'S'} \cdot d\mathbf{a} + \iint_{\partial V(\bar{S}=S_o)} \overline{\left(\kappa \frac{\partial S}{\partial z} - \Gamma\right)\mathbf{k}} \cdot d\mathbf{a} + \\ \iint_{A(\bar{S}<S_o)} S_{ref}\overline{(E-P)} dA + \iiint_{V(\bar{S}<S_o)} A_S \nabla_h^4 \overline{S} dv\end{aligned} \tag{2.1}$$

2.3 Results

2.3.1 Climatological Simulation of the Eastern Pacific Fresh Pool

The model's simulated SLS agrees well with MIMOC observations in both its spatial extent and annual cycle of outcrop area (Fig. 2.1). The model matches the western and northern extent of the observed minimum (Fig. 2.1a). The MIMOC outcrop extends farther than the model along its southwest edge around 3°N-10°N and the model outcrop extends farther than MIMOC along the northwest edge around 12°N-18°N. The California Current advects low salinity water along the coast of Baja California (34.0 psu at the top of Fig. 2.1a). Since this water mass is distinct from the EPFP it is excluded from the budget. The outcrops agree well in surface area throughout the year, although CESM exhibits a slightly larger surface area in January and February (Fig. 2.1b). The outcrops both reach their minimum extent in April and their maximum in November. The magnitude of surface flux from COREv2 peaks in July and the lowest values of SLS and the largest spatial extent of the outcrop is in the late fall (Fig. 2.2). The simulation's seasonal cycle of sea surface height (SSH) anomalies (Fig. 2.3) compare well with observations (e.g. Fig. 7 of Kessler, 2006). The Costa Rica Dome strengthens seasonally, with a maximum intensity in boreal fall and winter. The Tehuantepec Bowl strengthens and the NECC decays in boreal spring.

2.3.2 Salinity Budget of the Eastern Pacific Fresh Pool

The annual cycle of the salinity budget shows that the surface flux term is balanced primarily by the tendency term (Fig. 2.4). The tendency term is negative from early May through November while the surface flux term is positive from the beginning of January through mid-April and negative throughout the remainder of the year. The annual cycle of the surface flux term is primarily caused

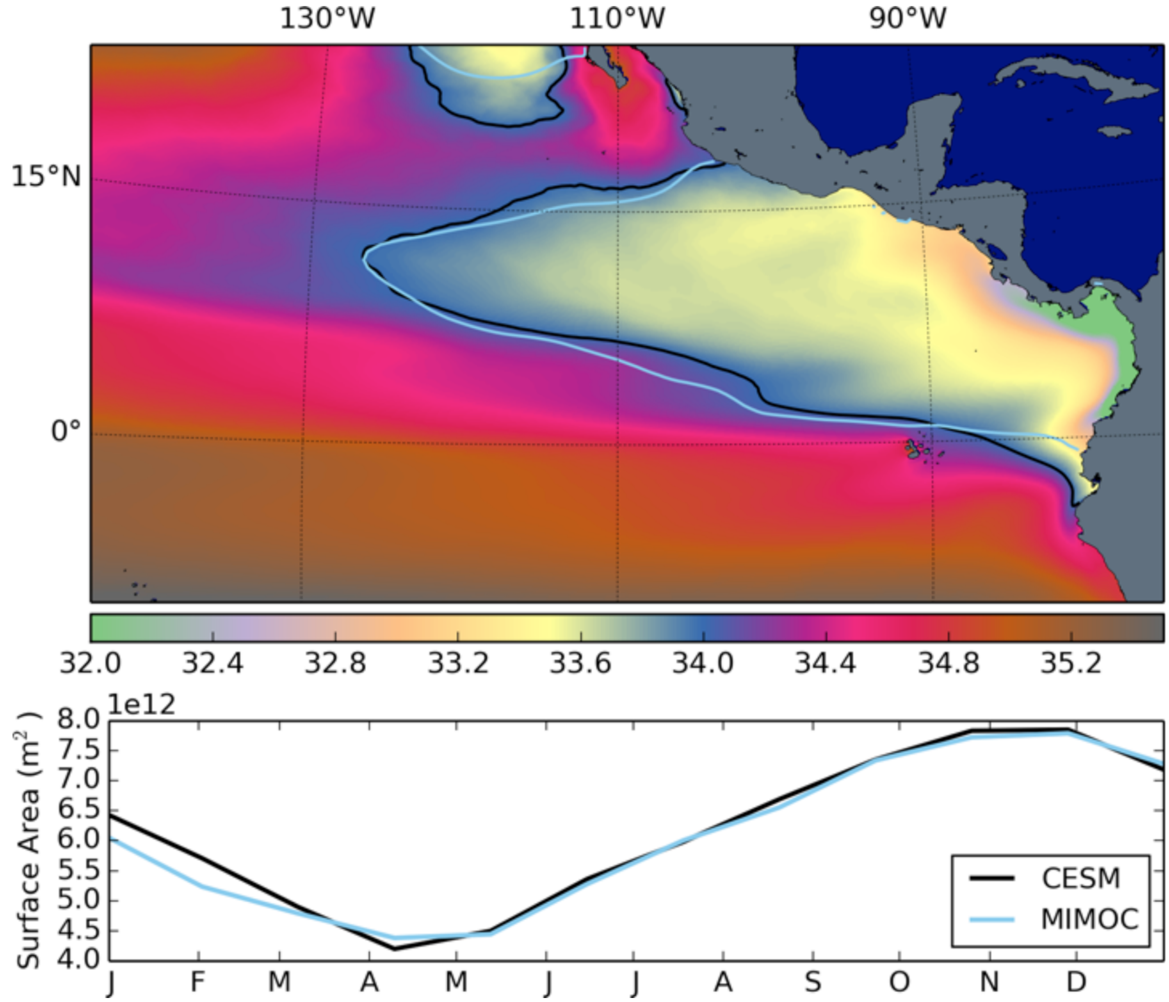

Figure 2.1: (a) Climatological model SLS (shaded, psu) and mean 34.0 psu contours for the simulation (black) and MIMOC (light blue). (b) Surface area bound by each of the outcrops in (a) as a function of month.

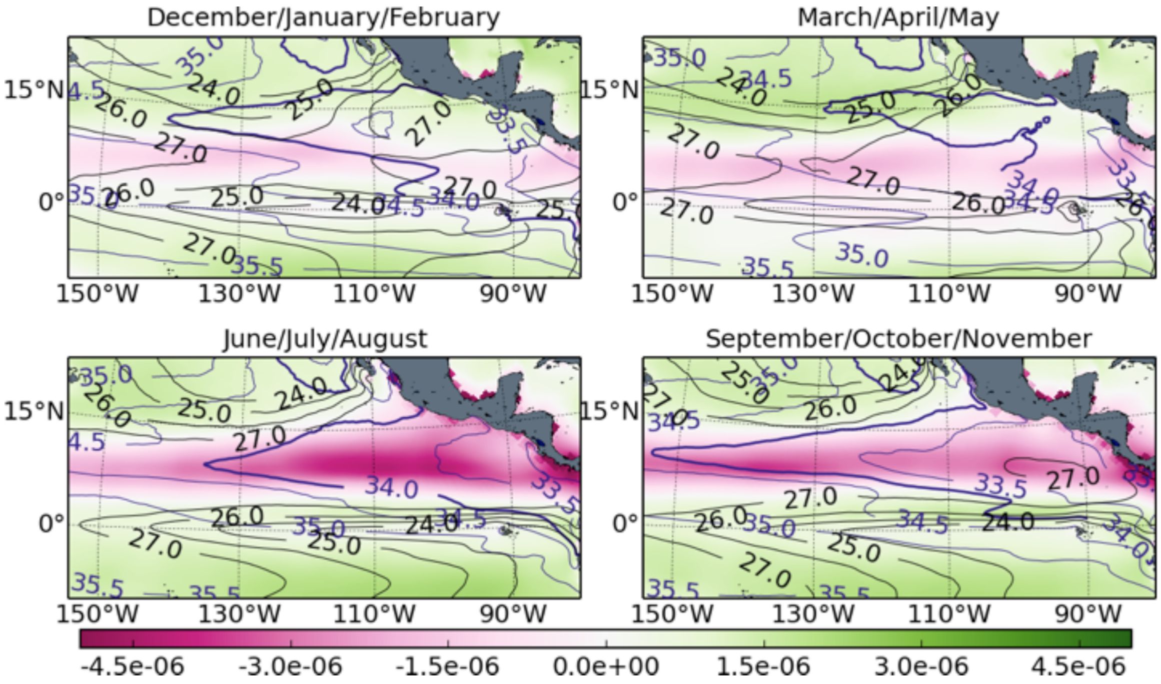
December/January/February
March/April/May
June/July/August
September/October/November
15°N
0°
150°W
130°W
110°W
90°W
-4.5e-06
-3.0e-06
-1.5e-06
0.0e+00
1.5e-06
3.0e-06
4.5e-06

Figure 2.2: Annual cycle of surface flux (shaded, psu m/s) with isohaline contours in purple (psu) and isotherms in black (°C).

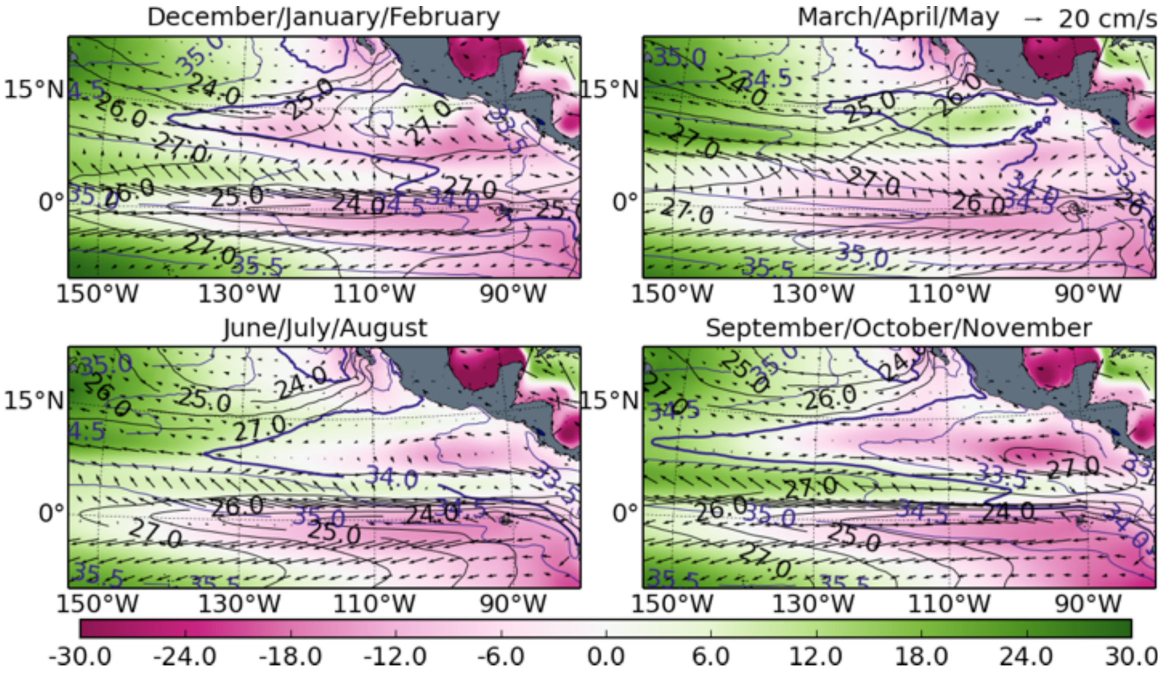
December/January/February
March/April/May
→ 20 cm/s
June/July/August
September/October/November
15°N
0°
150°W
130°W
110°W
90°W
-30.0
-24.0
-18.0
-12.0
-6.0
0.0
6.0
12.0
18.0
24.0
30.0

Figure 2.3: Annual cycle of SSH anomaly (shaded, cm) with surface velocity vectors (cm/s) and isohaline contours (purple, psu).

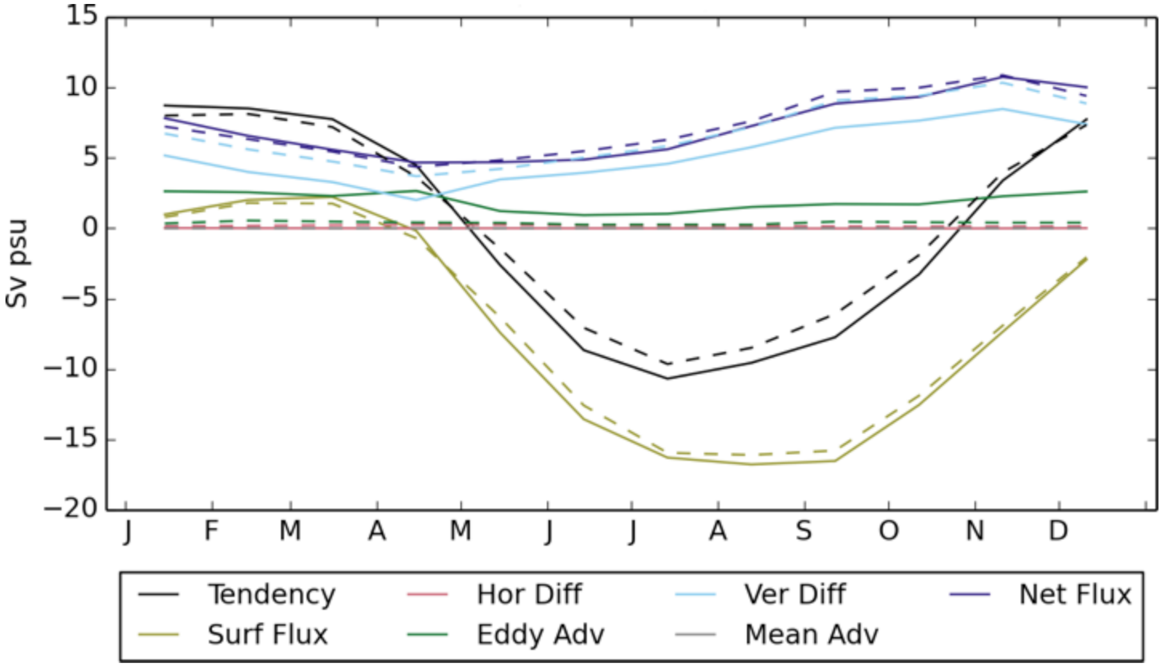

Figure 2.4: The annual cycle of salt budget terms (Sv psu) of the salinity budget volume-averaged within the 34.0 isohaline contour computed on 5-day data and averaged into monthly means (dashed lines) and computed on climatological monthly mean data (solid lines).

by the ITCZ's seasonal enhancement of precipitation over the EPFP, which peaks in the boreal summer and fall (Fig. 2.2).

The horizontal diffusion term is negligible and the vertical diffusion term is roughly sinusoidal. The peak and trough of the vertical diffusion term roughly coincide with the change in sign of the tendency term: the trough (peak) of the vertical diffusion term is in mid April (November), which is in rough coincidence with the change in sign of the tendency term from positive to negative (negative to positive) in early May (late October). This relationship suggests that the magnitude of the vertical diffusion term is in simple balance with the surface salinity.

To examine this relationship further we to create spatial maps of the pattern of vertical diffusive flux through the base of the mixed layer (Fig. 2.5). There is a zonal gradient of mixed layer depth with depths generally decreasing to the East. The mixed layer shoals in regions of lower SLS due to the increased stratification caused by the enhanced negative vertical gradient of salinity. We also examine the annual cycle of the vertical salinity gradients and vertical diffusion (Fig. 2.6) by depicting a time versus depth plot at 10°N and 110°W (denoted by the black marker in Fig. 2.5). During the fall months, the mixed layer shoals in response to increased stratification due to the

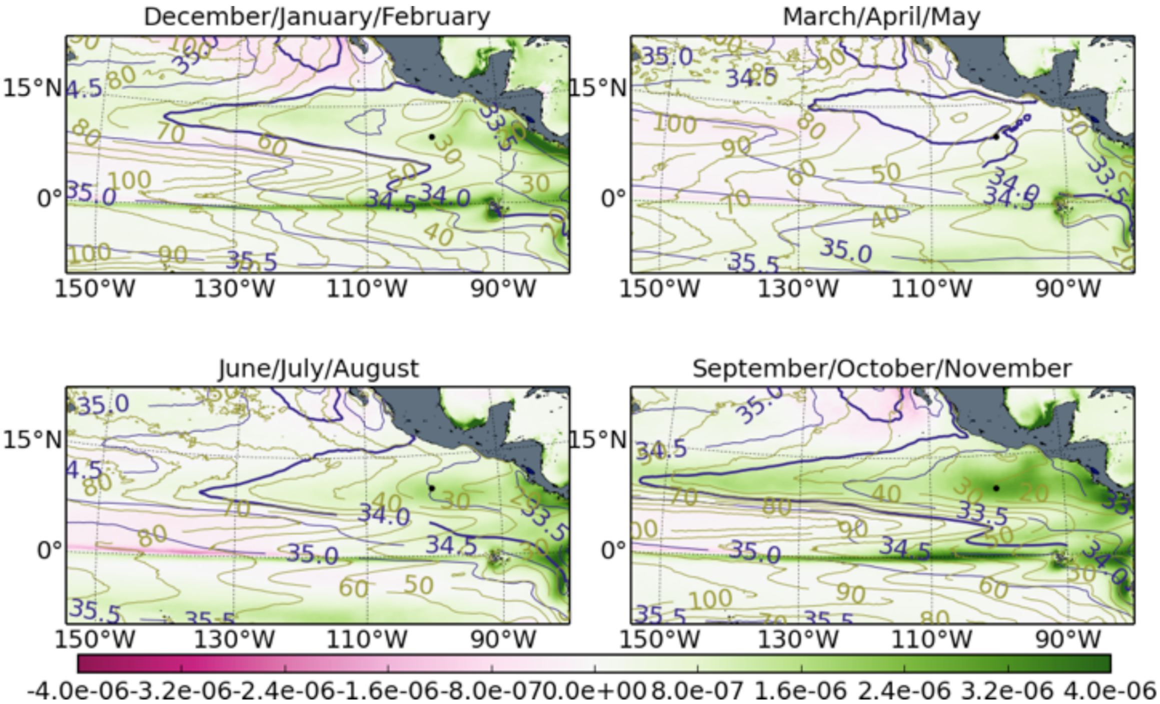
December/January/February
March/April/May
June/July/August
September/October/November
15°N
0°
150°W
130°W
110°W
90°W
-4.0e-06
-3.2e-06
-2.4e-06
-1.6e-06
-8.0e-07
0.0e+00
8.0e-07
1.6e-06
2.4e-06
3.2e-06
4.0e-06

Figure 2.5: The seasonal mean patterns of vertical diffusive flux through the base of the mixed layer (shaded, psu×m/s). Seasonal mean isohalines in purple and seasonal mean mixed layer depth in mustard.

freshwater flux. Thus enhanced diffusion is the direct result of the seasonally enhanced $\partial_z S$.

The difference between the versions of the salinity budgets (Fig. 2.4) allows us to infer the effect of high-frequency phenomena, such as mesoscale eddies and tropical instability waves, upon mixing. We see that the primary difference is that when the climatological monthly mean budget is compared to the 5-day budget using Eq. 2.1, eddy advection is enhanced and vertical diffusion is weakened in the climatological budget. These results are consistent with those in Chapter 1, suggesting that high-frequency phenomena enhance local gradients of salinity, which vertical mixing then acts upon.

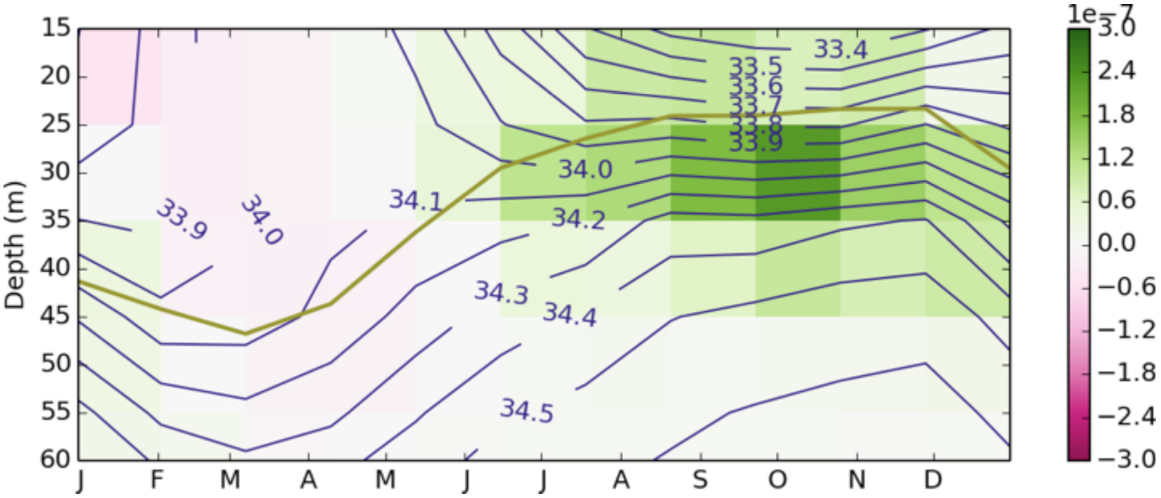

Figure 2.6: The annual cycle of vertical diffusion (shaded, psu/s) as a function of depth at 10°N and 100°W (depicted by the black marker in Fig. 2.5). Isohaline contours in purple, mixed layer depth in mustard.

2.4 Discussion

The tropical Pacific is a region in which the role salinity plays upon the vertical stability of the water column is different than in the subtropics. Since the waters of the EPFP are doubly stratified, rather than having an unstable $\partial_z S$ component as in the subtropical S_{max}, the inferences we make from the salinity budget are more limited. The salinity budget of the EPFP is dominated by the large annual cycle of precipitation beneath the path of the ITCZ. Because of the overwhelming influence of precipitation, properly accounting for the effects of salinity on stratification in the EPFP should improve our ability to forecast ENSO transitions by improving the representation of the Equatorial Undercurrent. For example, in low-resolution models, the meridional shear in the vicinity of the EPFP is too weak when compared against observations (Tseng et al., 2016).

In the EPFP the annual cycle of precipitation is compensated seasonally by local tendency and dissipated primarily by vertical diffusion. While the annual amplitude of the tendency term is large, we see after taking annual means of the climatological time series in Fig. 2.4, that the surface flux is primarily balanced by vertical diffusion (81%), eddy advection (15.5%) and tendency (3.5%).

Despite these limited insights, the application of the salinity budget to the EPFP provides a candid check on the validity of the salinity budget methodology – it provides results that are straightforward to interpret.

Chapter 3

Hypothesis Testing and Climate Change: Four Complications (and How to Account for Three of Them)

3.1 Abstract

Statistical hypothesis tests are used to infer changes in Earth's climate. Typically, a test statistic computed from data is compared against a null distribution to determine whether a change or trend observed in the data is statistically significant. However, the null distributions used in these tests are often estimated without considering how complications present in climate data – autocorrelation and measurement error – affect the variance of samples and the shape of the null distribution. These complications increase the variance of samples taken from the data and increase the width of the null distribution. Therefore, neglecting their effects results in overestimating the significance of changes or trends computed from the data. We consider time series of ocean temperature and salinity data and generate synthetic time series mimicking the properties of observational time series to illustrate these concepts. We then demonstrate how to account for the aforementioned complications. Next, we discuss two methods for handling other aspects of climate analysis: evaluating the significance of multiple tests conducted simultaneously and determining when a linear regression is an appropriate model for inferring the presence of a trend in a particular time series. After illustrating these concepts, we return to analyzing the time series of ocean temperature and salinity data and apply the methods necessary to account for autocorrelation, measurement error and multiple simultaneous tests. We discuss how the conclusions of many studies that infer significant changes in ocean salinity and the hydrological cycle should be reevaluated.

3.2 Introduction

Statistical hypothesis tests are the principle tool used to infer changes and trends in Earth's climate. Conducting a hypothesis test requires an analyst to formulate a null hypothesis (typically that a change or trend is not present in the data), compute a test statistic from the data and then compare it against a null distribution. If the test statistic falls within a sufficiently improbable region of the null distribution, then the null hypothesis is rejected and the analyst claims that a statistically significant change or trend has been observed.

While these steps are familiar to anyone acquainted with the rudiments of statistical analysis, the complications that arise when analyzing climate data are often overlooked. In particular, the techniques used by many analysts to estimate the shape of the null distribution require that the data being analyzed are independent of each other (lacking in correlation) and are measured without error. These requirements are usually not met in climate analysis, since climate data are spatially and temporally correlated and possess non-negligible measurement error.

The presence of autocorrelation and measurement error in data affects the distribution of samples collected from it. The distribution of samples from such data possesses a larger variance than samples taken from data that are independent and measured without error. Since the consequences of these complications are unfamiliar to many analysts, we thoroughly discuss their effects in the background section of this study. Within that section, we use synthetic time series (which allow us to specify the autocorrelation functions and error magnitudes) as a pedagogical tool to illustrate the effects of the complications and demonstrate how to account for them when constructing a null distribution.

Linear regressions are often used to determine whether trends are present in time series. In addition to the complications described above, regression analysis poses another complication that must be addressed: determining whether a linear model is appropriate for characterizing the data under analysis. Several conditions must be met in order to accurately estimate the null distribution of the regression slope. When these conditions are not met, a phenomenon known as model misspecification (Harvey and Collier, 1977), the estimate of the regression slope is biased and thus it is not possible to use standard techniques to determine whether a given regression slope is significantly different from zero (Draper and Smith, 1998). Since linear regressions are so commonly employed in the context of climate analysis, we demonstrate the approach of Harvey and Collier. However, model fitting is an expansive topic, so we restrict our discussion to linear models, leaving non-linear approaches such as those discussed by Barnett (1984) and Ghil et al. (2002), among others, beyond the scope of our discussion.

We analyze climatological data from two fields in the ocean, SST and SLS, to demonstrate these ideas. Changes in SST are related to global temperature changes and are comprehensively described in the literature. Changes in ocean salinity have been studied with the intention of using them to detect changes in the Earth's hydrological cycle (Held and Soden, 2006). Such changes are expected to manifest as shifts in the broad patterns of E-P. Indeed, many studies of ocean salinity report broad, statistically significant changes in the salinity field (Boyer et al. 2005, Tesdal et al. 2018) and then conclude that these changes are related to a changing hydrological cycle (Hosoda et al. 2009, Durack and Wijffels 2010, Helm et al. 2010, Skliris et al. 2014). These studies, however, do not account for autocorrelation, measurement error, and model misspecification when conducting their hypothesis tests.

Beyond the evaluation of hypothesis tests lies a broader challenge. When evaluating climate data, analysts often pose a separate, more complicated question: are the global changes or trends observed in a two-dimensional field comprised of individual time series significant? The SST and SLS fields can be thought of as being comprised of individual grid points each possessing a local time series. If the null hypothesis is rejected for subset of these local time series, how does an analyst determine whether significant global changes have occurred in each field?

This type of question has a long history within climate analysis. Walker (1914) realized that an analyst evaluating multiple hypothesis tests is increasingly likely to observe improbable test statistics as the number of tests increases. He formulated a criterion for evaluating individual hypothesis tests that becomes more stringent as the number of tests increases; Katz and Brown (1991) and Wilks (2016) provide longer discussions of this phenomenon and discuss Walker's criterion for evaluating it. Livezey and Chen (1983) introduced another approach to this problem by attempting to estimate whether the number of locally significant changes (or correlations, in their study) was itself significant, an approach they termed the detection of "field significance."

We describe an alternative technique, first introduced in the medical literature by Benjamini and Hochberg (1995), which focuses on controlling what is known as the FDR or controlling the rate at which null hypotheses are erroneously rejected. Ventura et al. (2004), Wilks (2006) and Wilks (2016) discuss the application of Benjamini and Hochberg's approach to geospatial data in order determine field significance and describe a methodology that is applicable even in the presence of spatial correlation.

These four complications – autocorrelation, measurement error, multiple testing, and model misspecification – greatly influence the outcome of hypothesis testing, yet they are rarely discussed within the literature concerned with the ocean's climate. We explain techniques for accounting for the first three of these complications within typical hypothesis tests. The last complication, model misspecification, is extensively described within the statistical literature (e.g. Ramsey 1969, Brown et al. 1975, Harvey and Collier 1977, White 1982, Draper and Smith 1998). We describe a technique for identifying model misspecification so that analysts can determine when linear regressions are an appropriate tool for inferring the presence of trends. However, accounting for the effects of model misspecification within hypothesis tests is a formidable task that is deserving of consideration in a separate study.

We apply the above techniques to an observational data set of ocean SST and SLS (Good et al., 2013) and demonstrate that the statistically significant changes observed in the ocean salinity field are not present at the levels described by prior studies when the effects of autocorrelation, measurement error and multiple testing are taken into account.

3.3 Background

3.3.1 Hypothesis Testing

We begin with a review of the steps involved in statistical hypothesis testing so that when we discuss the effects of autocorrelation and measurement error it is clear where, exactly, their effects must be accounted for when formulating a test.

Hypothesis tests generally involve five steps (Wilks, 2011):

1. Select a test statistic that is capable of addressing the research question. In climate studies, this test statistic is often the difference of mean values of data collected over two distinct time periods or the slope of the best-fit line through a time series.

2. State a null hypothesis. For our test statistics mentioned above, the null hypothesis would be that the difference of mean values is zero or the slope of the best-fit line is zero.

3. State an alternative hypothesis. This step determines whether or not the test should be one- or two-sided. For example, if our alternative hypothesis states that the slope of the best-fit

line should be positive (the time series increases in value as time passes) then the alternative hypothesis would not be confirmed if the slope is negative even if the magnitude of the slope is improbably large.

4. Determine the null distribution of the test statistic. The null distribution is the sampling distribution of the test statistic, presuming the null distribution is true. In many studies the null distribution is estimated using a parametric distribution. In practice, this step is the most difficult but crucial step in the formulation of a hypothesis test.

5. Use the null distribution to ascertain how probable it would be to observe the test statistic, assuming the null hypothesis true. This probability is known as the p-value. If the p-value is less than a specified threshold, α (which is also known as the level of the test), the null hypothesis is rejected.

While these steps seem straightforward, step 4 is often more difficult than analysts realize. The null distribution is usually determined using a parametric probability distribution function, often using either a t distribution when the sample size is small (Student, 1908) or a normal (Gaussian) distribution when the sample size is larger.

The two sample statistics that must be collected when using a normal distribution to prescribe a null distribution are the sample mean, m, and the sample variance, s^2:

$$f(y) = \frac{1}{\sqrt{2\pi s^2}} \exp \frac{-(y-m)^2}{2s^2} \tag{3.1}$$

Fig. 3.1 depicts the use of a normal distribution to specify a null distribution. The shaded regions of the distribution's tails depict the regions where a test statistic would be rejected for exceeding a commonly used level, $\alpha = 0.05$. We use y as the independent variable because, henceforth, we will be discussing null distributions in the context of time series analysis.

3.3.2 Synthetic-Data Time Series

In order to illustrate how autocorrelation and measurement error affect hypothesis tests, we generate synthetic-data time series. This approach allows us to create data with known properties that we can systematically alter in order to illustrate the effects of autocorrelation and measurement error.

To simplify the discussion, all of our time series are comprised of values drawn from a parent

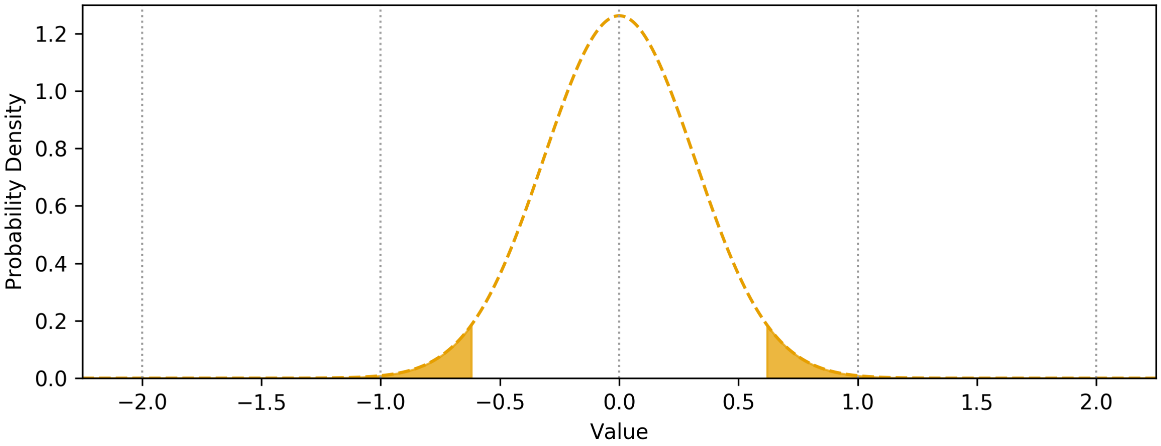

Figure 3.1: An example parametric probability distribution function, where the curve is specified by the Gaussian distribution. The shaded regions on each tail of the distribution indicate the regions where observing a test statistic would exceed the test level $\alpha = 0.05$.

distribution – in our case we use a normal distribution – that possesses parameters that we control. We specify that the parent distribution has a mean, $\mu = 0$, and variance, $\sigma^2 = 1$. We use these Greek letters, following Student (1908), in order to distinguish the *parameters* of the parent distribution – the population mean, μ, and population variance, σ^2 – from the *statistics* of the sample distribution – the sample mean, m, and the sample variance, s^2. Furthermore, the square roots of the variances denote the respective standard deviations: σ is the population standard deviation and s is the sample standard deviation. Box (1987) provides a historical discussion of Student's early scholarship which distinguished between these quantities.

The other aspect of the synthetic-data time series that we control is their autocorrelation structure. We arrange the order of the values in the time series to ensure that the time series possess a specific lag-1 autocorrelation, following the method described by Wilks (2011). Arranging the order of the values in this manner does not affect the population variance but, as we shall see, it does affect the sample variance.

We illustrate these elements using Fig. 3.2 to depict the all of the concepts that are involved and how they relate to each other. Panel A depicts the parent distribution which, again, is a parametric normal distribution specified by the parameters $\mu = 0$ and $\sigma = 1$. Throughout this paper we always depict parametric distributions using dashed lines. Panel B is a histogram depicting the relative frequency of 10,000 values, or observations, drawn from the parametric distribution. We use these observations to construct our time series. Since we drew such a large number of observations from the parent distribution, the shape of the histogram in Panel B roughly matches the parametric parent distribution in Panel A. Panel C depicts a time series constructed from the observations in Panel B. Thus, this time series is comprised of 10,000 observations but we only show the first 100 observations in order to make the autocorrelation structure of the time series more apparent. Panel D shows the same time series as in Panel C but with sky blue horizontal bars overlaid. These horizontal bars represent the mean value of samples taken from the observations, where ten successive observations are averaged into a single value. Panel E shows the distribution of the 1000 sample means taken from the time series. This distribution is known as the sample distribution of the sample mean. Panel F shows same the parametric null distribution depicted in Fig. 3.1 (except with the axes transposed) when $m = 0$ and s is estimated using the formula for the standard error of the mean:

$$s = \sigma/\sqrt{N}. \tag{3.2}$$

We highlight the discrepancy between Panels E and F. Typically when analysts use a parametric distribution to estimate the shape of the null distribution, as in Panel F, they are attempting to approximate the shape of the distribution that would be observed if a large number of samples were taken from data or observations which are consistent with the null hypothesis. In our synthetic data example, we depict such a distribution in Panel E. Panels E and F do not match because the technique we used for estimating the sample standard deviation in Eq. 3.2 assumes that the observations are independent of one another. In this time series (and in most time series) the observations are autocorrelated.

3.3.3 Complications

We use this visual technique depicted in Fig. 3.2 to highlight the effects of complications and to demonstrate the effectiveness of methods that account for them.

Autocorrelation

Fig. 3.3 depicts the same concepts as Fig. 3.2 except the dashed lines depicting parametric distributions are overlaid directly atop the sample distributions. We alter the lag-1 autocorrelation of the time series so that it increases with each row. Since there is no autocorrelation present in the top row, we see that specifying s using Eq. 3.2 actually results in a parametric distribution

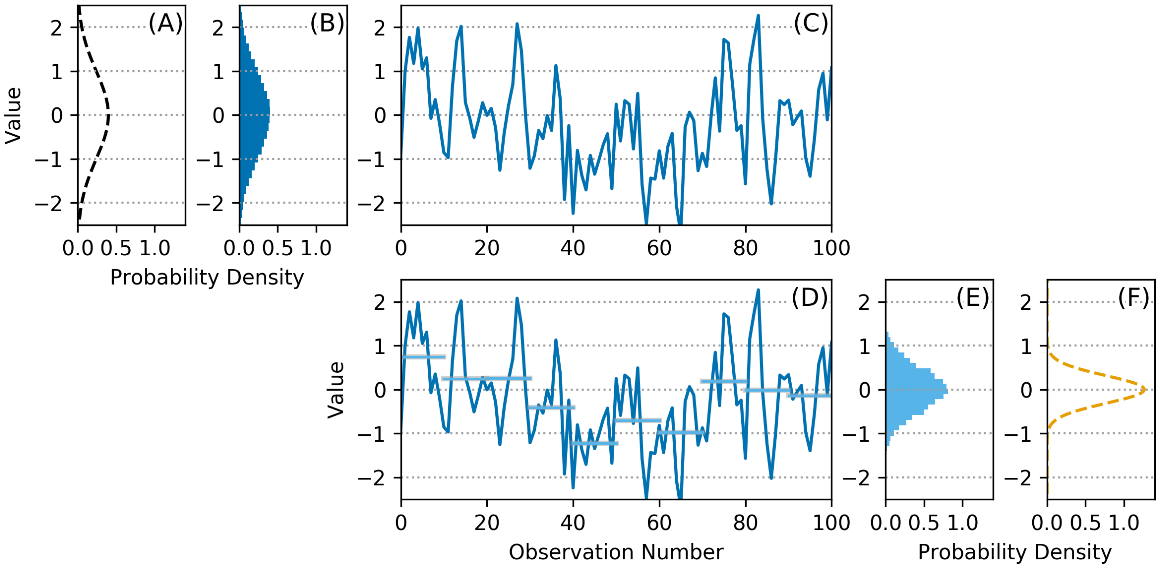

Figure 3.2: The elements of synthetic data times series and samples taken from it. A) A parametric probability distribution (dashed black line), representing the parent distribution, from which the values in the time series are drawn with $\mu = 0$ and $\sigma = 1$. B) A histogram (solid blue fill) of 10,000 values drawn from the parent distribution. C) A time series (solid blue line) constructed from the values in (B). Only the first 100 values are shown although the time series consists of all 10,000 values from (B). D) Sample means (horizontal sky blue lines) sampled from the time series, with the averaging period N=10. The first 10 sample means are depicted but 1000 samples, spanning the entirety of the time series are collected. E) A histogram of the 1000 sample means (sky blue fill) drawn from the time series. This distribution is known as the sample distribution of the sample mean. F) A parametric distribution (dashed orange line) meant to approximate the shape of the sample distribution of the sample mean where $s = \sigma/\sqrt{N}$. This parametric distribution does not match the shape of the sample distribution in (E) because the time series exhibits autocorrelation.

that matches the sample distribution of the sample mean. As the autocorrelation increases, using Eq. 3.2 to specify s in the parametric distribution results in an increasingly worse fit to the sample distribution of the sample mean.

This complication is well-understood within the context of time series analysis. A straightforward technique for accounting for autocorrelation is to inflate the sample variance by multiplying it by a factor, V, that estimates the magnitude of the lagged autocorrelation coefficients within a sample:

$$s_{auto}^2 = Vs^2 = V\frac{\sigma^2}{N} \tag{3.3}$$

where V is computed using the approach of Bayley and Hammersley (1946):

$$V = 1 + 2\sum_{j=1}^{N-1}\Big(1 - \frac{j}{N}\Big)\rho_j \tag{3.4}$$

where N is the number of observations in a sample and ρ_j is the jth lag autocorrelation coefficient. This approach works for the time series exhibiting lag-1 autocorrelation that we consider here and also for time series exhibiting autocorrelation beyond lag-1. We apply Eq. 3.3 and Eq. 3.4 and see, in the bottom three rows of Fig. 3.3, that the parametric distribution matches the sample distribution as the autocorrelation increases in the time series.

Measurement Error

One of the other assumptions of standard techniques for hypothesis testing is that the data being analyzed are either measured without error or the errors are small enough to be ignored. Climate data have many possible sources of error. Temporally or spatially averaged data have an uncertainty that is typically proportional to the variance of the data being averaged (Matalas and Langbein 1962, or, for a discussion of the data used in this study, Good et al. 2013). Even deterministic weather or climate models have uncertainty, since truncation errors in initial states cause uncertainty in model ensembles (Lorenz, 1963).

One method of accounting for this uncertainty is to take random draws from the error distribution and add them to the data. This method is used, for example, to estimate the initial system state in ensemble forecasts (Leith, 1974 & Anderson, 1996). While this approach can cause an individual sample to be closer to the mean of the parent distribution, it acts to increase the variance of the

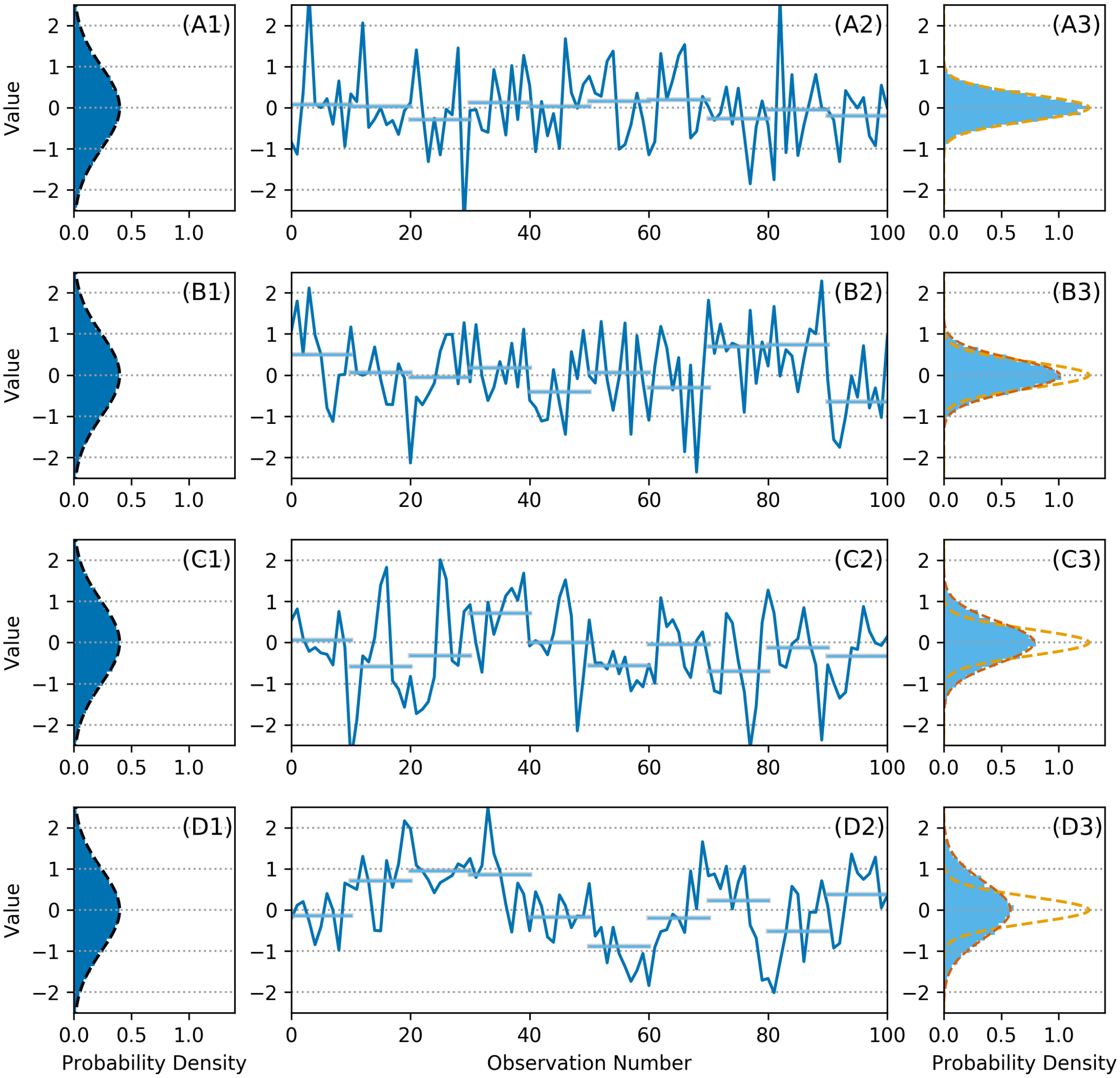

Figure 3.3: Each row contains a condensed version of the elements depicted in Fig. 3.2. In the left column the parametric parent distribution (dashed black line) is overlaid atop the histogram of values drawn from it (solid blue fill). In the middle column, the first 100 values of time series (solid blue lines) constructed from the histograms in the left columns are depicted along with the first 10 sample means (horizontal sky blue lines) sampled from each of the time series. Each of these sets of time series and samples consists of 10,000 observations and 1,000 sample means even though not all of these are shown. The right column shows the histogram of sample means drawn from each time series (solid sky blue fill) and parametric distributions used to estimate the shape of the sample distribution where the variance of the distribution is specified assuming $s^2 = \sigma^2/N$ (dashed orange curve) and $s^2 = V\sigma^2/N$ (dashed vermilion curve). The lag-1 autocorrelation of the time series is different for each row where in A it equals 0.0, in B it equals 0.25, in C it equals 0.5 and in D it equals 0.75.

sample distribution when many samples are taken.

To account for the effects of measurement error, we add the error variance, s_ϵ^2, to the autocorrelation-inflated variance:

$$s_{auto+error}^2 = V\sigma^2 + s_\epsilon^2 \tag{3.5}$$

This approach tacitly assumes that the measurement errors are uncorrelated. It is often the case that the errors themselves are indeed correlated which would increase the sample variance even further. However, in the absence of knowledge of the temporal structure of the errors, our assumption that the errors are independent provides a lower bound of their effect on the sample variance.

Fig. 3.4 depicts a time series with both autocorrelation and error and shows that the parametric distribution specified using using Eq. 3.5 accounts for both complications and matches the sample distribution. Fig. 3.5 depicts all three parametric distributions from Fig. 3.4C in order to highlight the importance of accounting for both autocorrelation and error. Applying the thresholds estimated from the parametric distribution that does not account for autocorrelation and error (narrowest distribution; orange dashed line) for a test at the $\alpha = 0.05$ level to test statistics collected from our time series that exhibits both autocorrelation and measurement error is equivalent to applying the $\alpha = 0.3$ level on the parametric distribution that accounts for both complications (widest distribution; bluish-green dashed line). In other words, by failing to account for autocorrelation and error an analyst would overestimate the frequency of statistically significant test statistics drawn from the time series in Fig. 3.4B estimated at the $\alpha = 0.05$ level by a factor of six.

3.3.4 Temperature and Salinity Data

We move beyond the consideration of individual hypothesis tests to a broader question in climate analysis. How does an analyst determine whether changes or trends observed in a global field of time series is significant? This problem is a difficult one, since it is often the case that when analyzing a global set of time series, only a subset of local time series will be observed to have statistically significant changes. In order to address this problem we use an observational data set of ocean temperature and salinity, the Hadley Centre EN 4.2.1 data set (Good et al., 2013), which provides quality controlled objective analyses of temperature and salinity data with uncertainty estimates. The temperature and salinity fields are spatially correlated and have non-negligible uncertainties, as shown in Figs. 3.6 and 3.7. Examining time series at individual points also demonstrates that the

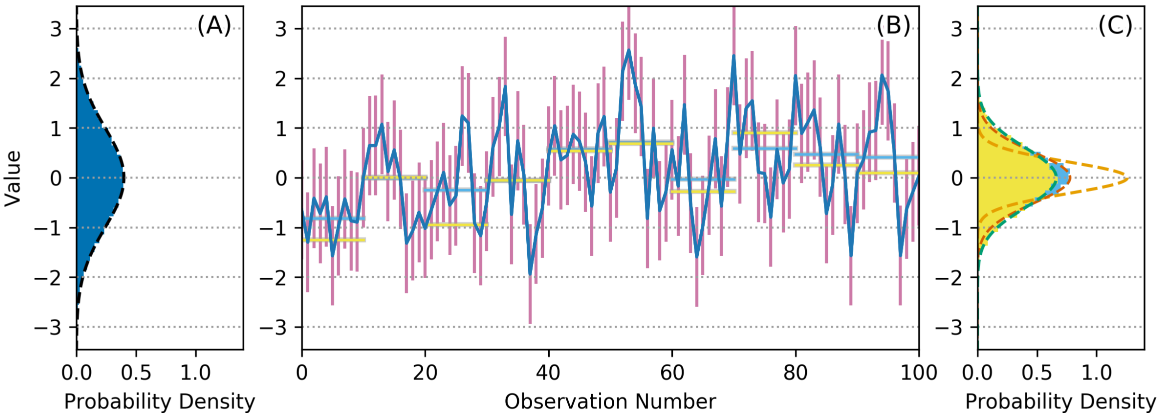

Figure 3.4: A time series with measurement error and its effect on the sample distribution. A) parent distribution (dashed black line) overlaid atop the histogram of values drawn from it (solid blue fill). B) The first 100 values of the time series (solid blue lines) constructed from the histograms in the left columns, depicted along with the first 10 sample means (horizontal sky blue lines) sampled from the time series. The magnitude of measurement error is depicted using vertical lines extending from each observation (solid reddish-purple lines). A random draw from the error distribution is collected for each observation and a second set of sample means (horizontal yellow lines) are sampled to account for the effect of measurement error. Each of these sets of time series and samples consists of 10,000 observations and 1,000 sample means even though not all of these are shown. C) The histogram of sample means drawn from the time series (solid sky blue fill) and the histogram of sample means drawn from the time series after random errors have been added to each observation (solid yellow fill). Dashed curves depict parametric distributions used to estimate the shape of the sample distribution where the variance of the distribution is specified assuming $s^2 = \sigma^2/N$ (dashed orange curve), $s^2 = V\sigma^2/N$ (dashed vermilion curve), and $s^2 = V\sigma^2/N + s_\epsilon^2$ (dashed bluish-green curve).

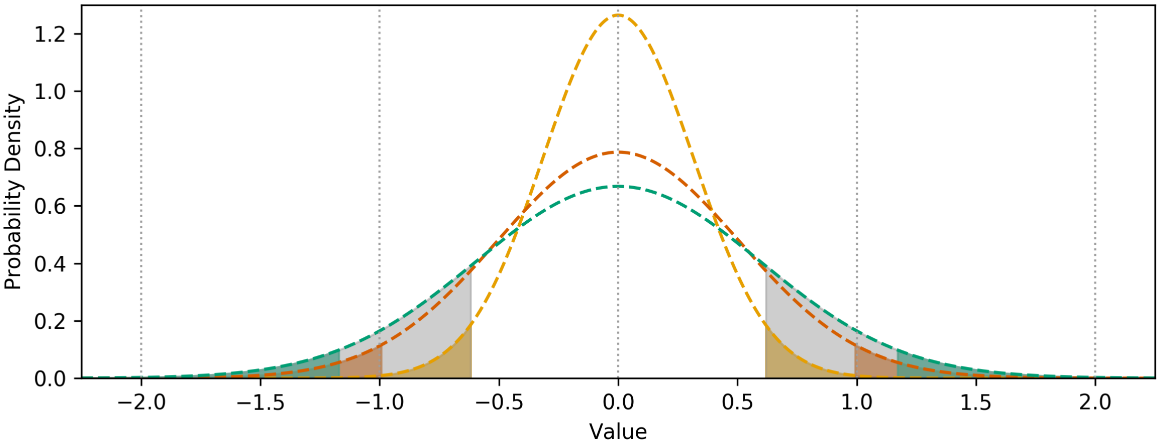

Figure 3.5: Three parametric distributions from Fig. 3.4C where the variance of each distribution is estimated using $s^2 = \sigma^2/N$ (dashed orange curve), $s^2 = V\sigma^2/N$ (accounting for autocorrelation; dashed vermilion curve), $s^2 = V\sigma^2/N + s_\epsilon^2$ (accounting for autocorrelation and measurement error dashed bluish-green curve). The filled regions beneath each dashed curve correspond to the regions that an observed test statistic would be rejected at the $\alpha = 0.05$ level. Incorrectly applying the threshold for the orange distribution for data represented by the bluish-green distribution results in an effective level of $\alpha = 0.3$.

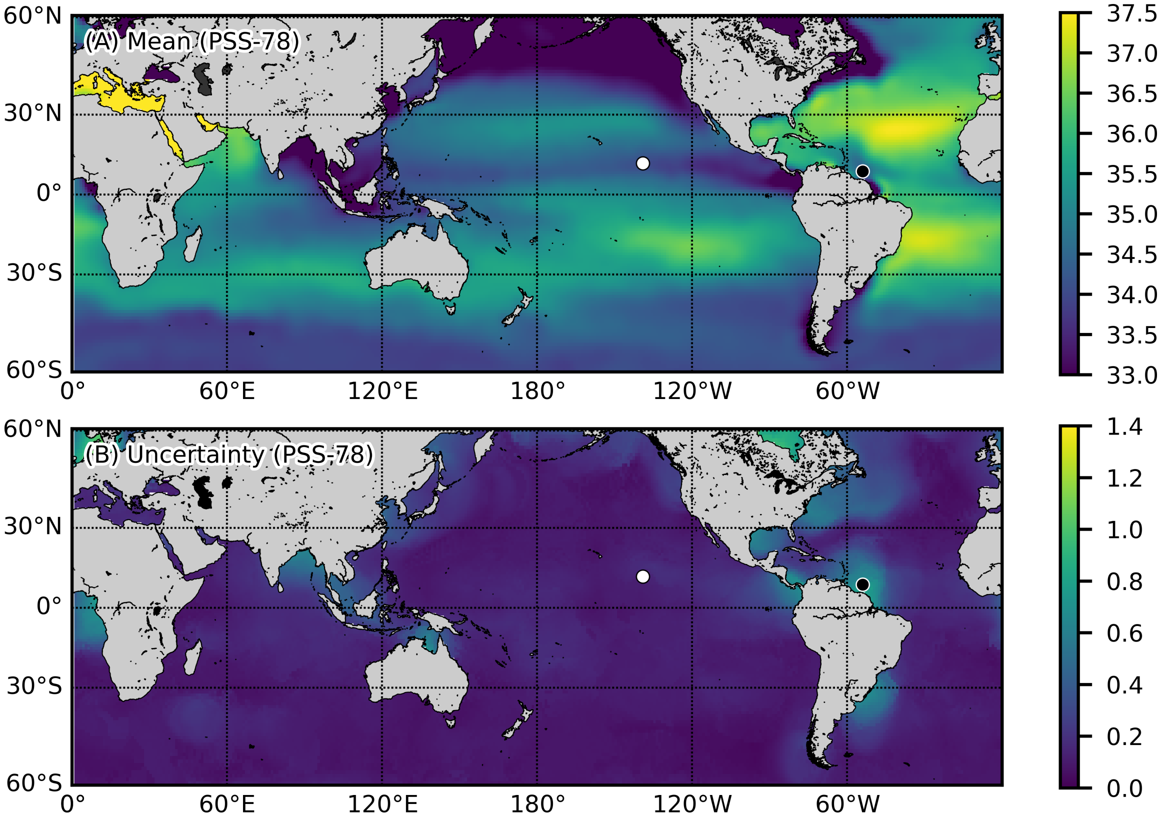

Figure 3.6: The mean SLS field and the mean uncertainty of the Hadley EN4.2.1 dataset. The black and white dots in each panel correspond to regions of high and low interannual variability of SLS, respectively. Time series taken from these points are shown in Fig. 3.8.

magnitude of the uncertainty is comparable to the interannual variability of the time series for both temperature and salinity (Figs. 3.8 and 3.9).

3.3.5 Multiple Testing (Field Significance)

With this data set we can begin to discuss the problem of multiple testing. If an analyst were to evaluate multiple hypothesis tests simultaneously while using the same test level, commonly $\alpha = 0.05$, for all of the tests, the probability of rejecting a null hypothesis increases as the number of tests increases. Thus, how does an analyst determine whether a global field of changes or trends is statistically significant?

Benjamini and Hochberg (1995) describe a technique for multiple testing which involves controlling the “false discovery rate” – in other words, minimizing the rate that a true null hypothesis is erroneously rejected. Their approach involves sorting the collection of p-values for the G grid points,

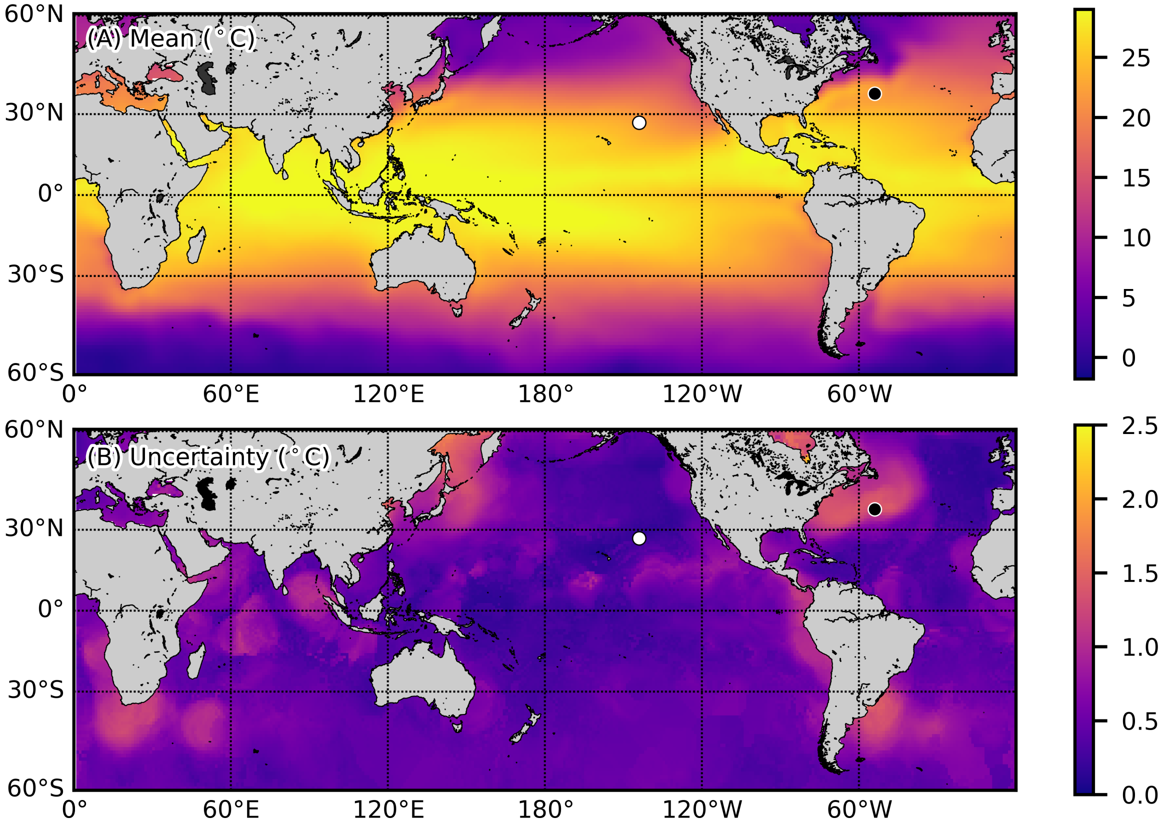
(A) Mean (°C)
(B) Uncertainty (°C)
60°N
30°N
0°
30°S
60°S
0°
60°E
120°E
180°
120°W
60°W
25
20
15
10
5
0
2.5
2.0
1.5
1.0
0.5
0.0

Figure 3.7: The mean SST field and the mean uncertainty of the Hadley EN4.2.1 dataset. The black and white dots in each panel correspond to regions of high and low interannual variability of SST, respectively. Time series taken from these points are shown in Fig. 3.9.

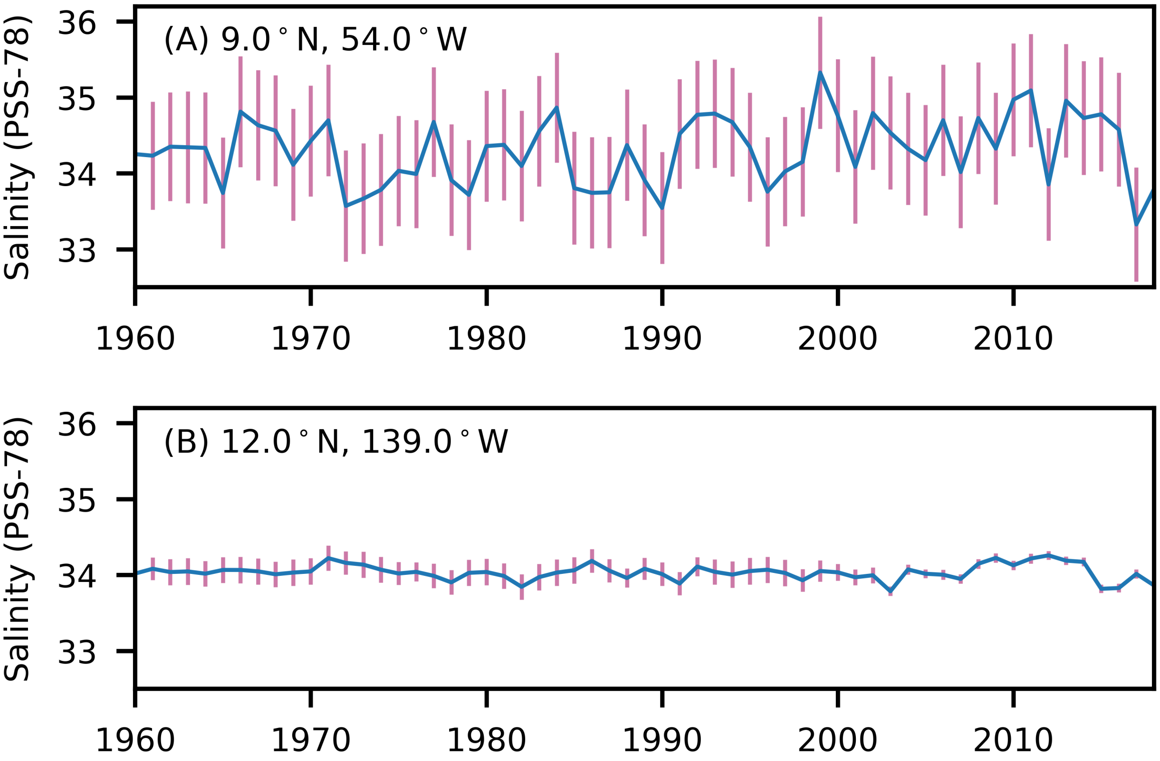

Figure 3.8: Time series of annual mean SLS values (solid blue line) and measurement error (solid reddish-purple lines) from two different points in the Hadley EN4.2.1 dataset. A) Region of high interannual variability in SLS. B) Region of low interannual variability in SLS. In both cases the magnitude of error is comparable to the magnitude of interannual variability.

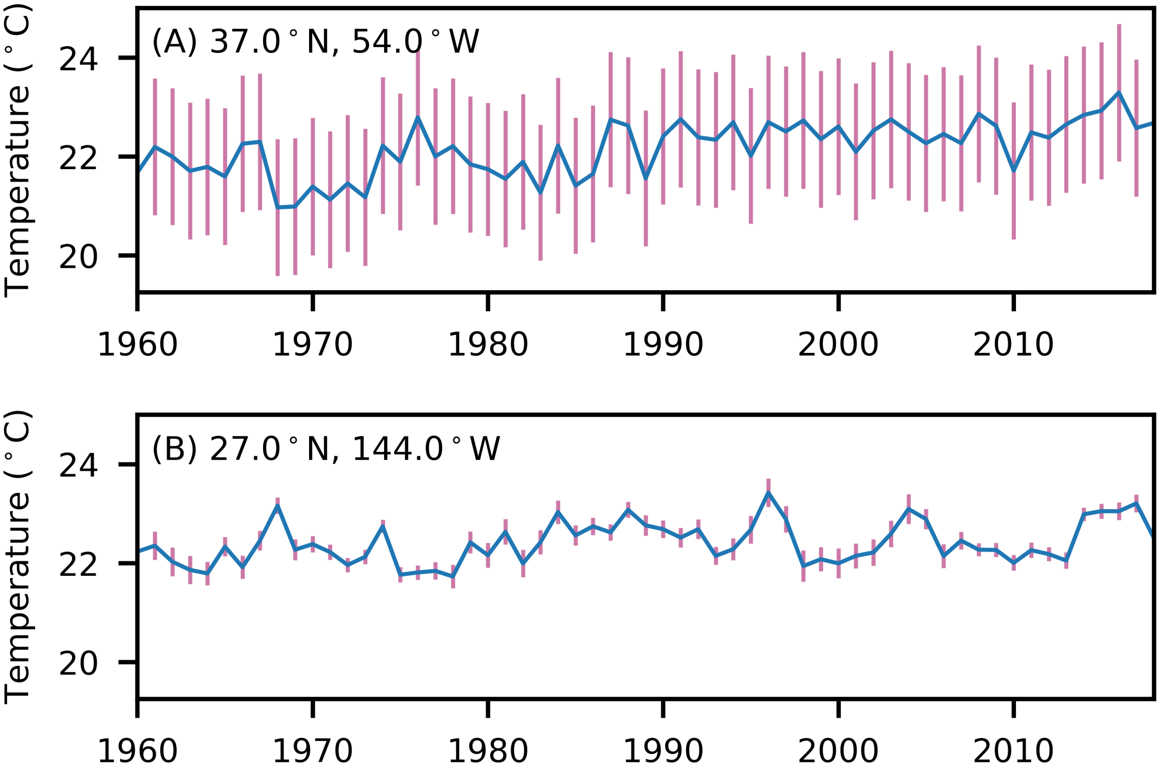

Figure 3.9: Time series of annual mean SST values (solid blue line) and measurement error (solid reddish-purple lines) from two different points in the Hadley EN4.2.1 dataset. A) Region of high interannual variability in SST. B) Region of low interannual variability in SST. As with SLS, in both cases the magnitude of error is comparable to the magnitude of interannual variability.

p_i for $i, ..., G$, into ascending order, and then scaling the level, p^*_{FDR}, for which a given p-value is deemed to be significant as a function of the number of tests that are conducted. In the context of climate analysis, Ventura et al. (2004) and Wilks (2016), have adapted this technique and have demonstrated that it is applicable to climate data even if such data is spatially, as well as temporally, correlated. Local hypotheses should be rejected if their p-values are less than or equal to the false discovery threshold:

$$p^*_{FDR} = \max_{i=1,\ldots,G} [p_{(i)} : p_{(i)} \leq (i/G)\alpha_{FDR}] \tag{3.6}$$

where α_{FDR} is the level of the test. Wilks (2016) recommends choosing a value of α_{FDR} that is twice the desired global level, α_{global}. If an analyst intends to evaluate a global test at $\alpha_{global} = 0.05$ then $\alpha_{FDR} = 0.1$.

3.3.6 Model Misspecification

One of the most widely used techniques to infer trends in climate data is to apply a linear regression to a time series and to use the slope of the best-fit line to determine the magnitude of a trend. This procedure involves assuming that a linear model of the form:

$$y_k = \alpha + \beta t_k + e_k \tag{3.7}$$

where α and β are offset and slope, respectively, and e_k is a random innovation, can adequately relate a given observation, y_k, to the time of an observation, t_k (Draper and Smith, 1998). Many analyses tend to use standard formulae to determine that β is significantly different from zero and thus can be used to estimate a trend in the data.

The question that is rarely asked, however, is whether a linear model is an appropriate one for a given time series. The regression literature is replete with warnings that the analyst must determine whether there is significant lack of fit between the model and the observations. Such analysis involves viewing the residuals to determine whether they exhibit heteroskedasticity (non-constant variance), autocorrelation, or a pattern that suggests additional terms are missing from the regression analysis (see, for example, Fig 2.6 of Draper and Smith, 1998). If such problems are present, then the estimate of the variance of β will be biased and we cannot use the standard formulae to conclude whether β is significantly different from zero.

Even when a linear model is appropriate for the data, the error of the regression slope is more complex than the error of the mean (Eq. 3.2) because the regression slope and offset are correlated. One could imagine adding or removing data from the time series and then recomputing the linear regression would change both the slope and the offset and that these changes would covary. Both the error of the slope and the error of the offset depend on the estimated standard deviation of the uncorrelated residuals (Wilks, 2011):

$$s_e = \sqrt{\frac{1}{n-2}\left(\sum_{i=1}^{n} y_i^2 - n\bar{y}^2 - \beta^2\left[\sum_{i=1}^{n} x_i^2 - n\bar{x}^2\right]\right)}. \tag{3.8}$$

Eq. 3.8 becomes biased if the residuals are correlated. The error of the offset, σ_α, is:

$$\sigma_\alpha = s_e\left[\frac{\sum_{i=1}^{n} x_i^2}{n\sum_{i=1}^{n}\left(x_i-\bar{x}\right)^2}\right]^{1/2}, \tag{3.9}$$

and the error of the slope, σ_β, is:

$$\sigma_\beta = \frac{s_e}{\left[\sum_{i=1}^{n}\left(x_i-\bar{x}\right)^2\right]^{1/2}}. \tag{3.10}$$

It takes considerable time to individually examine the residuals for a global field in which each grid point represents a time series. Fortunately, there are many statistical tests which examine either the structure of data to determine whether autocorrelation is present (Durbin and Watson 1950, Durbin and Watson 1951), whether the residuals exhibit heteroskedasticity (Breusch and Pagan, 1979), or whether the linear model is a poor fit for the time series (Ramsey 1969, Harvey and Collier 1977). We apply one such test, the Harvey-Collier test for model misspecification, to demonstrate the utility of applying such tests to global fields of time series. Such tests quickly show the analyst whether a given model formulation is appropriate for modeling a time series. In the case of the Harvey-Collier test, the linear regression residuals are estimated recursively and examined to see whether or not the mean of the residuals is zero. The null hypothesis is that a linear model is appropriate for the data and the test returns a p-value. Low p-values suggest that a linear model is inappropriate for a given time series.

As we can see in Fig. 3.10A the linear model is a poor fit to the SLS time series over most of the ocean, with the exception of regions affected by river runoff. Fig. 3.10B shows that SST time

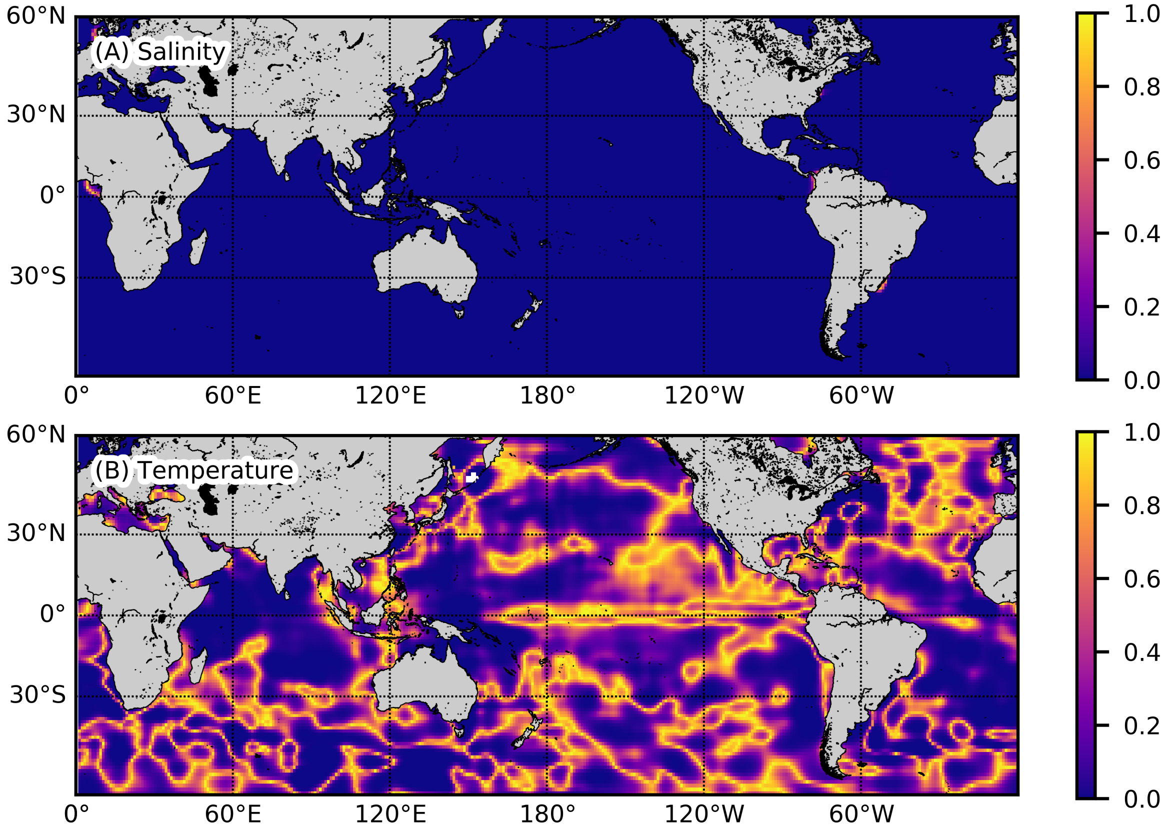

Figure 3.10: Results of applying the Harvey-Collier model misspecification test (p-values, shaded) to annual means of salinity and temperature in the Hadley EN4.2.1 data set.

series can plausibly be fit to a linear model over certain regions of the ocean. However, the pattern is complex and deserving of investigation in its own right. For both SLS and SST, it is inadvisable to use linear models to characterize the time series indiscriminately over the global ocean because large regions of the ocean have time series that cannot appropriately be modeled as linear.

3.4 An Example Test for Difference of Means

We apply the techniques we have described to account for three of the complications present in the data – autocorrelation, measurement error and multiple testing – in order to reexamine whether studies which infer statistically significant changes in the ocean's salinity field reach valid conclusions.

We use the same statistical test and compute the same test statistic as a previous study, Hosoda et al. (2009), which uses a test for differences of mean to demonstrate that ocean salinity has changed significantly over the past several decades. Their test is slightly more complicated than the basic tests for difference of means, because theirs allows for the variance of each sample to be different. We see that since the magnitude of the measurement error is non-stationary (Fig. 3.8) we would, indeed, expect the variance of each sample to be different. In this methodology, the test statistic, t, is compared against a t distribution to determine how improbable the observed difference of mean is, where:

$$t \equiv \frac{m_x - m_y}{\sqrt{s_x^2/n_x + s_y^2/n_y}}. \tag{3.11}$$

where m_x and m_y are the mean values of each sample, and n_x and n_y are the size of each sample.

We'll note here a subtlety in the analysis: when analyzing our synthetic data we know the population variance, σ^2, because we specified it when creating the data. When analyzing an observational data set we don't actually know the population variance, but the sample variance s^2 for independent data converges to Eq. 3.2 when the number of samples is large because of the central limit theorem. When the number of samples is small, the t distribution is used instead of assuming that the sample statistics will be normally distributed.

Using the t distribution, unlike the normal distribution, requires estimating the number degrees of freedom, df, of the system. Since Hosoda et al. (2009) assume unequal variances, the degrees of freedom are not simply $df = n_x + n_y - 2$ but are estimated using the Behrens (1929)-Fisher (1935) approach, where:

$$df = \frac{(s_x^2/n_x + s_y^2/n_y)^2}{\frac{(s_x^2/n_x)^2}{n_x - 1} + \frac{(s_y^2/n_y)^2}{n_y - 1}}. \tag{3.12}$$

When we use the standard error in Eq. 3.2 to estimate the variance, we see statistically significant changes in salinity over large regions of the ocean, as depicted in Figs. 3.11A & 3.12A. After inflating the variance using Eq. 3.3 to account for autocorrelation, many of the regions of significant changes disappear (Figs. 3.11B & 3.12B). After including the effects of measurement error using Eq. 3.5, the regions of significance diminish further (Figs. 3.11C & 3.12C). Finally, after accounting for multiple testing using Eq. 3.6, all of the regions of significant changes vanish (Figs. 3.11D & 3.12D).

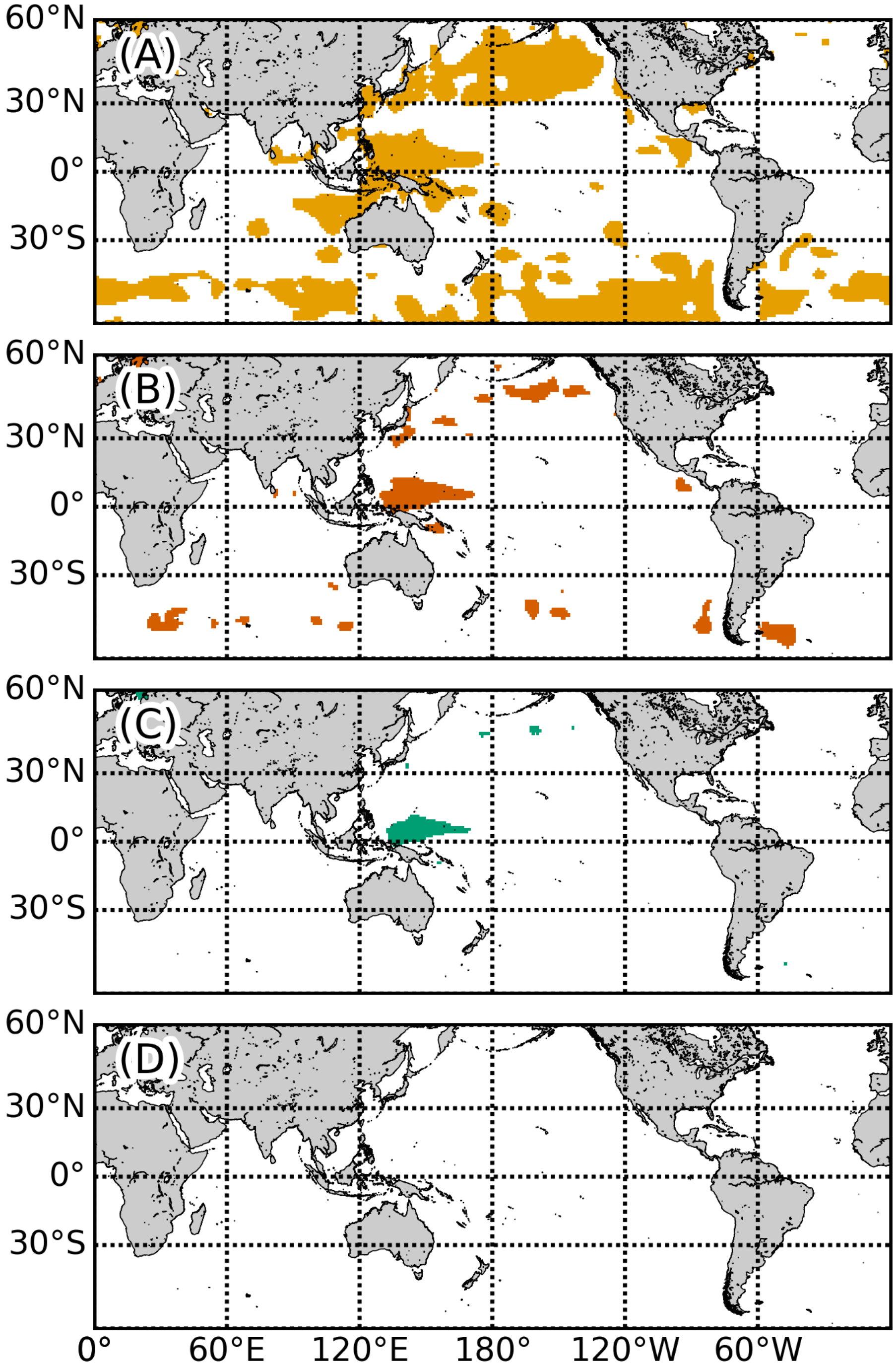

Figure 3.11: Regions of significant differences of observed SLS, following the methodology of Hosoda et al. (2009), evaluated at $\alpha = 0.05$. A) Shaded areas (solid orange fill) correspond to regions where a t-test infers significant change in SLS when $s^2 = \sigma^2/N$. B) Shaded areas (solid vermilion fill) correspond to regions where a t-test infers significant change in SLS when $s^2 = V\sigma^2/N$. C) Shaded areas (solid bluish-green fill) correspond to regions where a t-test infers significant change in SLS when $s^2 = \sigma^2/N + s_\epsilon^2$. D) The result of applying the FDR test to infer regions of significant change in SLS after accounting for autocorrelation and measurement error. No grid points are highlighted.

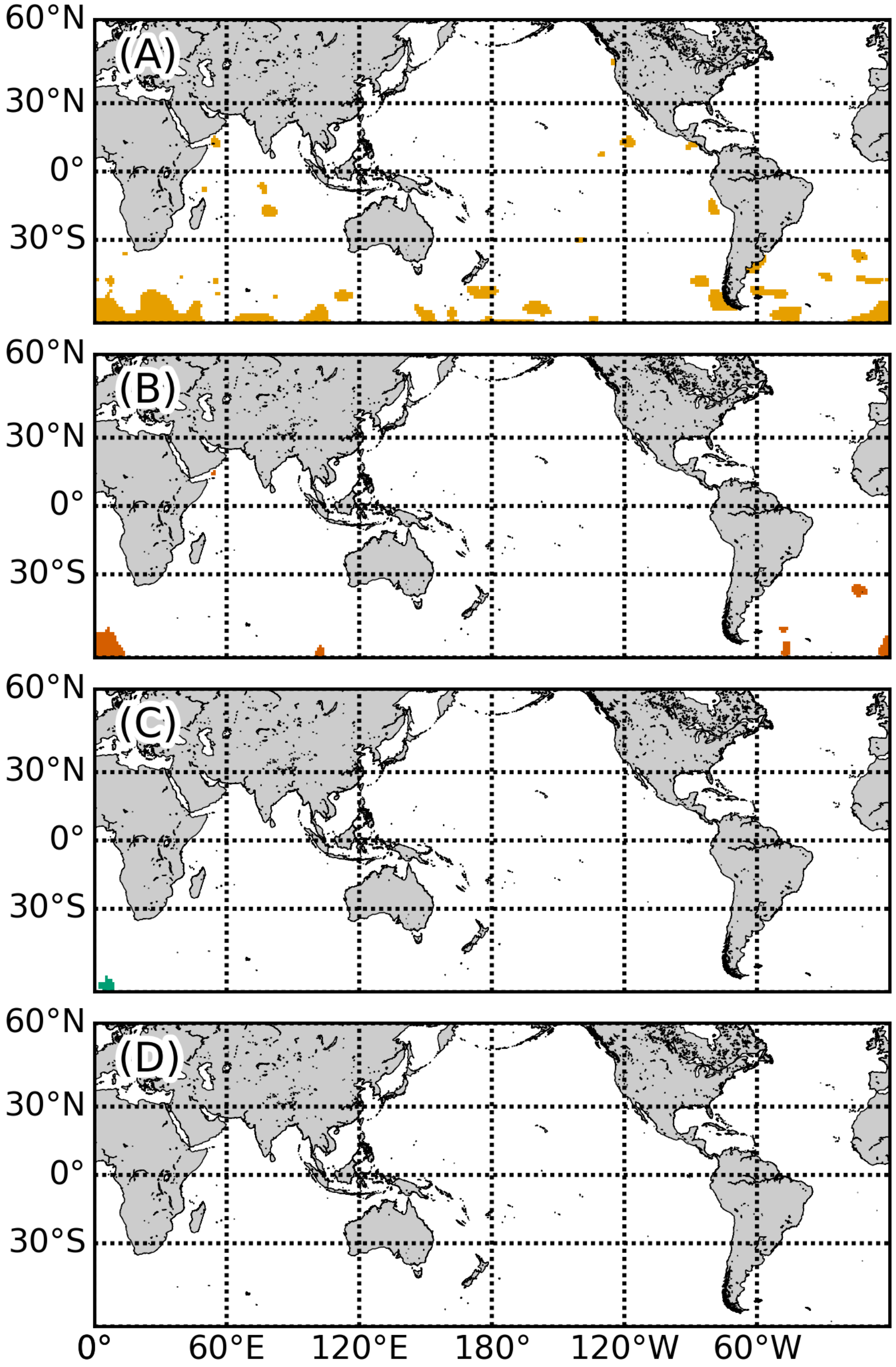

Figure 3.12: Regions of significant differences of observed SST, following the methodology of Hosoda et al. (2009), evaluated at $\alpha = 0.05$. A) Shaded areas (solid orange fill) correspond to regions where a t-test infers significant change in SST when $s^2 = \sigma^2/N$. B) Shaded areas (solid vermilion fill) correspond to regions where a t-test infers significant change in SST when $s^2 = V\sigma^2/N$. C) Shaded areas (solid bluish-green fill) correspond to regions where a t-test infers significant change in SST when $s^2 = \sigma^2/N + s_\epsilon^2$. D) The result of applying the FDR test to infer regions of significant change in SST after accounting for autocorrelation and measurement error. No grid points are highlighted.

3.5 Discussion

Many studies use statistical hypothesis tests to infer changes or trends in the ocean's SST and SLS fields. These studies use parametric distributions to estimate the shape of the null distribution without accounting for the effects of autocorrelation and measurement error. We attempt to demonstrate throughout this study that ignoring these effects causes an analyst to overestimate the significance of changes or trends observed in the data because these complications increase the variance of samples taken from the time series. Analysts often use levels such as $\alpha = 0.05$ to distinguish significant p-values from insignificant ones (Jolliffe, 2004). We follow this convention throughout our analysis, culminating in Figs. 3.11 and 3.12. This analysis shows that regions of significant changes for both the SLS and SST fields (when evaluated at $\alpha = 0.05$) vanish entirely.

This result for the SLS field contradicts most of the previously published literature on ocean salinity trends. We discuss the methodologies of six studies that analyze ocean salinity, all of which claim to observe statistically significant changes or trends in ocean salinity. None of these studies account for autocorrelation, measurement error and the effects of multiple tests. Many of them make additional assumptions that complicate the analysis, which we also discuss in brief.

- Boyer et al. (2005): In this analysis each observation is the mean of five years of data and the increment between successive observations is one year. For example, $t_1 = \overline{1955 - 1959}$, $t_2 = \overline{1956 - 1960}$, $t_3 = \overline{1957 - 1961}$, where the overline designates a temporal mean and so on. These observations are not merely autocorrelated – each observation significantly overlaps with the observations before and after it. Thus the estimated sample variance using the formula for the standard error of the mean is much smaller than the actual sample variance and the magnitude of N is significantly overestimated. Furthermore, the fact that this study uses Eq. 3.2, the formula for the standard error of the mean, is also a misapplication because the test statistic they consider is actually the slope of a linear regression, thus they should be using Eq. 3.10 to estimate the error. Linear regressions are employed without checking for lack of fit. Lastly, the variance is not estimated for each grid point, one variance is computed and applied over most of the ocean and a second is computed for the Arctic.
- Hosoda et al. (2009): In this analysis a test for difference of mean is conducted upon interpolated data without accounting for the effects of autocorrelation, measurement error and multiple testing. We repeat the analysis of this paper (Figs. 3.11 & 3.12) and find that the

regions of significant changes in salinity (and temperature) vanish after accounting for these complications.

- Durack and Wijffels (2010): In this analysis a twenty-two term multiple linear regression is employed. One of these terms (C_1 in their Eq. 1) is used to estimate the significance of trends. The sample distribution of this coefficient should be computed as a joint distribution of all twenty-two regression terms. The regression is not checked for lack of fit. The significance estimates also do not appear to account for autocorrelation and multiple testing.

- Helm et al. (2010): In this analysis 90% confidence intervals are reported without stating how these intervals are estimated. These intervals do not appear to have been estimated while taking autocorrelation into account. Additionally, the regions of significance do not appear to account for multiple testing.

- Skliris et al. (2014): In this analysis linear regressions are employed to estimate trends. These regressions are not checked for lack of fit. The significance of these trend estimates and the error bars depicted in the figures do not take autocorrelation into account. Moreover, the salinity anomalies exhibit a high amount of autocorrelation (their Fig. 2B). Regions of statistically significant salinity changes are estimated without accounting for multiple testing.

- Tesdal et al. (2018): In this analysis linear regressions are employed to estimate trends. The regressions are not checked for lack of fit. Student's t-test is used to estimate the significance of these trends without accounting for autocorrelation and interpolation error (the study uses interpolated data from Argo profiles). Multiple testing is not taken into account.

We see common patterns in each of these studies. All of these studies claim to observe statistically significant changes or trends in ocean salinity yet none account for autocorrelation and multiple testing. Some mention attempts to account for error but do not state how these errors are accounted for analytically.

Since there are a large number of studies which all claim to observe significant changes in the ocean's salinity field, much effort has been focused on pursuing this line of research. However, when accounting for the complications present in climate data – autocorrelation, measurement error and multiple testing – we see that the observed changes in ocean salinity described in these studies is

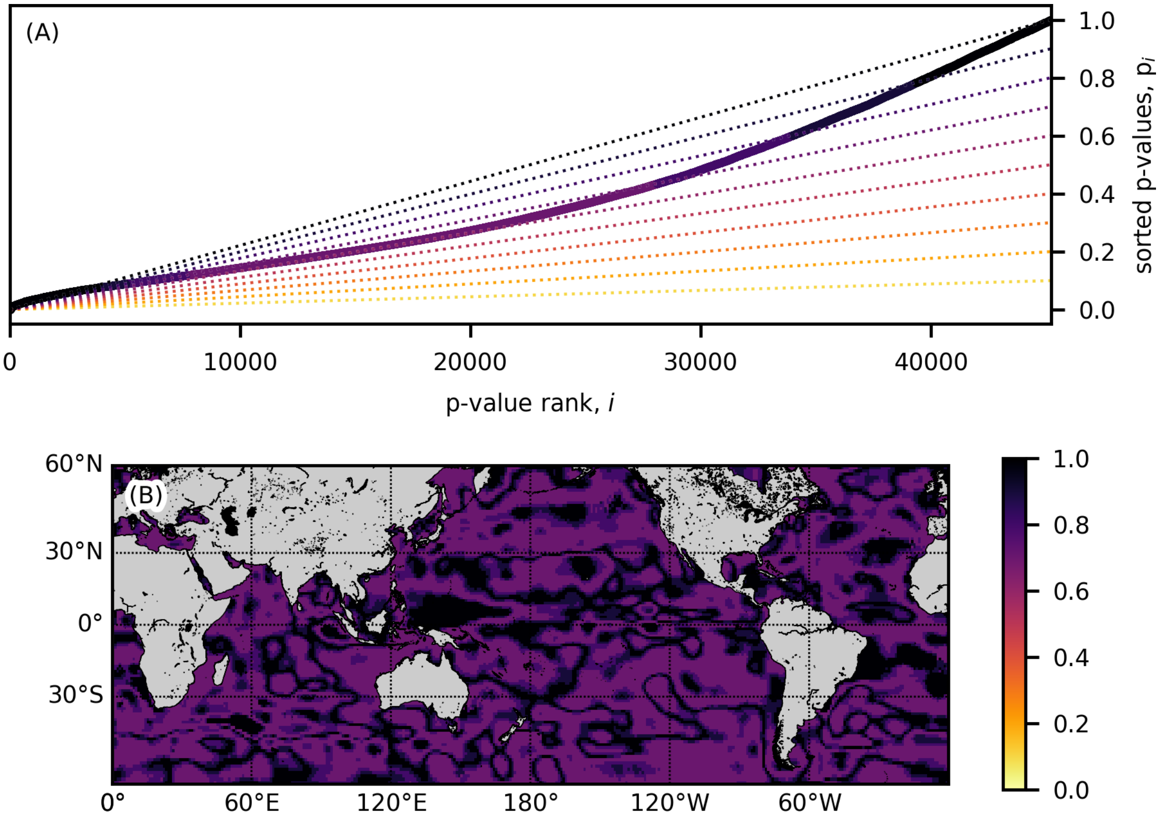

Figure 3.13: A) Sorted p_i values from the difference of mean test on SLS data, as depicted in Fig. 3.11 (shaded curve). Dotted lines indicate various FDR thresholds where α_{FDR}= 0.1, 0.2, ... 1.0. B) A map of the corresponding α_{FDR} thresholds that each grid point falls below.

the result of overestimation of statistical significance. This suggests that the broader conclusions of these studies should be reevaluated.

To place these results into a more rooted discussion of significance testing in the geosciences, we note that specifying any level, whether $\alpha = 0.01,\ 0.05,\ 0.1...$ to distinguish between significant and insignificant p-values is arbitrary. We provide a more inclusive description of changes in the SLS and SST fields, by using various α_{FDR} thresholds to evaluate the distribution of sorted p-values (Figs. 3.13 and 3.14). We see that grid points in the SST field exhibit changes corresponding to more stringent α_{FDR} levels over large regions, with the a mode threshold of $\alpha_{FDR} = 0.5$ (Table 3.1). While the SLS field also exhibits a few grid points whose sorted p-values fall below the $\alpha_{FDR} = 0.5$ threshold, the mode threshold of the SLS field is $\alpha_{FDR} = 0.7$.

A key insight from this analysis is that, by overlooking the complications described in this study, we as a community have been acclimated to believing that fluctuations in oceanographic time series

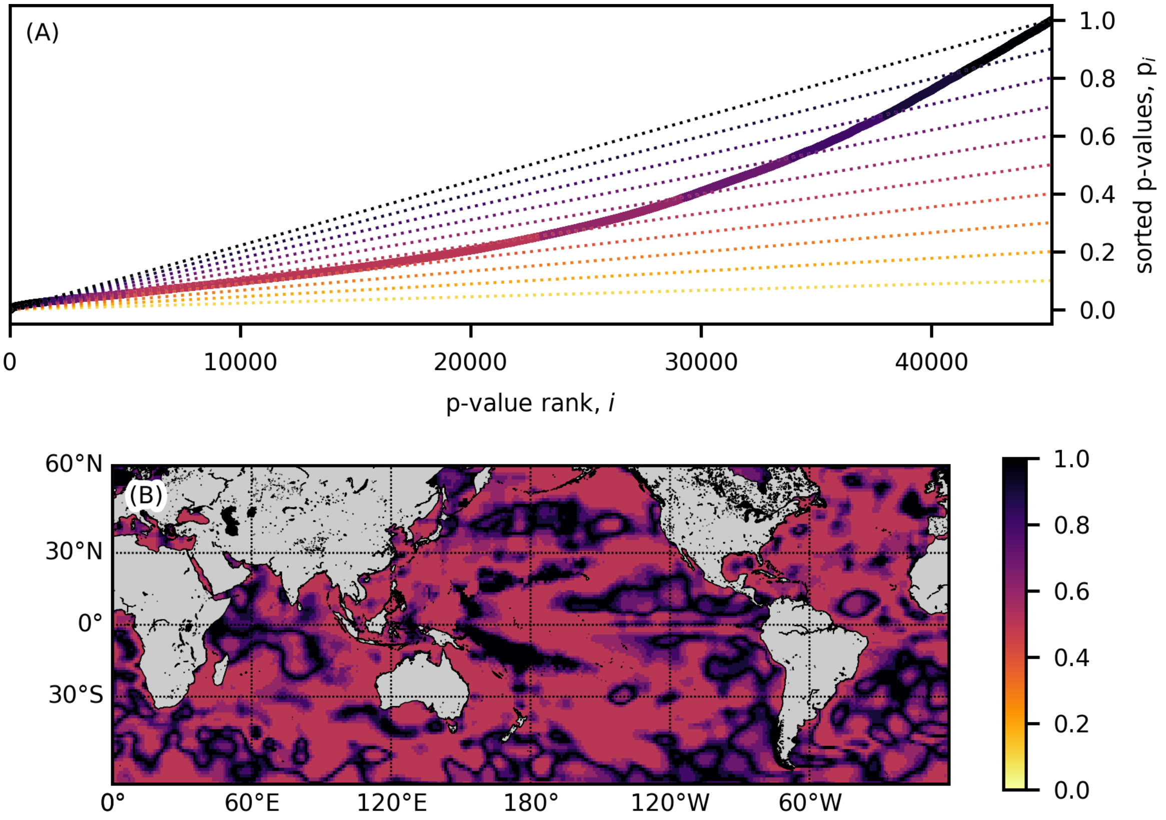

Figure 3.14: A) Sorted p_i values from the difference of mean test on SST data, as depicted in Fig. 3.12 (shaded curve). Dotted lines indicate various FDR thresholds where α_{FDR}= 0.1, 0.2, ... 1.0. B) A map of the corresponding α_{FDR} thresholds that each grid point falls below.

Table 3.1: False Discovery Rate levels (α_{FDR}), the corresponding level of the global test (α_{global}), and the number of grid points for surface salinity and temperature fields falling below each threshold.

α_{FDR}	α_{global}	*Number SLS*	*Number SST*
0.1	0.05	0	0
0.2	0.1	0	0
0.3	0.15	0	0
0.4	0.2	0	0
0.5	0.25	3	18159
0.6	0.3	8	8092
0.7	0.35	20499	5595
0.8	0.4	8475	4538
0.9	0.45	6598	3781
Above 0.9	Above 0.45	9633	5051

over the past few decades are indicative of observable changes in ocean climate evaluated at stringent significance levels. While the ocean's climate is indeed changing, we must reacclimate our collective intuition to recognize that observed changes in the ocean occur at less stringent levels of significance than currently believed.

We've devoted a large part of the narrative to describing the steps involved in hypothesis testing in part to emphasize what these tests actually accomplish – they determine the probability of observing a given test statistic, assuming the null hypothesis is true. These tests cannot, as is often assumed in many studies, determine whether a given hypothesis that intends to explain the cause of these variations is actually true. In the context of the studies we review, hypothesis tests can determine whether data compared between two epochs exhibit improbable differences in mean. This is a very limited insight. Meanwhile, many studies claim that statistical tests allow them to infer broader explanations about the climate system – for example, that changes in SLS are consistent with the notion that the hydrological cycle is changing.

Avoiding this type of reasoning – building ambitious explanations from such a humble statistical methodology – may require rethinking the role such tests play in research. Nicholls (2001) and Ambaum (2010) suggest they are more accurately conceptualized as "insignificance tests" and would better used as an initial step to determine whether variations in data are insignificant, thereby enabling the analyst to decide whether it is worth pursuing a particular course of research. Instead, analysts often do the opposite, conceiving of an explanation of a physical phenomenon and then using statistical tests after the fact to prove that this particular explanation is meaningful. Resisting this temptation is vital.

3.6 Chapter Acknowledgements

This work is indebted to the scholarship and pedagogical efforts of Daniel S. Wilks. I thank Eugenia Kalnay for her instruction in statistical methods and thank Douglas W. Nychka, Mohamad El Gharamti, Jeffrey L. Anderson and Timothy J. Hoar for their guidance and helpful discussions. B.K.J. was supported by NSF through its sponsorship of NCAR. Some of this analysis was carried out on Geyser, the visualization cluster that complimented the Yellowstone Supercomputing Resource (ark:/85065/d7wd3xhc), provided by CISL at NCAR, also sponsored by NSF. The colorblind-safe color palettes used throughout the figures in this study were developed by Wong (2011).

Chapter 4

Combining Water Mass Census and Transformation in θ-S Coordinates: an Illustration in the Southern Ocean

4.1 Abstract

One of the defining features of the Southern Ocean is the stark potential temperature-salinity contrast of its cold, fresh surface layer with the warm, salty water masses which lie beneath. These water masses are often studied using the water mass transformation framework, in which surface fluxes of freshwater and heat are used to compute the rate that one water mass is transformed into another. This transformation rate, as it is known, is nearly always computed as a function of density. However, density alone cannot be used to distinguish water masses because waters of different compositions can have the same density. We review prior studies and demonstrate how they conflate surface waters with subsurface water masses. To reconcile this problem, we use the Southern Ocean State Estimate to illustrate a pair of complimentary techniques for understanding water mass transformation: computing transformations as a function of potential temperature and salinity, rather than density, and comparing these transformations to a census of the Southern Ocean water masses. The inferences from this approach call conclusions from prior studies into question. We find that Circumpolar Deep Water is usually insulated from the sea surface and is thus not typically transformed by surface fluxes into upper and lower branches, as is commonly believed. We also demonstrate that Subantarctic Mode Water and Antarctic Intermediate Water are formed by density gain in the vicinity of the Subantarctic Front.

4.2 Introduction

Understanding the circulation of the Southern Ocean requires a methodology that properly reflects its intricacy. The Atlantic, Pacific, and Indian Basins are connected by the Antarctic Circumpolar Current (ACC) which flows across all longitudes and partitions the surface waters into distinct regimes (Deacon, 1937b). The regime south of the ACC is known as the subpolar regime – it is strongly influenced by its proximity to Antarctica (Orsi et al., 1995). Here precipitation exceeds evaporation and the ocean surface is seasonally covered by sea ice. These conditions impart a distinct cold, fresh potential temperature-salinity ($\theta - S$) signature into the surface mixed layer. This surface layer, which extends from the Polar Front (which we describe below) of the ACC to the Antarctic continental margins, is known as AASW (Mosby, 1934). Beneath AASW lies a warm, salty water mass known as Circumpolar Deep Water CDW (Deacon, 1937a, who established the circumpolar extent of this water mass but actually referred to it as the "Warm Deep Current") which is comprised of the respective deep waters of the Atlantic, Pacific and Indian Basins after they have been mixed within the ACC. Also in the vicinity of ACC are two other prominent water masses: SAMW (McCartney, 1977), which is a near-surface water mass identified by its low vertical stability, and AAIW (Wust, 1935), which exists beneath SAMW at a depth of roughly 800-1200m and is identified by its low salinity content. Since these water masses have complex structures (both spatially and in their $\theta - S$ composition) we review them in greater detail below.

The relationships between these water masses are often studied using a methodology known as the water mass transformation framework. This diagnostic framework uses estimates of surface fluxes of freshwater and heat to compute the rate at the which the density of surface water is transformed from one control volume into another. Walin developed the underlying concepts of transformation studies in two manuscripts which relate the surface flux of freshwater to the circulation of salinity (Walin, 1977) and the flux of heat to the circulation of temperature (Walin, 1982). This circulation is inferred by partitioning the ocean into control volumes in order to relate a given surface flux to the movement of seawater from one control volume to another. For example, dividing the ocean into two control volumes separated by an isohaline surface results in one control volume with a higher salinity than the other. A freshwater flux into the higher-salinity control volume will decrease its salinity, effectively moving some of the seawater contained within it across the isohaline surface to the lower-salinity control volume.

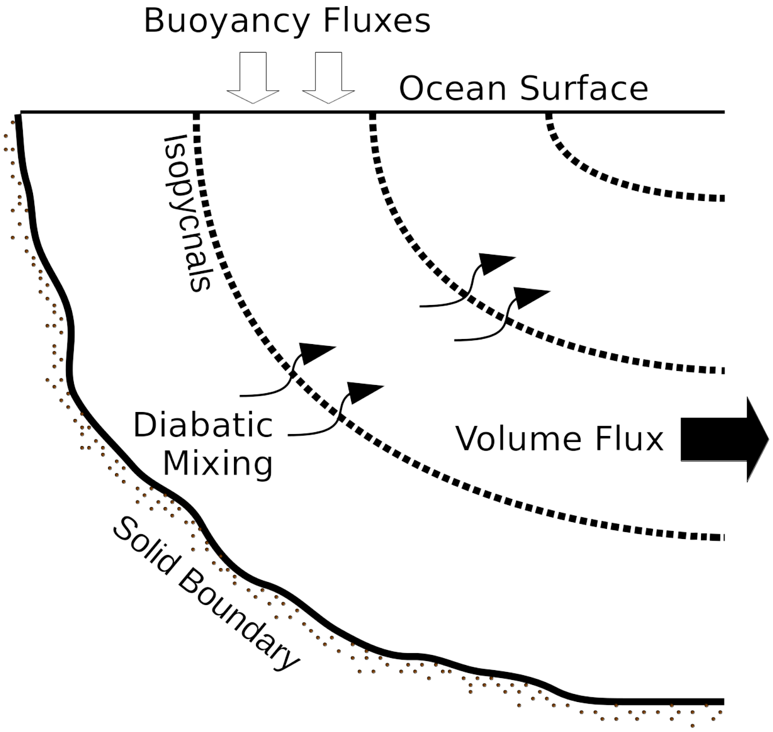

Figure 4.1: A depiction of the water mass transformation framework applied to the potential density field. Dotted lines represent isopycnal surfaces through which water can be transformed either by surface fluxes or subsurface diabatic mixing.

Later authors – Speer and Tziperman (1992), Marshall et al. (1999), Nurser et al. (1999), Sloyan and Rintoul (2001a) – developed a methodology, now known as the water mass transformation framework, by adapting Walin's technique to relate the simultaneous fluxes of both freshwater and heat to the circulation of density (Fig. 4.1). Within these studies surface fluxes are typically imposed (with a few exceptions) as a one-dimensional function of density, $T(\sigma_\theta)$, where $\sigma_\theta = (\rho - 1) \times 1000$ and ρ is potential density, and the fluxes transform water between control volumes, in this case known as density classes, which are separated by isopycnal surfaces.

Many studies apply these $T(\sigma_\theta)$ transformations to the Southern Ocean, including Speer et al. (2000), Iudicone et al. (2008), Downes et al. (2011), Sallee et al. (2013), Downes et al. (2015), Cerovecki and Mazloff (2016), and Abernathey et al. (2016).

A difficulty that arises when using diagnostic frameworks is that their formulation may not reflect the underlying complexity of the system under study. An unexamined assumption of these Southern Ocean studies is that the transformation of water among density classes corresponds directly to the transformation of the SAMW, AAIW, and CDW water masses.

We check this assumption by combining the water mass transformation framework with independent estimates of the extents of the water masses. We first conduct a $\theta - S$ census in which water masses are identified using defining characteristics from the observational literature and then compute water mass transformations where surface fluxes and the resulting density transformations are calculated as a function of potential temperature and salinity, $T(\theta, S)$. These techniques are independent of each other but their results can be depicted on the same $\theta - S$ plane.

This combination of techniques introduces some semblance of the scientific method into the analysis process. While it is impossible to use the scientific method in the strict sense – we cannot run independent control and experimental studies of the circulation of the Southern Ocean – this technique challenges the hypothetical formation mechanisms suggested by the water mass transformation framework with independent data from the $\theta - S$ census.

The resulting methodology exposes misconceptions about the structure of the Southern Ocean and reveals simple and conspicuous relationships between surface fluxes and water mass transformations. The simplicity of these relationships contrasts with the convoluted results of studies employing $T(\sigma_\theta)$ transformations since they attribute multiple types of surface fluxes (often of opposing sign) to the formation of specific water masses. This is because the density control volumes employed by these $T(\sigma_\theta)$ transformations do not isolate individual water masses; instead, each control volume includes a combination of water masses and surface zones. Furthermore, we demonstrate how the results of studies employing $T(\sigma_\theta)$ transformations can be recovered from $T(\theta, S)$ transformations by taking path integrals along isopycnal contours in the $\theta - S$ plane.

The critical misunderstanding present in prior studies is that water masses cannot be identified by their density alone since colder, fresher AASW overlaps in density with these warmer, saltier subsurface water masses.

This conflation of surface waters with subsurface water masses is present in many studies in part because comprehensive descriptions of these water masses are nearly absent within Southern Ocean water mass transformation studies. We begin by describing the SOSE dataset used in this study and its model formulation. Then we review the water masses and surface zones of the Southern Ocean.

We conclude by discussing the results gleaned from prior studies that employ $T(\sigma_\theta)$ transformations and illustrate how their conclusions contradict the observational literature. We reevaluate these conclusions using $T(\theta, S)$ transformations and demonstrate how the results are consistent with observations.

4.3 SOSE Model Configuration

We use SOSE (Mazloff et al., 2010), which is an implementation of the Massachusetts Institute of Technology General Circulation Model (MITgcm) (Marshall et al., 1997) in an eddy-permitting configuration with roughly 1/6° horizontal resolution and 42 vertical levels. Vertical resolution starts at 5m near the surface and gradually increases to 250m in the abyss. The model time step is 900 seconds. The model domain spans all longitudes and ocean latitudes south of 24.5°S. It is constrained to a variety of in situ and remotely sensed observations using an adjoint model. The experiment runs throughout the years 2005-2010. Since the original SOSE integration did not save the atmosphere/ice/ocean flux terms necessary for computing water mass transformations, this study uses monthly means from a second SOSE integration described in the supplementary material of Abernathey et al. (2016).

SOSE is a widely studied simulation of the Southern Ocean with several known shortcomings. Antarctic Bottom Water (AABW) is not formed as efficiently within SOSE as it is in other models (Mazloff et al., 2010). Additionally, large open-ocean polynyas form in the simulation (most prominently in 2005 and 2006) even though such polynyas did not actually form during those years in the Southern Ocean (Aguiar et al., 2017). Despite these drawbacks, SOSE remains a tool with which surface water mass transformations can be computed because there are many observations within the surface layer and the simulation is constrained by these observations.

4.4 Background on Fronts, Surface Zones, and Water Masses

Much of the confusion in the water mass transformation literature arises from a misunderstanding of what, exactly, is meant by the term "water mass." The concept of a water mass was first introduced by Helland-Hansen (1916) while constructing temperature-salinity curves of soundings from the North Atlantic. He noted that much of the region could be represented by a temperature-salinity curve with a particular shape which reflected exposure to local atmospheric conditions. Departures from this shape in certain soundings indicated the presence of water masses advected from remote locations. His deduction relies upon conservation laws: water masses formed with a particular temperature-salinity composition retain their heat and salt content as they are advected away from their formation locations – at least for some period of time before diffusion mixes them into their surroundings. These ideas have a long history within the oceanographic discipline. Sverdrup et al.

(1942) note in their prominent textbook, "Water masses can be classified on the basis of their temperature-salinity characteristics, but density cannot be used for classification, because two water masses of different temperatures and salinities may have the same density."

Despite this, many studies continue to use density to classify water masses. In order to illustrate the shortcomings of such an approach, we first describe a methodology for conducting a $\theta - S$ census to classify the composition of water masses and surface zones. We then continue by reviewing the major water masses, fronts and zones of the Southern Ocean to give meaning to the census. The hydrographic extent of certain zones also correspond to the extent of surface water masses – for example, the Subantarctic Zone also represents the extent of Subantarctic Surface Water – but this correspondence does not hold for all zones. Thus we explain where relevant subsurface water masses exist in relation to these fronts and zones. While these features have been extensively described elsewhere, a short review is helpful to understand the concepts in this study. We also attempt to aid the reader by noting when prominent works in the literature denote the same features by different names.

4.4.1 Fronts and Surface Zones

Orsi et al. (1995) describe four fronts – three of which are related to the Antarctic Circumpolar Current (ACC) – that partition the Southern Ocean into five surface zones. Using these fronts to classify SOSE output is slightly awkward since the positions of the fronts are derived from hydrographic data collected prior to 1990 and SOSE runs from 2005-2010. However we use them primarily to help the reader qualitatively understand the broad $\theta - S$ properties of the Southern Ocean.

The four fronts – and their brief descriptions – are, in order from north to south, (Fig. 4.2):

1. STF: first described by Deacon (1937a), the STF separates the relatively warm, salty Subtropical Surface Water from the relatively cold, fresh Subantarctic Surface Water (SASW). Orsi et al. (1995) updated Deacon's definition by using $\theta - S$ distributions at 100 m depth instead of surface values.

2. SAF: the northern most of the three fronts associated with the ACC, Whitworth and Nowlin (1987) relate the SAF to a rapid increase in the depth of the salinity minimum within a meridional cross section. We note that applying this definition to SOSE output results in a relatively close match of the SAF contour from Orsi et al. (1995) throughout all longitudes

except in the Southeast Pacific basin. There, the contour traced by the salinity minimum definition extends about 5-10° farther north than Orsi et al.'s contour (not shown).

3. PF: the PF is identified by a large gradient in surface temperature as temperatures drop to near freezing values south of the front. Gordon (1971) discusses how at some longitudes it appears as if AASW sinks at the location of the front, suggesting a convergent structure, while at other longitudes the circulation appears to be divergent. Thus this feature is referred to in the modern literature as a front rather than a convergence or divergence. The surface waters south of the PF are dominated by a relatively cold, fresh water mass (described further below) known as AASW.

4. sACCF: Orsi et al. (1995) first identified the circumpolar extent of the sACCF. The sACCF does not separate two distinct surface water masses since the surface water south of the PF is considered to be AASW. However, they note that the Southern Boundary of the ACC, which is in the vicinity of the sACCF roughly coincides with the most poleward extent of Upper Circumpolar Deep Water (UCDW) (described below).

These fronts divide the Southern Ocean into five surface zones which are, from north to south, the Subtropical, Subantarctic, Polar Frontal, Antarctic, and Southern Zones (Fig. 4.2C). Many prior studies describe everything south of the PF using the term "subpolar regime" which encompasses both the Antarctic and Southern Zones (Orsi et al., 1995). Furthermore, in even earlier descriptions (e.g. Sverdrup et al. 1942) the surface waters of the Southern Ocean were partitioned simply into SASW and AASW. In contrast with SASW, AASW is usually vertically stable (Gordon, 1971) as it overlies CDW (described below) which is much saltier and thus denser than AASW. AASW displays a wide range of $\theta - S$ characteristics; Talley et al. (2011) denote its range as $-1.9°C < \theta < 4.0°C$, $33.0\ g/kg < S < 34.5\ g/kg$. The seasonal cycle of heat loss, ice formation, heat gain and ice melt creates seasonally forming types of AASW (Wong et al., 1998): Summer Water ($-1.8°C < \theta < 2.1°C$, $30.6\ g/kg < S < 34.2\ g/kg$) and Winter Water ($-1.9°C < \theta < 1.5°C$, $34.2\ g/kg < S < 34.5\ g/kg$). We note that these reported ranges are based off of different data collected over different times so there are discrepancies in the definitions: the lower salinity bound for Wong et al.'s Summer Water exceeds the lower salinity bound for Talley et al.'s AASW. The freshest waters of the Southern Zone are typically associated with the formation of Summer Water while the saltiest waters are typically found on the continental shelves.

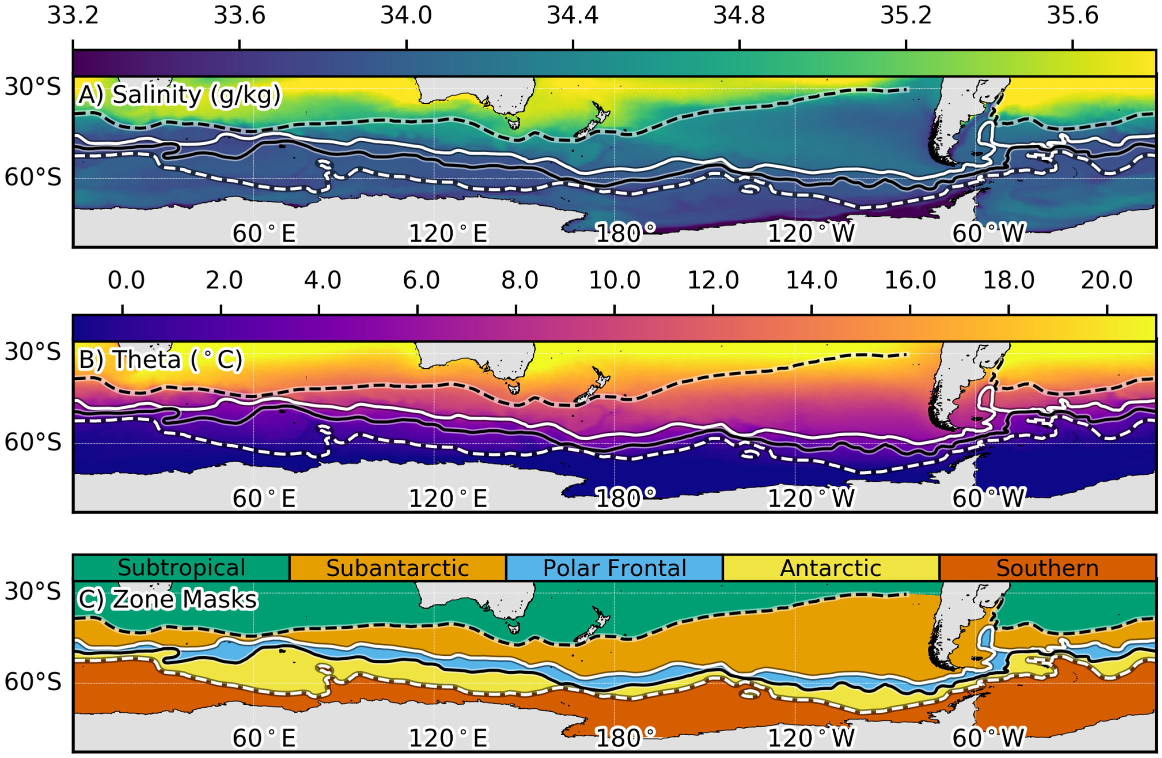
33.2
33.6
34.0
34.4
34.8
35.2
35.6
30°S
60°S
A) Salinity (g/kg)
60 ° E
120 ° E
180°
120 ° W
60 ° W
0.0
2.0
4.0
6.0
8.0
10.0
12.0
14.0
16.0
18.0
20.0
B) Theta (°C)
Subtropical
Subantarctic
Polar Frontal
Antarctic
Southern
C) Zone Masks

Figure 4.2: A) The mean surface salinity field (g/kg; shaded) for years 2005-2010 from SOSE (Mazloff et al., 2010) and climatological positions of the four Southern Ocean fronts from (Orsi et al., 1995). The fronts, from north to south: STF (black dashed line), SAF (white solid line), PF (black solid line), and sACCF (white dashed line). B) Same as A except showing the mean surface θ field (°C; shaded). C) The surface zone masks delineated by the fronts of the ACC (shaded according to the colorbar above the panel). The extent of each mask is used to assign each surface grid point into a specific zone when conducting the $\theta - S$ census.

4.4.2 Relevant Water Masses

In order to conduct a census of Southern Ocean water masses we first review the defining features of each of the water masses under study. Within the census we only include water volumes which meet the specific criteria used to identify the water mass, which is typically a combination of hydrographic extent and some defining characteristic of the water mass such as its $\theta - S$ composition or vertical stability. While we discuss several water masses in this section we provide a longer description of SAMW than the others due the pedagogical value it provides in illustrating the concepts discussed in this paper.

Subantarctic Mode Water Mode waters are a type of water mass with a large volume and hydrographic extent. "Mode" is used to indicate mode water's prevalence in a $\theta - S$ census akin to how the mode is the most common member of a mathematical set. Mode waters are well-mixed (low vertical stability) layers occurring in the upper pycnocline. These well-mixed layers are largest in volume during the late winter, when surface heat loss destabilizes the upper ocean. The well-mixed layers persist beneath the seasonal restratification of the mixed layer during the onset of spring. SAMW has the greatest hydrographic extent of all mode waters (Hanawa and Talley, 2001) and it was first described by McCartney (1977) who identified it as a thermostad (a thick layer of water with homogeneous temperature) occurring immediately north of the SAF. McCartney observed that SAMW exists throughout the Southern Ocean and in a wide range of densities (his Fig. 4). McCartney observed its most-equatorward and lightest occurrence off the coast of Argentina (roughly 32°S, 50°W and $26.5\sigma_\theta$) and its most-poleward and densest occurrence off the coast of Chile (roughly 43°S, 80°W and $27.1\sigma_\theta$).

Hanawa and Talley (2001) depict a different hydrographic extent for SAMW (their Plate 5.4.3) which does not include any SAMW in the Southern Atlantic Ocean. They instead show SAMW extending north past the STF into subtropical South Indian Ocean. Their review classifies the South Atlantic mode waters as a different type of mode water, Subtropical Mode Water, following Provost et al. (1999).

Antarctic Intermediate Water The process by which near-surface waters sequester dissolved gasses may be related to the process by which SAMW becomes AAIW. AAIW is a water mass with a very large hydrographic extent that spreads at intermediate depths, generally beneath 1000m. It lies beneath the high-salinity Subtropical Central Waters (SACW; Emery and Meincke 1986) and above CDW. AAIW can be differentiated from other water masses at intermediate depths by its relatively low salinity compared to CDW (e.g. Sverdrup et al. 1942, Emery and Meincke 1986), high oxygen content (Suga and Talley, 1995), and high silicate concentration (Tsuchiya, 1989). Competing paradigms exist within the literature with respect to the formation site of AAIW. Sverdrup et al. (1942; their Fig. 209A) and Emery and Meincke (1986; their Fig. 2) claim that AAIW is formed at nearly all longitudes along the SAF. McCartney (1977) and Tsuchiya and Talley (1998) claim that AAIW is formed from the coldest and densest SAMW off the coast of Chile. McCartney in particular noted that the coldest, densest version of SAMW in the Eastern South Pacific Ocean has a $\theta - S$ composition that roughly matches the $\theta - S$ composition of AAIW suggesting that SAMW transforms into AAIW and thus ventilates much of the Southern Hemisphere thermocline. He notes that this process occurs north of the SAF. In contrast, modeling studies such as Saenko and Weaver (2001) and Abernathey et al. (2016), the latter of which employs Walin's framework, conclude that sea ice advection and sea ice melt south of the SAF is responsible for forming AAIW. Regardless of which paradigm is correct, they agree that AAIW is a downwelling water mass which descends in the Subantarctic Zone and spreads northward.

Circumpolar Deep Water Finally, we describe CDW and its variants. CDW is a water mass which encircles the Antarctic Continent. Wong et al. (1998) define its broad $\theta - S$ characteristics: $0.0°C < \theta < 2.0°C$, $34.67\ g/kg < S < 34.75\ g/kg$. Whitworth et al. (1998) depict a zonal gradient in the local maximum temperature of CDW (their Fig. 1) in which the warmest local maximum temperatures are observed north of the Bellingshausen Sea ($\theta \approx 2.0°C$) and decrease as observations move westward around the continent, finally reaching the coldest local maximum temperature in the Weddell Sea ($\theta \approx 0.4°C$). This property gradient reflects CDW's relationship to the deep waters of each basin (Talley et al., 2011): North Atlantic Deep Water (NADW), Indian Deep Water (IDW), and Pacific Deep Water (PDW). CDW is often partitioned into UCDW and Lower Circumpolar Deep Water (LCDW) water masses. UCDW is distinguished by its low oxygen content while LCDW is distinguished by its high salinity content (Orsi et al., 1995).

CDW becomes colder and fresher as it moves from the open ocean onto the Antarctic Slope; the resulting water is distinguished as a distinct water mass known as Modified Circumpolar Deep Water (MCDW). Wong et al. (1998) differentiates these water masses by defining MCDW with slightly colder and fresher properties than CDW: $-1.5°C < \theta < 1.0°C$, $34.2\ g/kg < S < 34.67\ g/kg$. Whitworth et al. (1998) note that MCDW should be defined as being colder and fresher than the local offshore composition of CDW.

4.5 Methodology

We apply two complimentary techniques within this paper: conducting a $\theta - S$ census of the Southern Ocean and computing water mass transformations as a function of θ and S. While these techniques are independent, their results can easily be compared on the same $\theta - S$ coordinate plane. We contrast these methodologies to those used in prior studies which attempt to describe the transformation of water masses using density class control volumes.

4.5.1 $\theta - S$ censuses

Following Pollak (1958), Montgomery (1958), and Cochrane (1958), we conduct a potential temperature-salinity-area ($\theta - S - A$) census of surface zones and a potential temperature-salinity-volume ($\theta - S - V$) census of water masses. For each surface zone and water mass we create two-dimensional arrays of bins spanning the $\theta - S$ plane. At each SOSE time step we iterate through the all surface grid points for surface zones and all volume grid points for water masses and match the grid point to a surface zone or specific water mass (if it meets the criteria outlined in the following section). We then map the composition of the grid point to the relevant $\theta - S$ bin and add the surface area or volume of the grid point to the bin.

After completing this procedure we are left with several censuses where the value of each bin is the total surface area or volume of water matching the bin's $\theta - S$ composition. We compute the total surface area or volume of each census and then we arrange the $\theta - S$ bins in descending order. We iterate through these ordered lists and record the magnitude of the surface area or volume at which the cumulative area or volume reaches 90% of the total. We use this threshold value to demarcate the contour which outlines the $\theta - S$ extent of each water mass or surface zone in Fig. 4.2. To avoid confusing the latitude/longitude spatial areas of these water masses and surface zones with their corresponding $\theta - S$ areas, we refer to the $\theta - S$ areas traced out by these $\theta - S - A$ & $\theta - S - V$ census contours as "sectors."

4.5.2 Criteria for Distinguishing each Water Mass

Subantarctic Mode Water While McCartney initially identified SAMW as a thermostad, more recent studies instead identify SAMW using its low potential vorticity (PV) signature – e.g. Hanawa and Talley (2001), Sloyan et al. (2010), Hartin et al. (2011) – since PV is assumed to be approximately conserved under adiabatic motion. These studies use the planetary component of potential vorticity (PV) (Hanawa and Talley, 2001) to identify regions of low vertical stability:

$$PV = \frac{f}{\rho}\frac{\partial \rho}{\partial z} \tag{4.1}$$

where f is the Coriolis parameter. We use a first-order finite difference between successive vertical layers to compute $\partial\rho/\partial z$. We use the equation of state from Jackett and McDougall (1995) to compute ρ and delineate the extent of mode waters using a threshold value of $|PV| \leq 3\times10^{-10} m^{-1}s^{-1}$ (Wong and Johnson, 2003) and $26.5 < \sigma_\theta < 27.1$ (Hanawa and Talley, 2001). There is a degree of ambiguity when using PV to identify MW extent since the seasonal mixed layer also exhibits low vertical stability. To account for this, we exclude the grid levels encompassing approximately the uppermost 100m (when using first-order finite differences for partial derivatives on the SOSE grid, this means excluding the seven uppermost finite differences, since the seventh is centered at a depth of 94.5m) since mode waters are observed at deeper depths in the upper pycnocline. Additionally we exclude the Brazil-Malvinas Confluence from this survey, since it exhibits low vertical stability but it possesses a distinct $\theta - S$ composition that is warmer and fresher than the nearby mode waters.

While potential vorticity is widely used to describe mode waters, one drawback of its use is that it reflects the composite influence of both the vertical gradients of potential temperature and salinity upon the vertical stability of a water column. We can enhance our understanding by using alternative metrics which accentuate the relative influence of the potential temperature and salinity gradients upon vertical stability. Two commonly used metrics exist: the density ratio and the Turner angle. The density ratio is given by Turner (1973):

$$R_\rho = \frac{\alpha_T}{\beta_S}\frac{\partial\theta/\partial z}{\partial S/\partial z} \tag{4.2}$$

where α_T is the thermal expansion coefficient and β_S is the haline contraction coefficient. We see that R_ρ quantifies the relative effects of the vertical gradients of potential temperature (in the numerator) and salinity (in the denominator) upon the vertical gradient of potential density. The Turner angle (Ruddick, 1983) is the projection of the density ratio onto the angles contained within a unit circle (Radko, 2013):

$$Tu = 135^\circ - arg\left(\beta_S \frac{\partial S}{\partial z} + i\alpha_T \frac{\partial \theta}{\partial z}\right) \tag{4.3}$$

in a manner that is intended to simplify the description of vertical stability. When $-90^\circ < Tu < -45^\circ$ the vertical gradient of potential temperature is unstable but the water column is stable overall due to the stability of the vertical gradient of salinity. Conversely, when $45^\circ < Tu < 90^\circ$ the vertical gradient of salinity is unstable but the water column is stable overall due to the stability of the vertical gradient of potential temperature.

Antarctic Intermediate Water Since the characteristics by which AAIW is recognized are less precise than for SAMW – it is identified as a low salinity water mass which lies beneath SACW and above CDW – and because AAIW has such a large hydrographic extent, we limit our census to a specific control volume which approximates the depth and region of AAIW formation. We conduct our $\theta - S$ census at the SOSE model z-levels between 600m and 1000m depth in the Subantarctic Zone. These depths are beneath the deepest penetration of the mixed layer in late winter (Holte and Talley, 2009) and above the depth at which AAIW begins to spread northward.

Circumpolar Deep Water As with AAIW, we use hydrographic extent to conduct our CDW census, excluding waters shallower than 200m in order to omit AASW and warmer than 2.0°C to omit AAIW. We also exclude waters north of the PF in order to omit NADW and exclude waters south of the 2825 m isobath surrounding Antarctica to omit the Antarctic shelf waters.

4.5.3 Transformations

For our transformation analysis we partition surface freshwater and heat fluxes into six components: heat gain, heat loss, precipitation, evaporation, ice melt, and brine rejection. This differs from Abernathey et al. (2016) who only partition the sea ice freshwater flux into brine rejection and ice melt. They refrain from partitioning the heat fluxes into heat gain and heat loss and the atmosphere to ocean freshwater fluxes into precipitation and evaporation, claiming that this selective "decomposition is valid because (unlike evaporation and precipitation) ice freezing and melt cannot both occur in the same place at the same time." We note, however, that the output upon which they conduct their calculations is averaged in time. While a given surface grid point cannot be both melting and freezing at a single model time step, that grid point can undergo freezing, melting, evaporation, precipitation, heat gain, and heat loss during the averaging period (as stated earlier in Section 4.3, the model time step is 900 seconds so there are 480 time steps averaged into each five-day output file used in their study). The judicious way to compare these fluxes is to treat them identically and partition each into positive and negative fluxes. Since this analysis is done upon time-averaged data each of these six components represent net terms over each averaging period.

We begin our derivations of water mass transformation analysis by noting that the specific formulation of density fluxes used in SOSE differ from the formulation used in observational studies such as Speer and Tziperman (1992) because SOSE parameterizes surface density fluxes (Adcroft et al., 2018) using a slightly modified version of the bulk formulae described by Large and Yeager (2004).

The change in density of the ocean's surface layer is related to the flux of heat and freshwater:

$$\frac{\delta \sigma_\theta}{\delta t} = \left(\frac{\delta \sigma_\theta}{\delta \theta}\right)_S \frac{\delta \theta}{\delta t} + \left(\frac{\delta \sigma_\theta}{\delta S}\right)_\theta \frac{\delta S}{\delta t} \tag{4.4}$$

where we use δ rather than ∂ to indicate that the derivatives are not infinitesimal and we include a subscript on each derivative to indicate which quantity is being held constant. While the coefficients of each term on the RHS of the equation are recomputed at each time step, this is a linearization due to the time averaging, which is why we refrain from using ∂ notation. The change in temperature due to heat flux in SOSE is:

$$\frac{\delta \theta}{\delta t} = \frac{Q}{\rho_o C_p} \tag{4.5}$$

where Q is the 'TFLUX' or total heat flux field in SOSE, $\rho_o = 999.8\ kg\ m^3$ is the constant reference density and $C_p = 4000\ J\ {}^\circ C^{-1}\ kg^{-1}$ is the specific heat of seawater employed by the model. We partition the heat flux into two terms where $Q < 0$ is heat loss and $Q > 0$ is heat gain.

The change in salinity due to freshwater flux is:

$$\frac{\delta S}{\delta t} = \frac{S_o(W_{A\to O} + W_{I\to O})}{\rho_o} \tag{4.6}$$

where $W_{A\to O}$ is the atmosphere-to-ocean freshwater flux, $W_{I\to O}$ is the sea ice-to-ocean freshwater flux, and $S_o = 35\ g/kg$ salinity is a constant used by the model to convert a freshwater flux into a virtual salinity flux. The freshwater fluxes are derived from three SOSE fields: 'SIatmFW' which is the total freshwater flux from the atmosphere ($W_{A\rightarrow I} + W_{A\rightarrow O}$), 'SIempmr' which is the total freshwater flux into the ocean ($W_{I\rightarrow O}+W_{A\rightarrow O}$), and 'SIsnPrcp' which is the freshwater flux from the atmosphere to the sea ice ($W_{A\rightarrow I}$). Subtracting 'SIsnPrcp' from 'SIatmFW' recovers the atmosphere-to-ocean freshwater flux:

$$W_{A\rightarrow O} = W_{A\rightarrow I} + W_{A\rightarrow O} - W_{A\rightarrow I} \tag{4.7}$$

while subtracting the atmosphere-to-ocean freshwater flux from 'SIempmr' recovers the sea ice-to-ocean freshwater flux:

$$W_{I\rightarrow O} = W_{I\rightarrow O} + W_{A\rightarrow O} - W_{A\rightarrow O}. \tag{4.8}$$

The sign convention for freshwater fluxes in SOSE is that positive surface fluxes increase ocean salt content. Thus we partition the atmosphere-to-ocean freshwater flux into two terms where $W_{A\rightarrow O} < 0$ is precipitation and $W_{A\rightarrow O} > 0$ is evaporation. We also partition the sea ice-to-ocean freshwater flux into two terms where $W_{I\rightarrow O} < 0$ is ice melt and $W_{I\rightarrow O} > 0$ is brine rejection.

The other terms in Eq. 4.4 are the thermal expansion:

$$\alpha_T = \left(\frac{\delta\sigma_\theta}{\delta\theta}\right)_S \tag{4.9}$$

and haline contraction:

$$\beta_S = \left(\frac{\delta\sigma_\theta}{\delta S}\right)_\theta \tag{4.10}$$

coefficients computed by and used in the equation of state (Jackett and McDougall, 1995).

Water mass transformation studies typically compute a transformation rate, T, by taking the integral of Eq. 4.4 over area and time and analyzing the results as a function of the discretized independent variable σ_θ^i:

$$T(\sigma_\theta^i) = \int dt \int\int dxdy \frac{\delta\sigma_\theta^i}{\delta t} \tag{4.11}$$

where σ_θ^i represents a discrete range of potential densities within some interval $\Delta\sigma_\theta$. The formation rate, F, is the net convergence of transformation within a density range:

$$F(\sigma_\theta^i)\Delta\sigma_\theta = -[T(\sigma_\theta^{i+1}) - T(\sigma_\theta^i)] \tag{4.12}$$

Following Speer and Tziperman (1992) we interpret Eq. 4.11 by analyzing the results as a function of two discretized independent variables, θ_j and S_k:

$$T(\theta_j, S_k) = \int dt \int\int dxdy \left[\left(\frac{\delta\sigma_\theta}{\delta\theta} \right)_{S_k} \frac{\delta\theta_j}{\delta t} + \left(\frac{\delta\sigma_\theta}{\delta S} \right)_{\theta_j} \frac{\delta S_k}{\delta t} \right] \tag{4.13}$$

where θ_j represents a discrete range of potential temperatures within some interval $\Delta\theta$ and S_k represents a discrete range of salinity within some interval ΔS.

In this case the formation rates due to freshwater and heat fluxes can be considered separately, where the value of one component is held constant:

$$F(\theta_j)\Delta\theta = -[T(\theta_{j+1}, S_k) - T(\theta_j, S_k)] \tag{4.14}$$

$$F(S_k)\Delta S = -[T(\theta_j, S_{k+1}) - T(\theta_j, S_k)] \tag{4.15}$$

We plot the transformation and formation results on the $\theta - S$ plane, where the discrete values of θ_j, S_k correspond to grid points in the plane. We also plot the sector contours from the surface zones and water mass censuses atop these results to enable a straightforward comparison. In order to get a sense of the temporal phase of the surface fluxes we save the month of the maximum transformation magnitude at each θ_j, S_k for each of the six density flux components in order to illustrate when each component is most active in the seasonal cycle.

The depiction of water mass transformations on the $\theta - S$ plane has been discussed in previous works including Speer and Tziperman (1992), Groeskamp et al. (2014), and Hieronymus et al. (2014). In contrast to those earlier studies, ours uses sector contours to aid in the interpretation of the results, and compares the interpretations gleaned from both Eq. 4.11 and Eq. 4.13 to illustrate how using $F(\sigma_\theta)$ to interpret water mass transformations can lead to incorrect conclusions (in areas such as the Southern Ocean where waters of starkly different $\theta - S$ compositions lie along the same isopycnals).

We also illustrate, following Speer and Tziperman (1992), how to recover the results of Eq. 4.11 from Eq. 4.13 by taking path integrals along lines of constant density:

$$T(\sigma_\theta = C) = \frac{1}{|\mathbf{r}|} \int_{\sigma_\theta = C} T(\theta, S) d\mathbf{r} \tag{4.16}$$

and how this approach is inadvisable in the Southern Ocean.

4.6 Results

4.6.1 Census Results

There are two aspects of the $\theta - S$ census which enable key insights into the structure of the Southern Ocean. The first is the ability to infer which subsurface water masses regularly outcrop by examining whether a particular water mass sector significantly overlaps with any of the surface zone sectors. The second is the ability to isolate distinctive features within the census and remap these features as a function of latitude and longitude in order to draw connections between the $\theta - S$ structure and processes which have previously been described in the observational literature.

Several prominent features emerge in Fig. 4.3A. The Subtropical Zone is the warmest and saltiest surface zone. The remaining zones get colder and fresher when traversing the ACC from north to south. While the Southern Zone is the coldest zone overall, it also exhibits the largest variance in its salinity values (ranging from roughly 32.8 - 34.6 g/kg) as the sector spreads out along the seawater/ice phase transition line at approximately -1.89°C. This variance reflects the interaction of the coupled atmosphere/sea ice/ocean system. The formation of sea ice acts to convert heat loss at the seawater/ice phase transition line into salinity gain via brine rejection. The melting of sea ice acts to convert heat gain by sea ice into freshwater gain by the ocean at or near the seawater/ice phase transition line, since the freshwater due to ice melt can flux into seawater that is warmer than the freezing point. By viewing these transformations in the $\theta - S$ plane we can see how this process confounds $T(\sigma_\theta)$ transformations – it spreads the Southern Zone sector horizontally along the seawater/ice phase transition line creating cold, fresh water that overlaps in density with SAMW.

We see that many surface zones and water masses occur within the SAMW density class control volume. The sectors for all five surface zones, along with the sectors for SAMW and AAIW all exist within the SAMW density class control volume. This establishes that a density class control

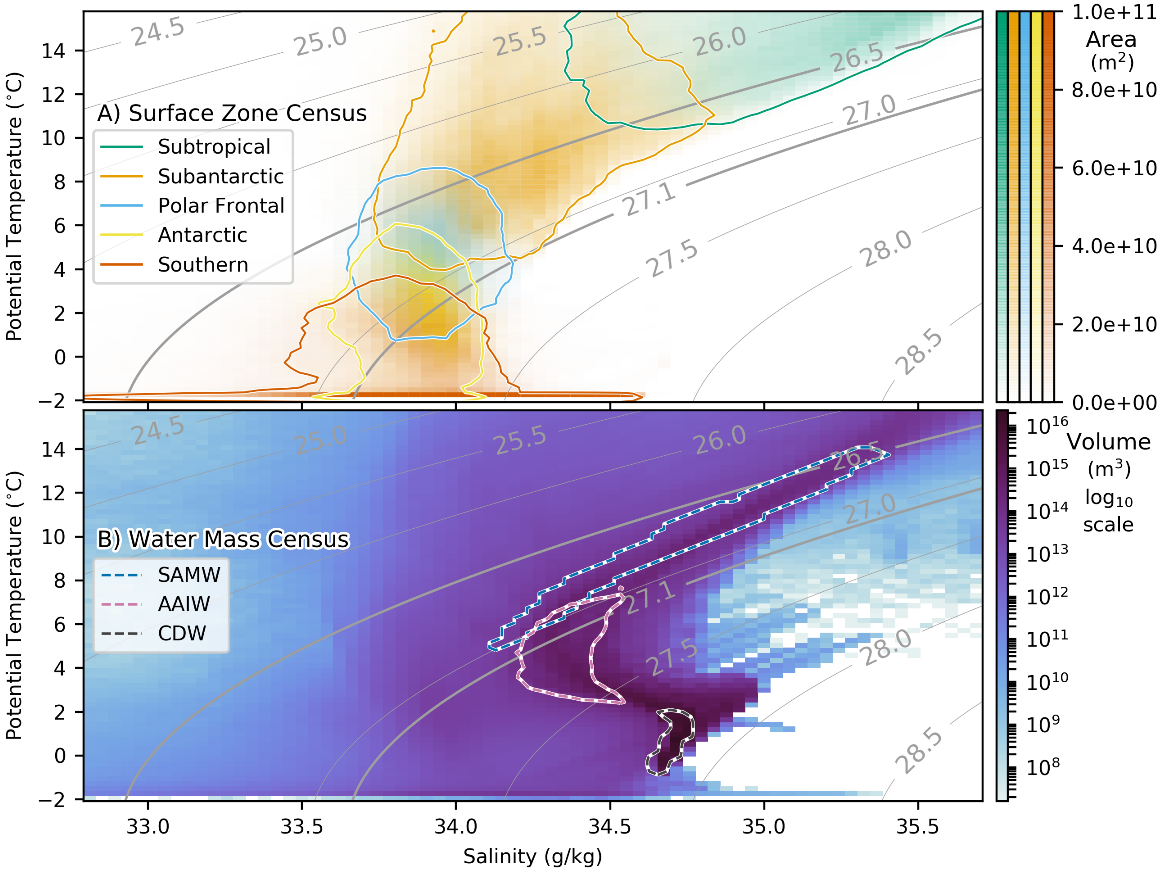

Figure 4.3: A) $\theta - S$ surface area census of the zones depicted in Fig. 4.2C (m^2, shaded for each section according to the corresponding color bar at the right of the panel). Solid contours outline the 90% surface area contour of each surface zone as described in Section 4.5.1. B) $\theta - S$ volume census of the SOSE domain (m^3, shaded $\log_{10}$ scale). Dashed contours outline the 90% volume contour of three water masses (SAMW, AAIW, CDW) as described in Section 4.5.1. Since the 26.5-27.1σ_θ density range is typically used to delineate the SAMW density class, the corresponding isopycnals are drawn in a heavier weight within the θ-S diagrams.

volume cannot adequately isolate a water mass. We can see from Fig. 4.3B that there is a significant volume of water contained within the SAMW density class control volume which lies outside of the SAMW water mass sector. The mean volume of seawater contained within the SAMW density class control volume ($2.42 \times 10^{16} m^3$) is approximately 3.4 times the mean volume of the SAMW water mass ($7.11 \times 10^{15} m^3$).

We also see that the SAMW sector has significant overlap with the Subtropical and Subantarctic Zones. We can map where SAMW occurs by applying Eq. 4.1 to the SOSE output. Doing so shows some agreement with both McCartney's and Hanawa and Talley's descriptions of SAMW extent (Fig. 4.4A). Small amounts of low-PV water are observed in the South Atlantic (consistent with McCartney) and the low-PV extent is also observed north of the SAF in the subtropical South Indian Ocean (consistent with Hanawa and Talley).

Applying Eq. 4.3 to the mode waters depicted in Fig. 4.4A shows a distinct pattern within the mode water extent – the northern waters within the mode water extent have an unstable vertical salinity gradient while the southern waters have an unstable vertical temperature gradient (Fig. 4.4B). The composition and location of the mode water with an unstable salinity gradient suggests a relationship between it and South Indian Central Water (Emery and Meincke, 1986) while the composition and location of the mode water with an unstable temperature gradient suggests a relationship between it and AAIW (McCartney, 1977).

We can understand this relationship better by considering the surface and subsurface sectors shown in Fig. 4.3 in more detail. Fig. 4.5 shows all the sector contours within one panel. It also helps to visualize the effect of the seasonal cycle on the surface values of θ and S by showing their mean values along three meridians in February (summer) and September (winter) 2005. The selected meridians approximate the positions of WOCE (Siedler et al., 2001) transects A12/S2 (7°E; Fig. 4.6), SR3 (145°E; Fig. 4.7) and P19 (89°W; Fig. 4.8), the last of which was occupied by the AAIW05 cruise during winter of 2005 (Chereskin, 2005). We selected these three transects after first completing the analysis along all 19 meridional transects that intersect the Southern Ocean in the WOCE Atlas and choosing a subset that represent their respective regions of the Southern Ocean.

Several notable features emerge from the seasonal migration of the surface values in Fig. 4.5. The P19 transect in the Southern Zone is near the seawater/ice phase transition line, thus its surface mean value primarily increases in S during the transition to from Summer to Winter reflecting the influence of freshwater fluxes caused by sea ice melt and formation. The A12 and SR3 transects in

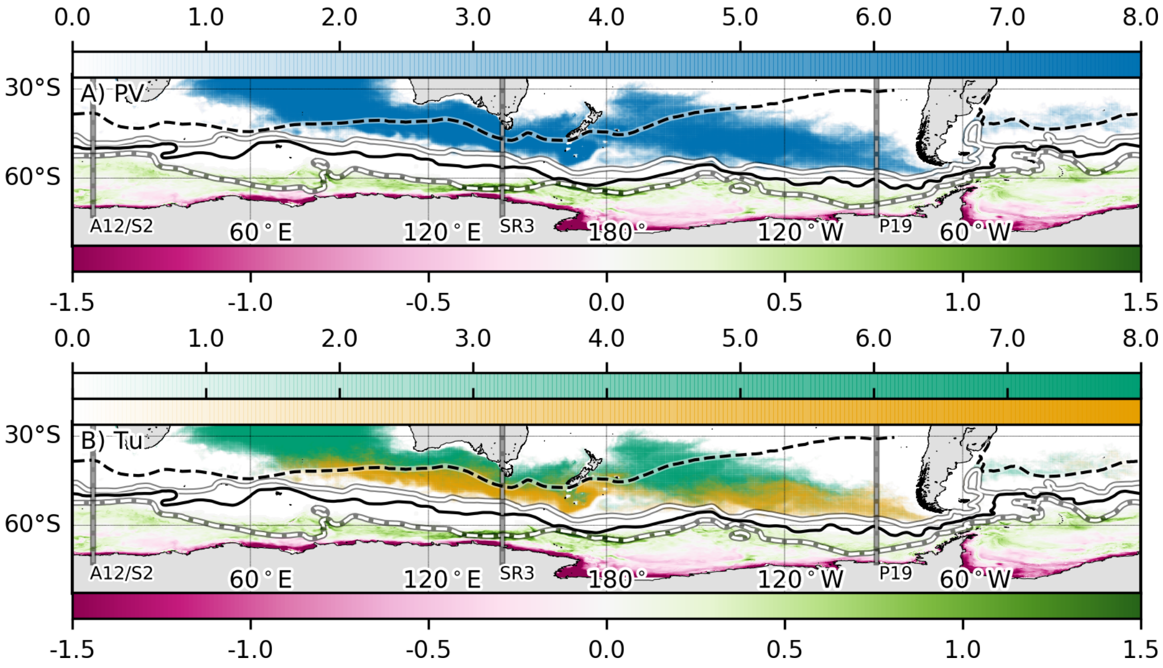

Figure 4.4: These figures depict mode water extent and the range of surface fluxes caused by the formation and melting of sea ice. A) Mean vertically integrated mode water volume (10^{10}m^3) where the mode water extent is delineated by the SAMW density range (26.5-27.1 σ_θ) and by the potential vorticity threshold $|PV| \leq 3.0 \times 10^{-10} m^{-1}s^{-1}$ (shaded in blue). We exclude the upper 100m from the integral so as to exclude the surface mixed layer. Also shown is sea ice redistribution freshwater flux (m/year) where negative flux due to brine rejection is shaded in magenta and positive flux due to ice melt is shaded in green. The climatological positions of the Southern Ocean fronts are the same as in Fig. 4.2. B) The same mean vertically integrated mode water volume except we use the Turner angle to partition the mode water into two different volumes in order to highlight the extent of waters with unstable vertical gradient of salinity (10^{10}m^3; shaded in bluish-green) and unstable vertical gradient of temperature (10^{10}m^3; shaded in orange).

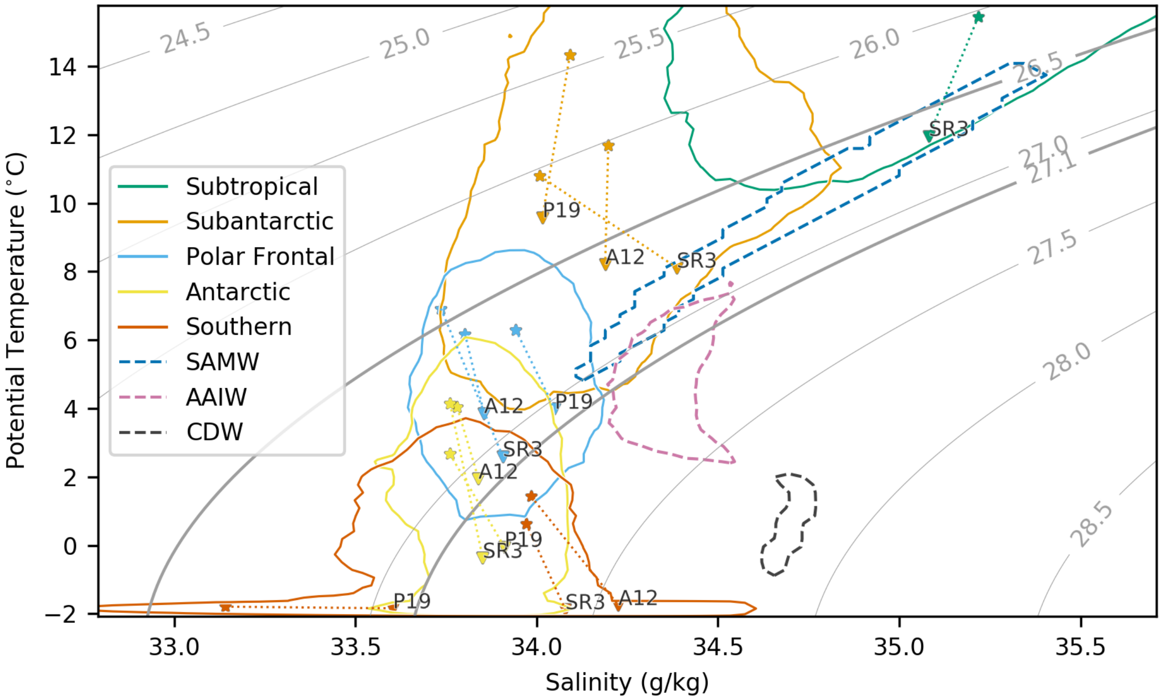

Figure 4.5: The mean surface $\theta - S$ composition along the A12/S2, SR3 and P19 transects where each marker is the average along a given transect within a surface zone in February 2005 (star markers) and September 2005 (triangle markers). The coloring of each marker corresponds to the surface zone within which the mean is computed and the winter and summer markers for each zone are connected by a dotted line. Each winter marker is annotated with the name of the transect. The solid and dashed sector contours for the surface zones and water masses are the same as in Fig. 4.3. The subtropical markers for the A12/S2 and P19 transects are all warmer than 16°C and thus exceed the θ limit for the figure.

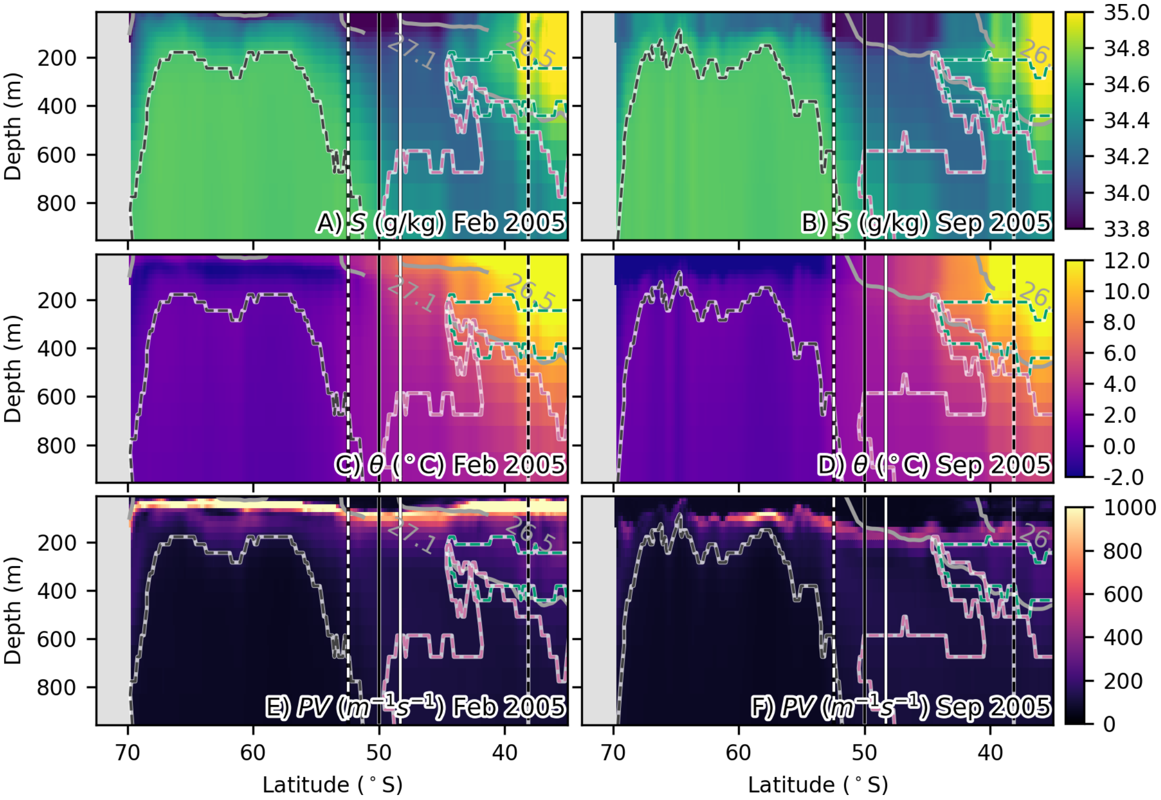

Figure 4.6: Latitude-depth transects along 7°E (approximating the track of the WOCE A12/S2 meridional section) for February 2005 (left column) and September 2005 (right column) for S (g/kg; top row), θ (°C; middle row), and PV ($\mathrm{m}^{-1}\mathrm{s}^{-1}$; bottom row). Climatological positions of the Southern Ocean fronts depicted by vertical lines: STF (dashed black), SAF (solid white), PF (solid black) and sACCF (dashed white). Gray contours are SAMW density class isopycnals (26.5 and 27.1 σ_θ). Dashed gray contour denotes the extent of CDW, dashed reddish-purple contour denotes the extent of AAIW, dashed bluish-green contour denotes the extent of SAMW with unstable vertical salinity gradient.

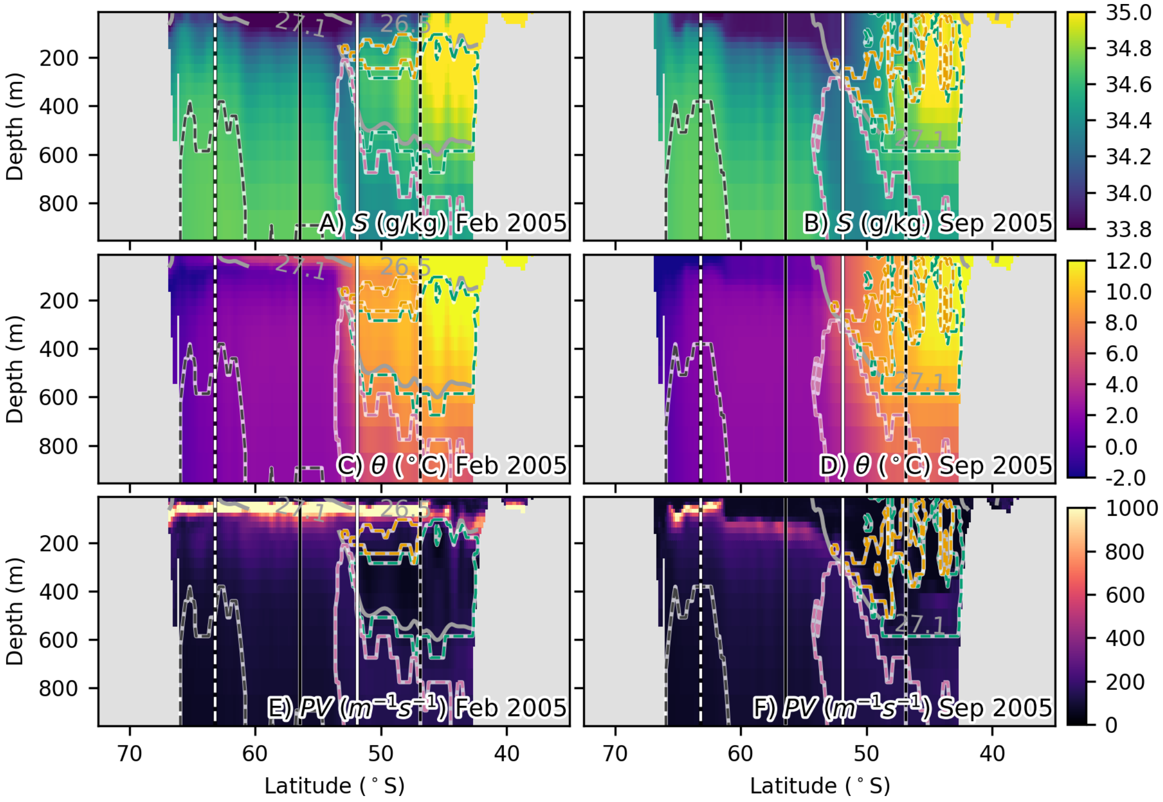

Figure 4.7: Latitude-depth transects along 145°E (approximating the track of the the WOCE SR3 meridional section). Contours and shading same as in Fig. 4.6 with an additional contour: dashed orange contour denotes the extent of SAMW with unstable vertical temperature gradient.

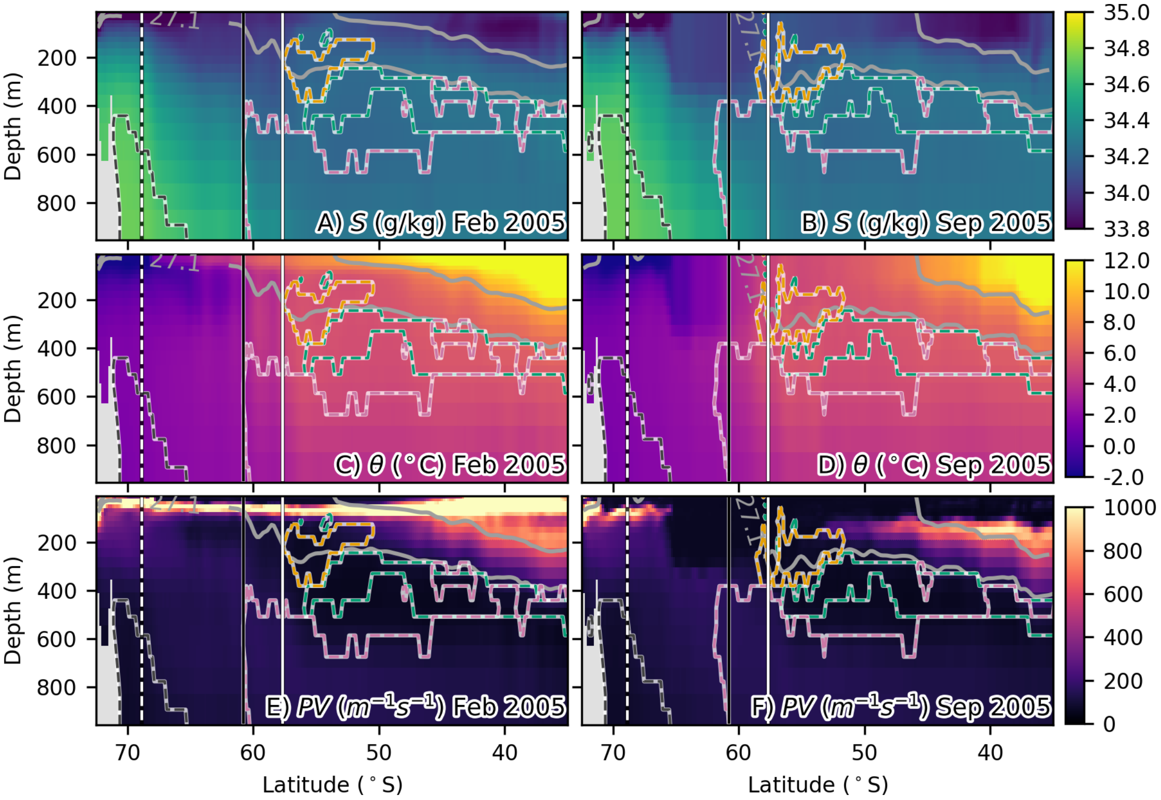

Figure 4.8: Latitude-depth transects along 89°W – approximating the track of the AAIW05 cruise (Chereskin, 2005) transect along the WOCE P19 meridional section. Contours and shading same as in Fig. 4.7. There is low-stability water that would be classified as a mode water using the low-PV criteria near the PF but it is not outlined with an SAMW contour in these panels because its density (approximately 27.2-27.3 σ_θ) lies beyond the SAMW density range used throughout this study. Comparing the September PV transect in E to the contemporaneous transects observed during AAIW05 (Hartin et al., 2011) reveals a discrepancy in the location of the deep near-surface low-PV layer in SOSE. The deepest penetration of low-PV water in SOSE is centered poleward of the polar front at roughly 62°S while the deep near-surface low-PV layer observed during the same time period during the AAIW05 Cruise was centered equatorward of the PF at roughly 57°S (Fig. 2a of Hartin et al. 2011).

the Southern Zone decrease in θ and increase in S during the transition from Summer to Winter, a behavior shared by all of the transects within the Antarctic and Polar Frontal Zones. The P19 and A12 transects in the Subantarctic Zone decrease in both θ and S while the SR3 transect decreases in θ but increases in S. This causes its winter composition to migrate into SAMW sector. The SR3 transect in the Subtropical Zone decreases both in θ and S and also migrates into the SAMW sector in the winter.

By examining the surface waters along the poleward sides of the transects in Figs. 4.6, 4.7, and 4.8 we can get a sense of the seasonal evolution of AASW. Winter Water is visible in panels C and D of these transects as a cold mixed layer which extends from the continent past the sACCF and which sometimes reaches the PF. During the spring, surface heat and freshwater fluxes due to ice melt and increased solar insolation decrease the density of the surface layer and form a high PV layer of Summer Water in the upper 50m. Winter Water remains as a subsurface temperature minimum from around 50-200m depth; its persistence throughout the warmer seasons was noted by Mosby (1934). While CDW along each transect shoals south of the sACCF, the Winter Water lies above the uppermost extent of CDW, insulating it from the surface.

The formation of Summer Water causes the SAMW density class control volume to shift poleward into the subpolar gyres. The 27.1 σ_θ isopycnal, which typically outcrops in the vicinity of the PF during the September transects, extends all the way to the Antarctic continent. While certain authors, such as Cerovecki and Mazloff (2016), interpret this poleward shift of the density class control volume as a shift in the location of SAMW formation, we can see that while the location of the isopycnals moves seasonally, the location of the mode waters along each transect does not. We interpret the results differently, noting that the SAMW density class control volume merely encompasses different water masses in different seasons. In the austral summer the control volume includes Summer Water south of the sACCF while in austral winter it does not.

The overlap of the densest waters of the Subantarctic Zone and lightest waters of the AAIW sector in Fig. 4.5 suggests that AAIW reaches the surface. By iterating through all of the surface grid points and noting where the surface waters match the composition of these overlapping sectors (Fig. 4.9), we can chart where AAIW surfaces to find that AAIW reaches the surface in the Southeast Pacific between 130°W and Drake Passage. This location coincides with the location of AAIW renewal described by McCartney (1977). Notably, Fig. 4.5 also shows that the CDW sector does not overlap with any surface zone sector. This result suggests that it does not broadly outcrop in

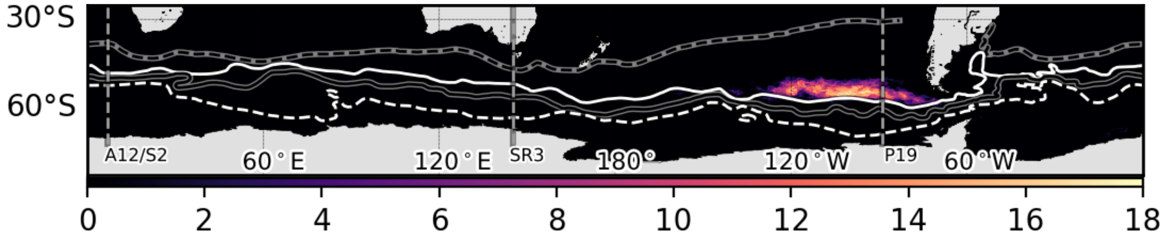

Figure 4.9: Number of months that water matching the $\theta - S$ composition of AAIW was detected at each surface grid point (shaded, out of a possible 60 total months). The shading was created by iterating through each surface grid point at each time step and checking whether the $\theta - S$ composition of the surface was within the overlapping Subantarctic Zone and AAIW sectors in the $\theta - S$ plane.

the Southern Ocean, a finding which contradicts many studies.

4.6.2 Transformation Results

We produced $T(\theta, S)$ transformation and $F(\theta, S)$ formation/destruction diagrams in Fig. 4.10 side-by-side to aid in their interpretation. Since the $F(\theta, S)$ formations result from taking the convergence of $T(\theta, S)$ along a particular axis (along the y-axis for heat transformations and along the x-axis for freshwater transformations) distinct patterns emerge. If the magnitude of a transformation along an axis steadily increases, reaches a maximum and then steadily decreases, the resulting formation and destruction will occur on opposing sides of the local maximum in formation magnitude. For example, when moving in the positive x-direction of Fig. 4.10TC, the net precipitation peaks at roughly 33.9 g/kg salinity. Since freshwater gain results in a loss of density at the surface, water is destroyed to the right of the precipitation peak (the magenta shading at values > 33.9 g/kg salinity in panel FC) and is formed to the left of the precipitation peak (the green shading at values < 33.9 g/kg salinity in panel FC).

These diagrams demonstrate how the $T(\sigma_\theta)$ framework is inadequate for accurate descriptions of the transformations between water masses. Imagine a water parcel in the middle of the Polar Frontal Zone sector (sky blue contour) at $\theta = 5.0$ °C and $S = 33.9$ g/kg. If it were to lose heat it would move toward the Antarctic Zone sector while if it were to gain salt it would move toward the AAIW sector (pink dashed contour). The $T(\sigma_\theta)$ framework treats these transformations identically – as increases in density – yet the resulting $\theta - S$ composition that is formed by each transformation is not the same. To borrow a concept from linear algebra, assuming the $T(\sigma_\theta)$ framework can appropriately describe water mass transformations would be akin to assuming that a single vector can span the

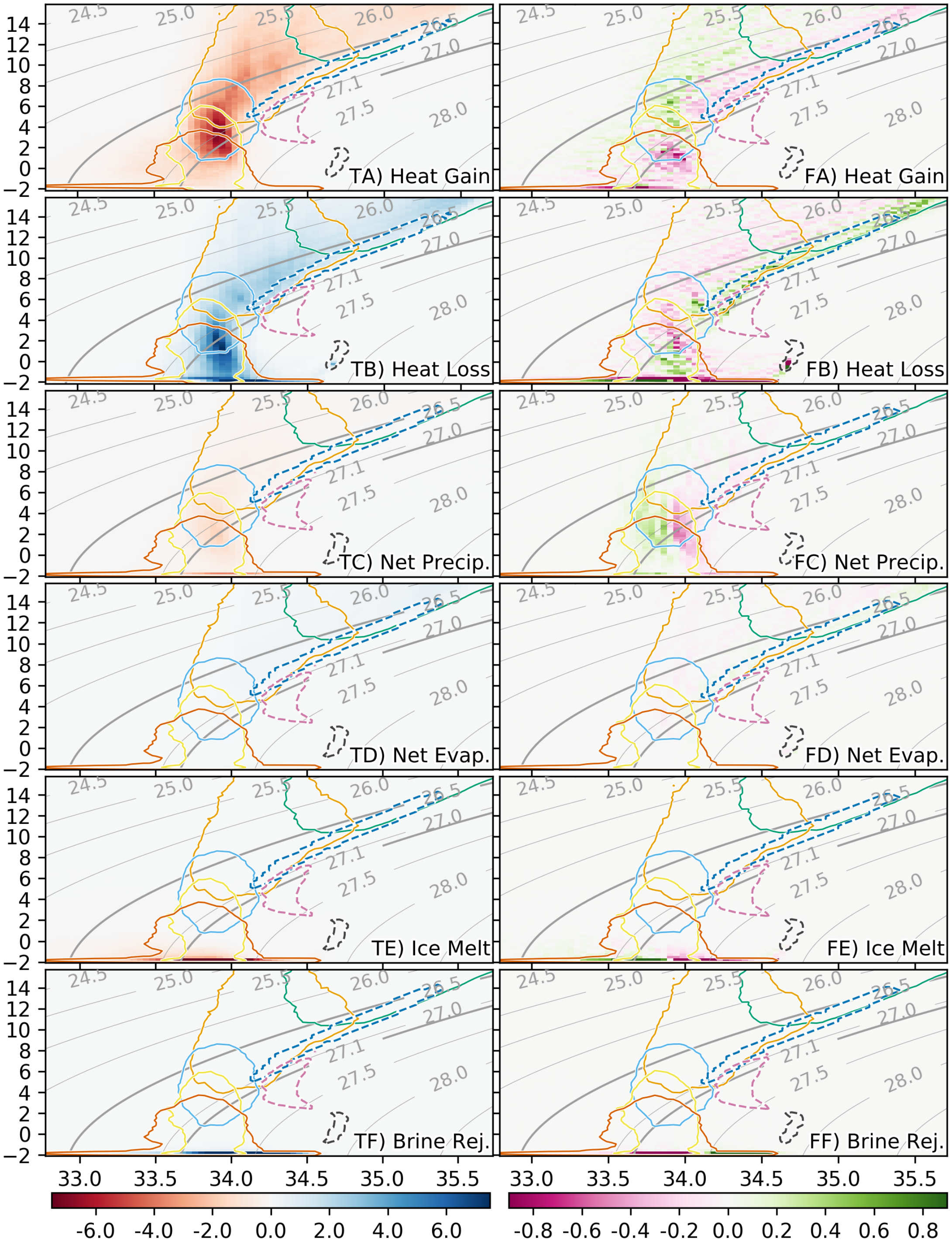

Figure 4.10: $T(\theta, S)$ surface transformations (in Sverdrups [Sv]; left column) and the resulting $F(\theta, S)$ formations (Sv; right column). X-axis for each panel is S (g/kg). Y-axis is θ (°C). The dashed blue contour corresponds to the SAMW sector, the dashed reddish-purple contour corresponds to the AAIW sector and the dashed dark gray contour corresponds to the CDW sector.

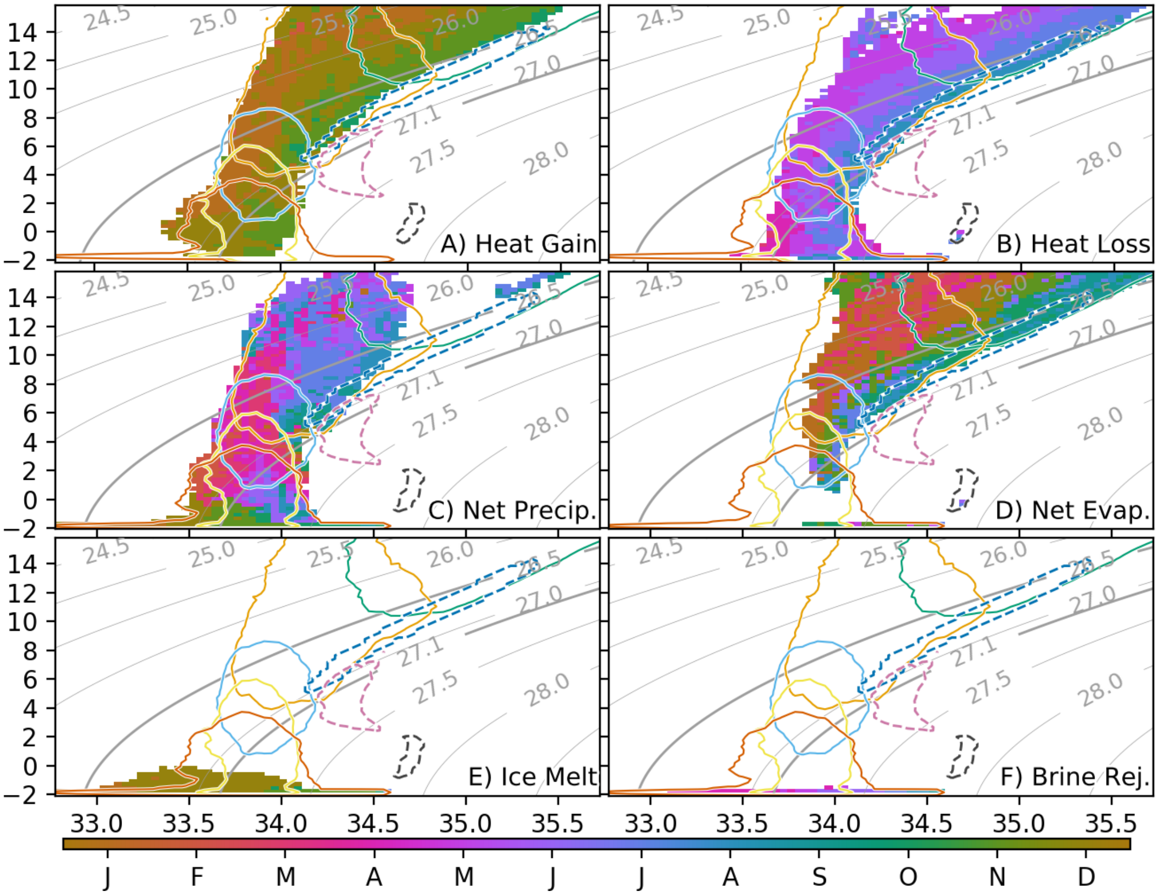

Figure 4.11: Phase (month) of maximum transformation by each surface component. The x-axis of each panel is salinity (g/kg); y-axis is potential temperature (°C). Contours are the same as the left column of Fig. 4.10.

$\mathbf{R}^2$ plane.

Additionally, to help understand the seasonality of transformations, we depict the month at which peak transformation occurs for a given $T(\theta_j, S_k)$ bin in Fig. 4.11.

4.7 Discussion

The $T(\theta, S)$ transformations provide a distinct vantage for interpreting Southern Ocean water mass transformations because they allow for differentiation of the subsurface water masses from the surface waters which lie atop them. Since these water masses are the focus of transformation studies we start with a discussion of the overall results of the transformation analysis and then discuss the specific implications for our understanding of the formations of CDW, SAMW and AAIW. In doing so, we

Table 4.1: Density range for CDW and its variants in water mass transformation studies. Note well: Sloyan and Rintoul (2001b) supplement their density calculations using $\theta - S$ composition and conclude that CDW is transformed into AASW which then is transformed into AAIW.

Study	*Nomenclature*	*Density Range (γ^n)*
Speer et al. (2000)	UCDW	27.5-28.0 kg/m^3
Sloyan and Rintoul (2000, 2001b)	UDW (a synonym of UCDW)	27.4-28.0 kg/m^3
Iudicone et al. (2008)	UCDW	27.8-28.0 kg/m^3
Downes et al. (2011)	NADW PDW IDW	27.5-28.1 kg/m^3 27.6-28.0 kg/m^3 27.5-27.9 kg/m^3
Abernathey et al. (2016)	UCDW	27.5-28.0 kg/m^3

highlight the different interpretation which $T(\theta, S)$ transformations provide when compared to $T(\sigma_\theta)$ transformations. We then continue by discussing which type of surface flux has the greatest influence over the Southern Ocean. We finish with a discussion of possible reasons why misconceptions about the Southern Ocean are so prevalent.

4.7.1 Water Mass Transformations

Circumpolar Deep Water

One of the central conclusions of $T(\sigma_\theta)$ transformation studies is that CDW outcrops in the Southern Ocean and is transformed into upper and lower branches – six such studies are listed in Table 4.1. In the case of Downes et al. (2011), CDW is differentiated into NADW, PDW, and IDW. These studies typically describe the transformation of CDW via freshwater and heat gain into an upper branch consisting of SAMW and AAIW and a lower branch consisting of AABW. The upper branch is what Speer et al. (2000) refer to as the "Diabatic Deacon Cell" in reference to Deacon's (1937a) description of the Antarctic Convergence.

In contrast to these studies, our $T(\theta, S)$ transformations do not depict significant outcropping of CDW since the CDW sector does not overlap with either the Antarctic or Southern Zones. While the surface transformations generally occur within the surface zone sectors (Fig. 4.10), one notable outlier is visible within the CDW sector, near its coldest and freshest edge. There, a heat loss transformation occurs (Fig. 4.10TB and Fig. 4.12A) at approximately $\theta = 0°C$ and $S = 34.67 g/kg$. Plotting the spatial extent of the heat loss transformations within the CDW sector reveals they occur in the Ross and Weddell Seas and are caused by the formation of sensible-heat polynyas within the

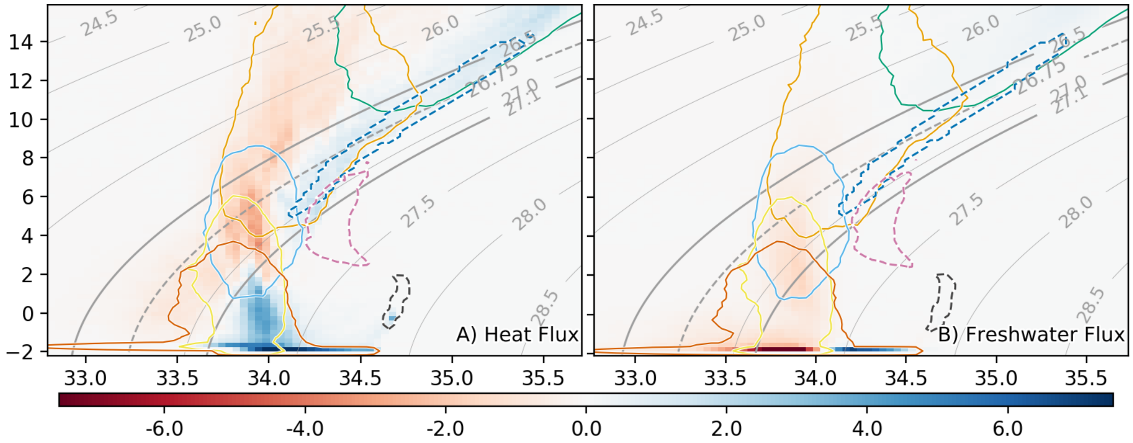

Figure 4.12: Net heat transformation (Sv, shaded) for surface heat flux and surface freshwater flux. The x-axis of each panel is S (g/kg); y-axis is θ (°C). The dashed lines depicting the 26.75 σ_θ isopycnal corresponds to the dashed vertical lines in Fig. 4.16.

model (Fig. 4.13).

Polynyas are large breaches within the sea ice cover. They are typically differentiated into two types – sensible and latent heat – depending upon the primary mechanism of heat loss that occurs within the polynya (Gordon and Comiso, 1988). Latent-heat polynyas tend to form along the Antarctic Coast, where katabatic winds advect sea ice away from the continent creating a breach along the shoreline. The surface water within the breach is typically at the freezing point and heat loss occurring within the polynya results in the production of new sea ice. Sensible-heat polynyas tend to form within the open ocean where breaches in the sea ice expose the sea surface to the frigid air above. The surface water within the breach is typically warmer than the freezing point and heat loss occurring within the polynya lowers the temperature of the seawater. Sensible-heat polynyas tend to form in the vicinity of shallow bathymetric features such as Maud Rise in the Weddell Sea. The breaches can be completely enclosed by sea ice or can form along the ice edges, in which case they are known as embayments.

The existence of these large sensible-heat polynyas in 2005 and 2006 is a model artifact: corresponding polynyas did not manifest near Antarctica during those years. We discuss the effects of these polynyas nonetheless because they represent a process that actually occurs in other years – most notably in 1974-1976 (Gordon and Comiso, 1988) and again in 2017. The causes and effects of these polynyas are also visible in other SOSE studies such as Mazloff et al. (2010; their Fig. 2C depicts atmospheric temperature anomalies in the same regions as the polynyas) and Tamsitt et al.

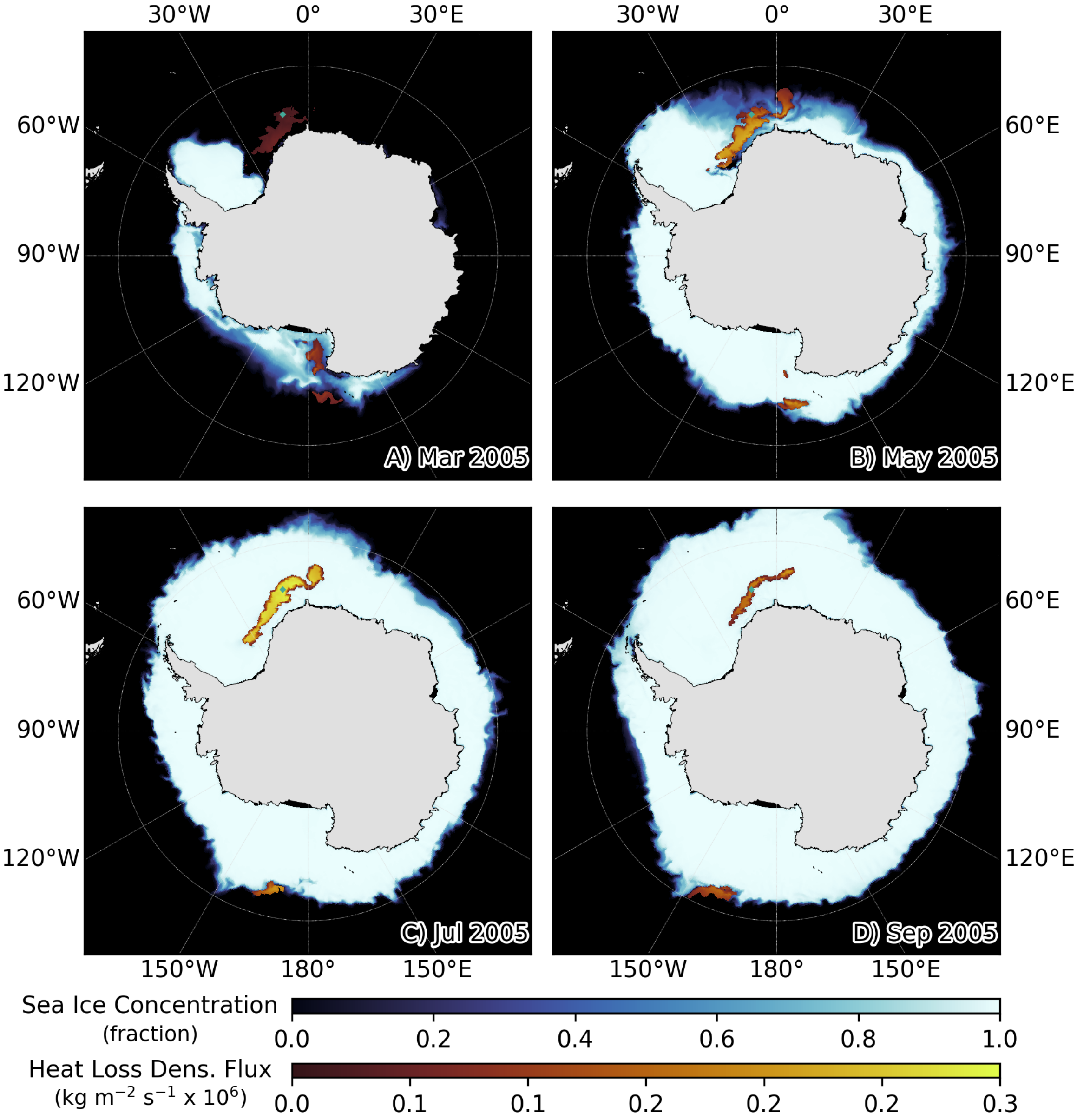
30°W
0°
30°E
60°W
90°W
120°W
60°E
90°E
120°E
150°W
180°
150°E
A) Mar 2005
B) May 2005
C) Jul 2005
D) Sep 2005
Sea Ice Concentration (fraction)
0.0
0.2
0.4
0.6
0.8
1.0
Heat Loss Dens. Flux (kg m^{-2} s^{-1} x 10^{6})
0.0
0.1
0.1
0.2
0.2
0.2
0.3

Figure 4.13: Sea ice concentration and density flux due to heat loss during March, May, July and September, 2005 (austral fall and winter). The areas of heat loss density flux correspond to sensible-heat polynyas and embayments. Similar, but smaller, polynyas and embayments also occur in 2006. The green dot at 67.0416°S, 10.083°W indicates the point at which polynya-induced deep convection occurs for the longest duration during the simulation.

(2016; their Fig. 4A shows significant surface heat loss in the same regions as the polynyas).

The density fluxes in these polynyas are strongest in 2005 and are intense enough to form deep convective plumes which penetrate through the surface layer of AASW and mix CDW up to the sea surface (Fig. 4.14). Moving back to the $T(\theta, S)$ figures, we can see in Fig. 4.10FB that water matching the composition of CDW actually reaches the surface where it is transformed by sensible heat loss; thus relatively warm water is destroyed within the CDW sector and relatively cold water is formed. This highlights the efficacy of the technique: we can detect familiar phenomenon in the model, such as polynyas and see their effects on the $\theta - S$ plane.

Smaller open-ocean polynyas form in the later years of SOSE but the heat loss within them is not intense enough to form deep convection which transforms CDW. There are no significant heat or freshwater gain transformations within the CDW sector, a result which challenges the idea that CDW contributes to an upper branch of the Southern Ocean overturning circulation via heat and freshwater gain.

Subantarctic Mode Water

Since we have demonstrated that SAMW and AAIW are not formed via the transformation of CDW via surface heat and freshwater gain, we turn our attention to describing which fluxes in SOSE are consistent with the observational descriptions of SAMW and AAIW formation. There is a discernible connection between the $\theta - S$ structures of SAMW and the surface waters of the Southern Ocean: water matching SAMW composition forms as a result of heat loss (Fig. 4.10FB) along the densest edge of the Subtropical and Subantarctic Zones at the end of austral winter (Fig. 4.11B). This formation mechanism and seasonality is consistent with McCartney's (1977) original description of SAMW. We also see that the lightest parts of AAIW overlap with the densest parts of SAMW, which is also consistent with McCartney's observation that AAIW is renewed in the late winter from the densest and coldest types of SAMW. We see that no formation occurs via surface fluxes over the remainder of the AAIW sector, suggesting a subsurface process brings about its densification.

Cerovecki and Mazloff (2016) and Abernathey et al. (2016) claim that freshwater fluxes from the melting of sea ice, in particular, play an important role in the formation of SAMW and AAIW (Cerovecki and Mazloff focus their discussion primarily on SAMW). Fig. 4.4 compares the hydrographic extent of this sea ice redistribution freshwater flux with the hydrographic extent of SAMW. We see that SAMW formation and ice melt occur in distinct regions and do not overlap: SAMW

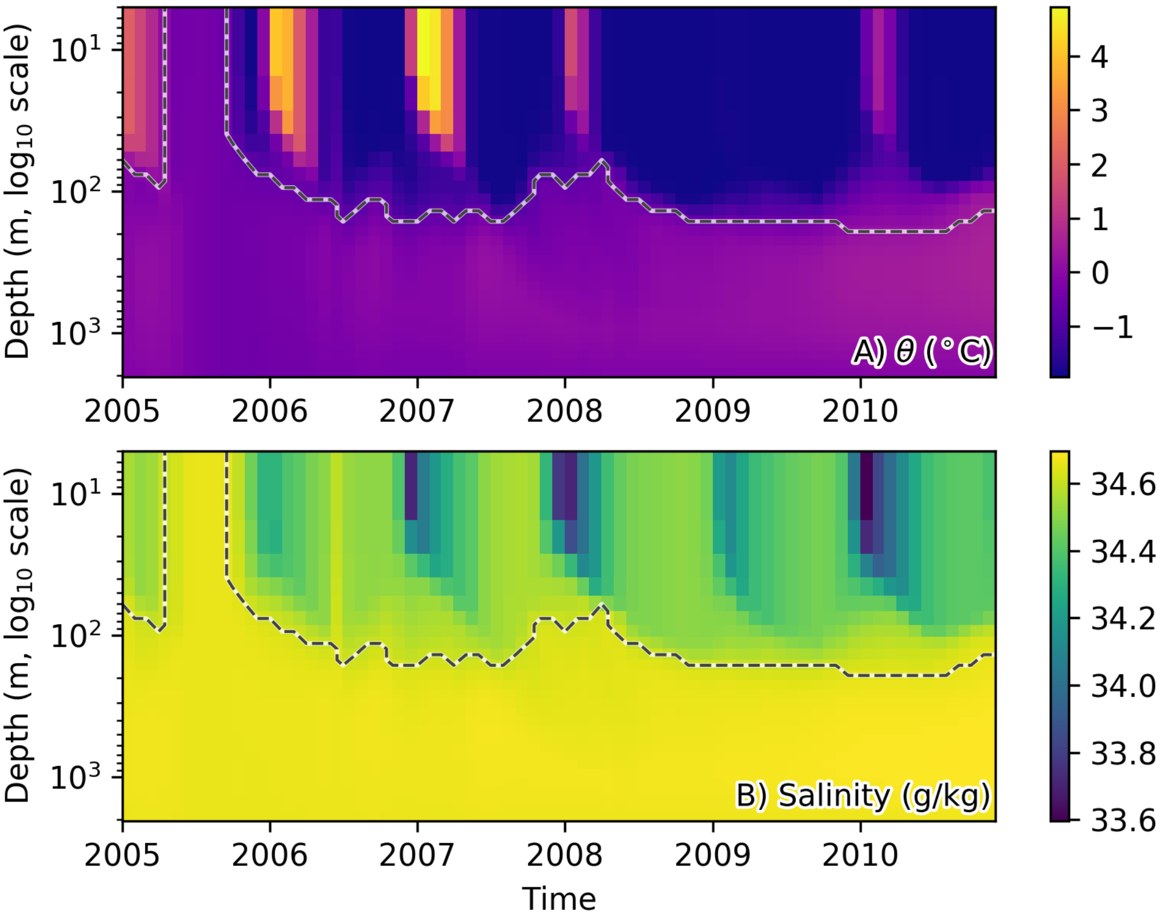

Figure 4.14: A time versus depth (y-axis depicted using $\log_{10}$ scale) plot of θ and S for the point at 67.0416°S, 10.083°W. The dark gray dashed line denotes the extent of CDW, which typically exists beneath the cold and fresh surface layer but reaches the surface from May through September of 2005. A weaker convection event is also visible in 2006 but composition of the surface mixed layer is not warm and salty enough to be considered CDW.

exists north of the PF while the sea ice melt occurs primarily south of the sACCF.

On the $\theta - S$ plane, we see that sea ice formation and melt occur at approximately -1.89°C (Fig. 4.10 TE and TF) while the coldest SAMW is 4°C (McCartney, 1977) and the coldest AAIW is 2°C (Emery and Meincke, 1986). Additionally, peak formation of SAMW occurs in August while peak ice melt occurs in January (Fig. 4.11). It is possible for sea ice to be advected away from its formation region and for the resulting ice melt to flux into warmer waters but Tamura et al. (2011) report that such a strong ocean/sea ice temperature contrast is not observed, which is consistent with the temperature of the ice melt transformations in Fig. 4.10 TE (typically at less than -1°C).

Since the melting of sea ice typically occurs in January, south of the sACCF and into seawater typically colder than 0°C, this ice melt transformation that Cerovecki and Mazloff (2016) and Abernathey et al. (2016) relate to the formation of SAMW and AAIW is actually related to the seasonal formation of Summer Water. Additionally, since sea ice melt flux increases the stability of the water column it cannot directly cause the formation of mode water since increasing mode water volume requires that a surface flux decrease the stability of the water column.

Antarctic Intermediate Water

AAIW rarely reaches the surface in the first three years of SOSE (2005, 2006, and 2007). We see that AAIW does not reach the surface in the P19 transect depicted in Fig. 4.8. However, AAIW often reaches the surface during the colder months of the final three years of SOSE (2008, 2009, and 2010) when convective plumes penetrate from the surface to deeper than 500m depth (we show a representative year, 2008, along the P19 transect in Fig. 4.15). Among the other WOCE transects, these convective plumes also occurred along the P18 transect (105°W) in 2008, 2009 and 2010 as well as on the A21 transect (68°W) in 2008 and 2009.

AAIW exhibits several characteristics which run counter to the description of AAIW one might glean from reading the water mass transformation literature. AAIW does not regularly outcrop. Out of the possible 60 months in the SOSE dataset AAIW only reached the surface for a maximum of 18 months at select grid points. When AAIW does reach the surface, the water mass does not gradually shoal like one might imagine from depictions of isopycnal surfaces. The bulk of the AAIW water mass remains at depth, and a deep convective plume connects this water mass to the surface. This convection is brought about primarily by wintertime heat loss and AAIW is transformed within the plumes to form colder and denser water. The majority of the AAIW sector is

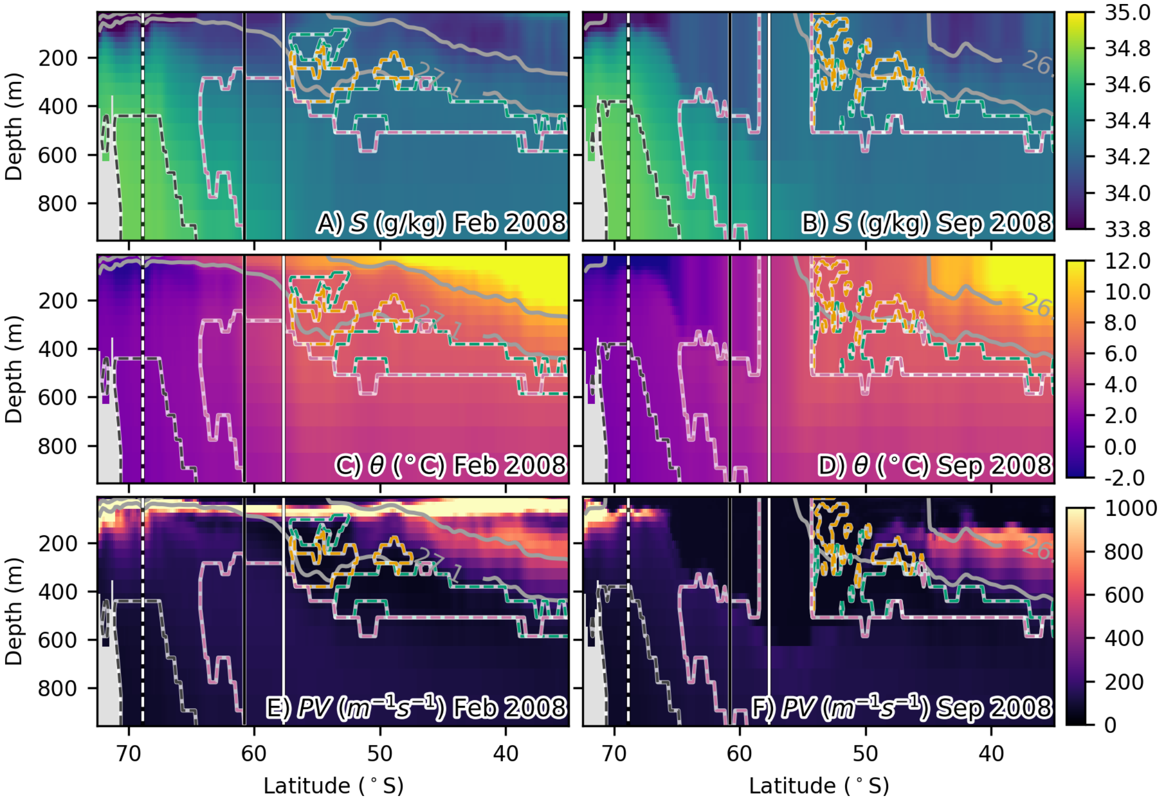

Figure 4.15: Latitude-depth transects along 89°W for February and September 2008. Contours and shading same as in Fig. 4.8. The deep convection mixing AAIW up to the surface is visible in the vicinity of the Subantarctic Front in panels B, D, and F.

not exposed to surface fluxes, which suggests that AAIW is primarily formed via subsurface mixing. This interpretation of the formation process for AAIW contradicts many of the explanations in the water mass transformation literature which conclude that surface fluxes are the dominant mechanism for AAIW formation, e.g. Fig. 13 of Sloyan and Rintoul (2001b), Fig. 17 of Iudicone et al. (2008), Fig. 2d of Abernathey et al. (2016).

4.7.2 Surface Fluxes

An additional discrepancy remains: several studies – Iudicone et al. (2008), Downes et al. (2011), Abernathey et al. (2016) – conclude that transformations from freshwater fluxes are larger in magnitude than transformations from heat fluxes in the Southern Ocean. This conclusion appears to contradict our findings in Fig. 4.10 in which panels TA and TB depict much larger heat transformations than the freshwater transformations in panels TC, TD, TE and TF. The key to resolving this discrepancy is to remember that the one-dimensional $T(\sigma_\theta)$ transformations represent the path integral along an isopycnal in $\theta - S$ space as described in Eq. 4.16. We apply this equation and can replicate the results depicted in Fig. 2 of Abernathey et al. (2016) as shown in our Fig. 4.16. Our Fig. 4.16C depicts the heat transformation partitioned into heat gain and heat loss – its maximum magnitude is roughly three times that of brine rejection and ice melt.

Additionally, the vertical dashed line denotes the 26.75 σ_θ isopycnal, which we also draw in Fig. 4.12. Even though the magnitude of the one-dimensional $T(\sigma_\theta)$ heat transformation in Fig 4.16A is smaller than that of the freshwater transformation at 26.75 σ_θ, we see in Fig. 4.12 that the heat flux transformation has opposite signs at different places along the 26.75 σ_θ isopycnal: the transformation is of negative sign in the Polar Frontal and Antarctic Zones while it is of positive sign in the Subantarctic Zone. Because the $T(\sigma_\theta)$ transformation is the integral along this path, the result of the calculation makes the magnitude of the heat transformations appear smaller than the freshwater transformations even though the $T(\theta, S)$ transformations in Fig. 4.10 show otherwise.

4.7.3 Misconceptions about the Southern Ocean

One might wonder why misconceptions about the Southern Ocean are so pervasive in the literature. We suggest that it is related to the way that the recent literature depicts water masses in this region. Older descriptions do not use density classes to delineate water masses. For example, Sverdrup et al.'s

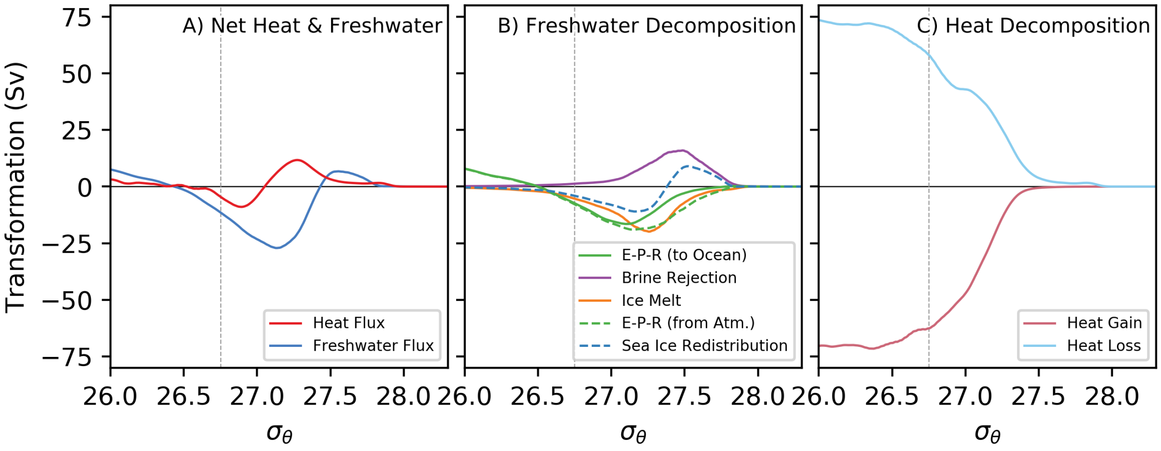

Figure 4.16: One dimensional surface transformations computed by applying Eq. 4.16 to the $T(\theta, S)$ transformations in Fig. 4.10 and applying a smoothing filter since the $T(\theta, S)$ transformations are computed at discrete grid points in the $\theta - S$ plane. Comparing this figure to Fig. 4.10 demonstrates how a mean transformation by a single component does not necessarily represent a conversion from dense water to lighter water (or vice versa) because in the subpolar region the seasonal cycle of heating and cooling is accomplished by different components of the coupled atmospheric, cryospheric and oceanic system.

(1942) depiction of the Southern Ocean in their Fig. 164 uses the 0°C and 2°C isotherms to depict AASW overlying the deeper water masses. These isotherms extend far from the Antarctic continent and separate deeper waters from the surface.

When we contrast Sverdrup et al.'s depiction with the depictions of the Southern Ocean in $T(\sigma_\theta)$ studies – e.g. Fig. 8 of Speer et al. (2000), Fig. 13 of Sloyan and Rintoul (2001b), Fig. 17 of Iudicone et al. (2008), Fig. 8 of Downes et al. (2011), & Fig. 1A of Abernathey et al. (2016) – we see that since the water mass transformation studies use isopycnals rather than isotherms they omit the depiction of AASW. Their depiction also shows lighter water masses as being stacked above denser ones, and water masses outcropping sequentially as a function of density when moving from low to high latitudes.

Even beyond water mass transformation studies, this depiction pervades the recent literature – Table 4.2 lists thirteen studies which replicate Fig. 8 of Speer et al. (2000). Eight of these papers modify the figure before publication and we list the changes made in the third column (excluding mention of superficial changes such as altering the colors in the replicated figure). The widespread replication of Speer et al.'s Fig. 8 within the published literature in spite of its problems is concerning because schematic interpretations can beget wider misconceptions if the schema does not accurately reflect the underlying concepts or data. We must be careful about how we use schematic

Table 4.2: Studies which replicate Fig. 8 of Speer et al. (2000).

Study	*Figure*	*Modifications?*
Rintoul et al. (2001)	Figure 4.6.2	N/A
Olbers and Visbeck (2005)	Figure 1	AAIW downwelling
Hallberg and Gnanadesikan (2006)	Figure 1	N/A
Carter et al. (2008)	Figure 2	N/A
Meredith et al. (2011)	Figure 13	SAMW downwelling
Talley et al. (2011)	Figure 13.4	Include surface water masses – AASW, SASW, STSW and CSW – and depict SAMW as both insulating AAIW from the surface and mixing down into AAIW
Naveira Garabato (2012)	Figure 1c	N/A
Bryden et al. (2012)	Figure 3a	AAIW downwelling
Egan et al. (2013)	Figure 1	SAMW mixes down into AAIW
Sallee et al. (2013)	Figure 1	SAMW downwelling
Post et al. (2014)	Figure 3	SAMW and AAIW downwelling
Gent (2016)	Figure 1	N/A
Deppeler and Davidson (2017)	Figure 3	SAMW and AAIW downwelling

interpretations to depict oceanographic features because the depictions themselves strongly influence how we conceptualize the ocean's circulation and the relationships between water masses.

This is a common problem among scientific disciplines; taxonomy provides a straightforward analogy. The Linnean classification system – which groups species based on similarities in appearance and imposes a hierarchy schema consisting of Kingdom, Phylum, Class, Order, Family, Genus and Species – fails in many instances to reflect the true relationships between species. Linnean taxonomy groups birds and reptiles into distinct classes of animals (Linnaeus, 1758). Yet dinosaurs are reptiles (Owen, 1842) and cladistics reveals that birds are dinosaurs (Gauthier, 1986). There is a contradiction in the schema but the existence of the schema perpetuates a misconception that birds and reptiles are distinct groups of animals. Modern taxonomy employs a different schema, the cladogram, which uses shared derived anatomical features to differentiate species into clades (the number of clades is unlimited) in order to depict the relationships between species more accurately.

We should employ schematic interpretations in oceanography which reflect the complexity of the underlying data in order to describe the relationships between water masses. In taxonomy, the

Linnean hierarchy was supplanted by the cladogram, which uses an unlimited number of clades instead of a fixed amount of levels and adapts to reflect the underlying complexity of species. Likewise, the one-dimensional $T(\sigma_\theta)$ framework should be supplanted by the two-dimensional $T(\theta, S)$ framework since it better distinguishes water masses by using $\theta - S$ composition instead of density and is adaptable to reflect the underlying complexity by using the sector boundaries of a $\theta - S - V$ census rather than density classes.

This improvement would help to correct several misconceptions, including the:

1. lack of awareness of the existence of AASW
2. belief that isopycnal surfaces can adequately delineate water masses, ignoring the seasonal migration of the isopycnals and the longitudinal variation of density within a specific water mass
3. acceptance that UCDW outcrops and is transformed into upper and lower cells rather considering the possibility that the processes which transform SAMW and AAIW are relatively unrelated to the transformation of UCDW.

4.8 Summary

We demonstrate throughout this study that $T(\sigma_\theta)$ water mass transformation studies conflate the cold, fresh waters of AASW with warm, salty subsurface water masses of the same density. These studies reach a number of erroneous conclusions by assuming that surface fluxes transform the subsurface water masses rather than the surface waters which lie atop them.

One of the most pervasive misconceptions is that CDW outcrops and is split into upper and lower branches via surface heat fluxes. The upper branch is assumed to be caused by heat and freshwater gain and leads to the formation of SAMW and AAIW. We demonstrate that CDW does not outcrop broadly in the Southern Ocean. The only process by which CDW is drawn to the surface in SOSE is via mixing related to sensible-heat polynyas in the Weddell and Ross Seas occurring during the first two years of SOSE (2005-2006). While large open-ocean polynyas did not actually form in the vicinity of Antarctica in those years we note that such sensible-heat polynyas would cause CDW to increase in density via surface heat loss and thus would not contribute to an upper branch.

CDW is not transformed by surface heat and freshwater gain and thus is not transformed into SAMW and AAIW. SAMW formation is related to heat loss in the austral winter and the coldest, densest types of SAMW overlap in $\theta - S$ composition with the warmest, lightest types of AAIW, an observation consistent with McCartney's (1977) deductions about AAIW renewal.

Furthermore, many studies conclude that freshwater fluxes dominate heat fluxes in the Southern Ocean. We find the opposite to be true – the effect of heat fluxes on density transformations are generally much larger than freshwater fluxes, with the exception of along the seawater/ice phase transition line. Finally, we speculate on the reason why there are so many widespread misconceptions about the Southern Ocean and suggest that it is partly due to the way that water masses are depicted schematically.

4.9 Chapter Acknowledgements

Funding: This work was completed in collaboration with Dr. Jeff Willison and Professor Ruoying He and was supported by NSF award OPP-14434444. The authors declare no competing financial interests. We thank the developers of MITgcm for enabling creation of SOSE. Additionally, we thank Matthew Mazloff and Ryan Abernathey for providing the data used in this study. Computational resources for SOSE were provided by NSF XSEDE resource grant OCE130007. It can be obtained via the project website http://sose.ucsd.edu. B.K.J. would also like to thank Dr. Frank O. Bryan for his guidance and insightful discussions regarding Walin's water mass transformation framework. The comments from the two reviewers were invaluable and we thank the editor for his patience, as two of the authors moved on to new appointments during the revision process.

Overview and Prospects for Future Research

The completion of a dissertation is often an arduous journey. In my case, I underestimated both the difficulty of the task and the growth that would come about by its fulfilment. I hope my committee will indulge my return to the conversational tone I used in the acknowledgements while I summarize the broad findings of this dissertation and the avenues of future research, since personal context will bring clarity to both of these descriptions.

Throughout my childhood I was taught that the nature of the scientific method involves embracing a state of disbelief in one's own ideas. Initial hunches are to be viewed as hypotheses that should be tested, when possible, using controlled experiments or updated by the introduction of new information that can falsify the original belief. It is almost always the case in oceanography that controlled experiments are not possible, thus the latter technique of using Bayesian inference becomes the necessary route of scientific inquiry.

I attempted to use this technique throughout this dissertation and continue to use it throughout my research. In Chapter 1, for example, it would've been possible to forgo finding Argo floats along each of the eastward and poleward edges of the S_{max} because checking data from the floats risks undermining the narrative of the chapter. However, since we took the risk and found observational results that were clearly consistent with the model, we increased the subjective probability that the narrative is correct.

For this reason, it was disconcerting to read through the peer-reviewed literature cited in Chapter 4...and it was unsettling to write the chapter itself. Nearly all of the analysis in the studies cited in that chapter act only to confirm initial suspicions rather than attempt to falsify hypotheses. This is the critical reason why so many of those studies arrive at erroneous conclusions and why the introduction of new information – seasonality, location, $\theta - S$ composition, or vertical stability – so easily reveals the dubiousness of those findings.

That chapter, in concert with Chapter 3, lead me to the belief – which is either inspiring or dispiriting (maybe both) – that many of the ideas we currently hold in oceanography will not withstand scrutiny. The situation is inspiring in the sense that perhaps there is much yet to discover about the basic structure of the ocean, yet dispiriting in the sense that revealing these discoveries requires illustrating the flaws in our current paradigms and critiquing the work of those whose research is predicated upon these paradigms. It is an unfortunate aspect of the literature that we identify studies by authors' last names because a critique then *appears* to criticize the authors ad hominem rather than criticizing the paradigm itself. I hope that those whose work I critique can see past this superficiality and appreciate that I am trying to help our community pursue more rewarding avenues of research.

One of the most fruitful paths that I am engaged in is combining the techniques of Chapter 1 and Chapter 4 – using $T(\theta, S)$ analysis in conjunction with models equipped to output the diffusivities for individual processes. I used this methodology with Dr. Jeff Willison and Professor Ruoying He at North Carolina State University for a study of continental shelf mixing around Antarctica, a work that is currently in revision.

I also mentioned data assimilation and Bayesian inference in the introduction. One of the ongoing efforts in my position at NCAR is to use ensemble assimilation to diagnose and understand systematic model error in ocean general circulation models. While the models mentioned in this dissertation are relatively high-resolution – we studied POP2 in a 1/10° eddy-resolving configuration and SOSE in a 1/6° eddy-permitting configuration – much of our knowledge about the coupled climate system is predicated upon inferences gleaned from 1° eddy-parameterizing models. Assimilation algorithms have difficulty assimilating observations in such models in the vicinity of western boundary current extensions since systematic model error appears to be prevalent in these regions (Karspeck et al., 2013).

The general technique presented in Chapter 4, where results are compared against water mass census data, should provide a tractable path for understanding such model error. For example, water masses within the model can be compared against a $\theta - S$ census estimated from an observational data set to see whether the model adequately represents a given water mass and, if not, whether the filter increments can adjust the model state to correct the error.

These avenues of research excite me and the initial results are promising. I thank the members of my committee for allowing me the opportunity to defend my dissertation and for providing a rigorous critique of its contents. Finally, to my family: Okage sama de.

Appendix A

Experiment Setup

A.1 Community Earth System Model

The numerical experiment described in Chapters 1 and 2 used CESM version 1.0.4 with active ocean (POP2; Smith et al., 2010) and ice (CICE4; Bailey et al., 2010) components. The grid configuration was T62_t12, which is a spectral atmospheric grid and an eddy-resolving oceanic tripole grid (Murray, 1996) with zonal resolution of 0.1°, meridional resolution of 0.1° cos(lat) and a source modification allowing for 62 vertical levels (10m spacing above 160m and gradually increasing spacing towards the sea floor). The equation of state was computed using the method of McDougall et al. (2003). Freshwater forcing is imposed as a virtual salt flux. Vertical mixing is represented using the KPP mixing scheme of Large et al. (1994). Turbulent shear mixing and double diffusive convection are represented by increasing vertical diffusivity above the background diffusivity. Shear mixing is a function of the gradient Richardson number and salt finger convection is a function of R_ρ according to the empirical parameterization of St. Laurent and Schmitt (1999). In CESM parlance, the experiment used a “G” compset in which the the ocean and ice components of CESM were forced in accordance with the CORE (Griffies et al., 2009) guidelines. The COREv2 dataset is composed of a blend of NCEP reanalysis (Kalnay et al., 1996) and a variety of satellite-based reconstructions of surface atmospheric state and flux fields (Large and Yeager, 2009). COREv2 includes interannually varying forcing data, spanning the years 1948-2009 and a single “normal year” which is an exactly repeating synthetic year derived from the interannually varying data. The interannual dataset incorporates observational and reanalysis data from a variety of sources with irregular start and stop times. In 1979, COREv2 begins incorporating data from MSU (Spencer, 1993), the CMAP product (Xie and Arkin, 1996) and GPCP data (Huffman et al., 1997). Coastal runoff is imposed using the Dai and Trenberth (2002) climatology. The model was initialized with temperature and salinity distributions from the WOCE climatology (Gouretski and Koltermann, 2004) and spun up for 15 model years with COREv2 normal year forcing. This spin up was shared by the experiment described in Bryan and Bachman (2015) but the integrations branched after spinup: Bryan and Bachman continued by extending their integration for another 5 years under normal-year forcing; the integration in this dissertation continued for another 33 years under interannually varying forcing corresponding to the years 1977-2009. Since the transition from normal-year forcing to interannual forcing makes the forcing fields discontinuous, we started the interannual forcing in 1977 to mitigate the effects of these perturbations and suggest that users of this experiment restrict analysis to the output from 1979-2009. Output was saved as five-day averages and converted to monthly averages using a weighted mean.

A.2 Forcing Fields and Availability

The following tables contain the data sources, temporal availability, and units of the variables contained in the COREv2 data set.

Table A.1: The variables and data sources incorporated into the COREv2 data set. This is a modified version of Table 1 of Large and Yeager (2009) updated to reflect the extension of the dataset (Griffies et al., 2012).

Variable	*Source*	*Frequency*	*Duration*	*Resolution*	*Coverage*	*Basis*
SST	Hadley-OI	Monthly	1871-2009	1°	Global	Satellite
Atmos. State	NCEP	6 hourly	1948-2009	T62	Global	NWP
Radiation	ISCCP-FD	Daily	1984-2009	2.5°	Global	Satellite
Precipitation	CPCP	Monthly	1979-2009	2.5°	Global	Satellite
Precipitation	CMAP	Monthly	1979-2009	2.5°	Global	Blend
Precipitation	S-H-Y	Monthly	Climatology	0.5°	50°N-90°N	In situ
Precipitation	MSU	Monthly	1979-1993	2.5°	55°S-55°N	Satellite
Ice fraction	NSIDC	Daily	10/79-2009	25 km	Global Satellite	
All	NOC	Monthly	1980-1995	1°	Global	Ships
All	TAO Daily	1995-2009	2°-20°	Pacific	Buoys	
Most	PIRATA	Daily	1998-2009	2°-20°	Atlantic	Buoys
Vector winds	QSCAT	6 hourly	1999-2009	0.5°	Global	Satellite
Air temperature	POLES	12 hourly	1979-2009	100 km	60°N-90°N	In situ

Table A.2: The forcing fields used in the simulation with their temporal availability and units. This information is a truncated form of Table 1 of Griffies et al. (2012).

Field	*Availability*	*Units*
10 m air density	6 hr x 365 days	kg m^{-3}
Continental runoff	12 months	kg m^{-2} s^{-1}
Liquid precipitation	12 months	kg m^{-2} s^{-1}
Solid precipitation	12 months	kg m^{-2} s^{-1}
Downward longwave radiation	365 days	W m^{-2}
Downward shortwave radiation	365 days	W m^{-2}
10 m specific humidity	6 hr x 365 days	kg kg^{-1}
Sea level pressure	6 hr x 365 days	Pa
10 m air temperature	6 hr x 365 days	K
10 m easterly wind	6 hr x 365 days	m s^{-1}
10 m northerly wind	6 hr x 365 days	m s^{-1}

A.3 POP2 Namelists Groups, Options and Values

The following are all of the namelist groups, included options and their values as set in the pop2_in file for the numerical experiment. Since the particular settings of specific namelist options can have a profound effect on the outcome of a numerical experiment and such namelist files can be lost or corrupted when kept on a filesystem, we reproduce all of the settings in the following tables.

Table A.3: Domain Namelist Group

Variable Name	*Value*
clinic_distribution_type	‘spacecurve’
ew_boundary_type	‘cyclic’
nprocs_clinic	1024
nprocs_tropic	1024
ns_boundary_type	‘tripole’
tropic_distribution_type	‘spacecurve’

Table A.4: IO Namelist Group

Variable Name	*Value*
log_filename	`'/glade/scratch/johnsonb/g.e01.GIAF.T62_t12.003/run/ocn.log.141010-060252'`
lredirect_stdout	.true.
luse_nf_64bit_offset	.true.
luse_pointer_files	.true.
num_iotasks	1

Table A.5: Time_manager Namelist Group

Variable Name	*Value*
accel_file	`'/glade/scratch/johnsonb/g.e01.GIAF.T62_t12.003/run/tx0.1v2_depth_accel'`
allow_leapyear	.false.
date_separator	'-'
dt_count	750
dt_option	'steps_per_day'
dtuxcel	1.0
fit_freq	4
iday0	1
ihour0	6
iminute0	0
imonth0	1
impcor	.true.
isecond0	0
iyear0	1
laccel	.false.
runid	`'g.e01.GIAF.T62_t12.003'`
stop_count	1000
stop_option	'nyear'
time_mix_freq	17
time_mix_opt	'avgfit'

Table A.6: Grid Namelist Group

Variable Name	*Value*
bathymetry_file	‘unknown_bathymetry’
bottom_cell_file	`‘/glade/scratch/dbailey/62_level/dzbc_km62_201209.ieeer8’`
flat_bottom	.false.
horiz_grid_file	`‘/glade/p/cesm/cseg//inputdata/ocn/pop/tx0.1v2/grid/horiz_grid_200709.ieeer8’`
horiz_grid_opt	‘file’
kmt_kmin	3
lremove_points	.false.
n_topo_smooth	0
partial_bottom_cells	.true.
region_info_file	`‘/glade/scratch/johnsonb/g.e01.GIAF.T62_t12.003/run/tx0.1v2_region_ids’`
region_mask_file	`‘/glade/p/cesm/cseg//inputdata/ocn/pop/tx0.1v2/grid/region_mask_20080702.ieeei4’`
sfc_layer_opt	‘varthick’
topography_file	`‘/glade/scratch/dbailey/62_level/topography_km62_201209.ieeei4’`
topography_opt	‘file’
topography_outfile	`‘./g.e01.GIAF.T62_t12.003.pop.h.topography_bathymetry.ieeer8’`
vert_grid_file	`‘/glade/scratch/johnsonb/g.e01.GIAF.T62_t12.003/run/tx0.1v2_vert_grid’`
vert_grid_opt	‘file’

Table A.7: Init_ts Namelist Group

Variable Name	*Value*
init_ts_file	`‘g.e11.G.T62_t12.002.pop.r.0016-01-01-00000.nc’`
init_ts_file_fmt	‘nc’
init_ts_option	‘ccsm_continue’
init_ts_outfile	`‘./g.e01.GIAF.T62_t12.003.pop.h.ts_ic’`
init_ts_outfile_fmt	‘bin’
init_ts_suboption	‘spunup’

Table A.8: Diagnostics Namelist Group

Variable Name	*Value*
cfl_all_levels	.false.
diag_all_levels	.false.
diag_cfl_freq	1
diag_cfl_freq_opt	'nday'
diag_global_freq	1
diag_global_freq_opt	'nday'
diag_outfile	`'/glade/scratch/johnsonb/g.e01.GIAF.T62_t12.003/run/./g.e01.GIAF.T62_t12.003.pop.dd'`
diag_transp_freq	1
diag_transp_freq_opt	'nday'
diag_transport_file	`'/glade/scratch/johnsonb/g.e01.GIAF.T62_t12.003/run/tx0.1v2_transport_contents'`
diag_transport_outfile	`'/glade/scratch/johnsonb/g.e01.GIAF.T62_t12.003/run/./g.e01.GIAF.T62_t12.003.pop.dt'`
diag_velocity_outfile	`'/glade/scratch/johnsonb/g.e01.GIAF.T62_t12.003/run/./g.e01.GIAF.T62_t12.003.pop.dv'`
ldiag_velocity	.false.

Table A.9: Budget_diagnostics Namelist Group

Variable Name	*Value*
ldiag_global_tracer_budgets	.false.

Table A.10: Bsf_diagnostic Namelist Group

Variable Name	*Value*
ldiag_bsf	.false.

Table A.11: Restart Namelist Group

Variable Name	*Value*
even_odd_freq	100000
leven_odd_on	.false.
pressure_correction	.false.
restart_fmt	'nc'
restart_freq	100000
restart_freq_opt	'nyear'
restart_outfile	`'./g.e01.GIAF.T62_t12.003.pop.r'`
restart_start	0
restart_start_opt	'nstep'

Table A.12: Tavg Namelist Group

Variable Name	*Value*
ltavg_has_offset_date	.false. .false.
ltavg_ignore_extra_streams	.false.
ltavg_nino_diags_requested	.false.
ltavg_one_time_header	.false. .false.
ltavg_streams_index_present	.true.
n_tavg_streams	2
tavg_contents	`‘/glade/scratch/johnsonb/g.e01.GIAF.T62_t12.003/run/tx0.1v2_tavg_contents’`
tavg_file_freq	5 5
tavg_file_freq_opt	‘nday’ ’nday’
tavg_fmt_in	‘nc’ ’nc’
tavg_fmt_out	‘nc’ ’nc’
tavg_freq	5 1
tavg_freq_opt	‘nday’ ’nday’
tavg_infile	`‘./g.e01.GIAF.T62_t12.003.pop.hrestart.end’`
tavg_offset_days	2 2
tavg_offset_months	1 1
tavg_offset_years	1 1
tavg_outfile	`‘./g.e01.GIAF.T62_t12.003.pop.h’`
tavg_start	0 0
tavg_start_opt	‘nstep’ ’nstep’
tavg_stream_filestrings	‘nday5’ ’nday1’

Table A.13: History Namelist Group

Variable Name	*Value*
history_contents	`‘/glade/scratch/johnsonb/g.e01.GIAF.T62_t12.003/run/tx0.1v2_history_contents’`
history_fmt	‘nc’
history_freq	1
history_freq_opt	‘never’
history_outfile	`‘./g.e01.GIAF.T62_t12.003.pop.hs’`

Table A.14: Movie Namelist Group

Variable Name	*Value*
movie_contents	`‘/glade/scratch/johnsonb/g.e01.GIAF.T62_t12.003/run/tx0.1v2_movie_contents’`
movie_fmt	‘nc’
movie_freq	1
movie_freq_opt	‘never’
movie_outfile	`‘./g.e01.GIAF.T62_t12.003.pop.hm’`

Table A.15: Solvers Namelist Group

Variable Name	*Value*
convergencecheckfreq	10
convergencecriterion	1.0e-13
maxiterations	1000
preconditionerchoice	‘diagonal’
preconditionerfile	‘unknownPrecondFile’
solverchoice	‘ChronGear’

Table A.16: Vertical_mix Namelist Group

Variable Name	*Value*
aidif	1.0
bottom_drag	1.0e-3
bottom_heat_flx	0.0
bottom_heat_flx_depth	1000.0e2
convect_diff	10000.0
convect_visc	10000.0
convection_type	‘diffusion’
implicit_vertical_mix	.true.
nconvad	2
vmix_choice	‘kpp’

Table A.17: Vmix_const Namelist Group

Variable Name	*Value*
const_vdc	0.25
const_vvc	0.25

Table A.18: Vmix_rich Namelist Group

Variable Name	*Value*
bckgrnd_vdc	0.1
bckgrnd_vvc	1.0
rich_mix	50.0

Table A.19: Tidal Namelist Group

Variable Name	*Value*
local_mixing_fraction	0.33
ltidal_mixing	.false.
mixing_efficiency	0.2
tidal_energy_file	‘unknown_tidal_mixing’
tidal_energy_file_fmt	‘bin’
tidal_mix_max	100.0
vertical_decay_scale	500.0e02

Table A.20: Vmix_kpp Namelist Group

Variable Name	*Value*
bckgrnd_vdc1	0.55
bckgrnd_vdc2	0.303615
bckgrnd_vdc_ban	0.0
bckgrnd_vdc_dpth	2500.0e02
bckgrnd_vdc_eq	0.0
bckgrnd_vdc_linv	4.5e-05
bckgrnd_vdc_psim	0.0
lcheckekmo	.false.
ldbl_diff	.true.
lhoriz_varying_bckgrnd	.false.
linertial	.false.
llangmuir	.false.
lrich	.true.
lshort_wave	.true.
num_v_smooth_ri	1
prandtl	10.0
rich_mix	50.0

Table A.21: Advect Namelist Group

Variable Name	*Value*
tadvect_ctype	‘centered’

Table A.22: Hmix Namelist Group

Variable Name	*Value*
hmix_momentum_choice	‘del4’
hmix_tracer_choice	‘del4’
lsubmesoscale_mixing	.false.

Table A.23: Hmix_del2u Namelist Group

Variable Name	*Value*
am	1.e8
lauto_hmix	.true.
lvariable_hmix	.false.

Table A.24: Hmix_del2t Namelist Group

Variable Name	*Value*
ah	1.e8
lauto_hmix	.false.
lvariable_hmix	.true.

Table A.25: Hmix_del4u Namelist Group

Variable Name	*Value*
am	-27.0e17
lauto_hmix	.false.
lvariable_hmix	.true.

Table A.26: Hmix_del4t Namelist Group

Variable Name	*Value*
ah	-3.0e17
lauto_hmix	.false.
lvariable_hmix	.true.

Table A.27: Hmix_gm Namelist Group

Variable Name	*Value*
ah	3.0e7
ah_bkg_bottom	0.0
ah_bkg_srfbl	3.0e7
ah_bolus	3.0e7
buoyancy_freq_filename	`'/glade/scratch/johnsonb/g.e01.GIAF.T62_t12.003/run/buoyancy_freq'`
buoyancy_freq_fmt	‘nc’
const_eg	1.2
diag_gm_bolus	.false.
gamma_eg	500.0
kappa_depth_1	1.0
kappa_depth_2	0.0
kappa_depth_scale	150000.0
kappa_freq_choice	‘once_a_day’
kappa_isop_choice	‘bfre’
kappa_max_eg	2.0e7
kappa_min_eg	0.35e7
kappa_thic_choice	‘bfre’
read_n2_data	.false.
slm_b	0.3
slm_r	0.3
slope_control_choice	‘notanh’
transition_layer_on	.true.
use_const_ah_bkg_srfbl	.true.

Table A.28: Mix_submeso Namelist Group

Variable Name	*Value*
efficiency_factor	0.07
hor_length_scale	5.0e5
luse_const_horiz_len_scale	.false.
time_scale_constant	8.64e4

Table A.29: Hmix_aniso Namelist Group

Variable Name	*Value*
c_para	8.0
c_perp	8.0
hmix_alignment_choice	'east'
lsmag_aniso	.false.
lvariable_hmix_aniso	.true.
smag_lat	20.0
smag_lat_fact	0.98
smag_lat_gauss	98.0
u_para	5.0
u_perp	5.0
var_viscosity_infile	'ccsm-internal'
var_viscosity_infile_fmt	'bin'
var_viscosity_outfile	`'./g.e01.GIAF.T62_t12.003.pop.hv'`
var_viscosity_outfile_fmt	'nc'
vconst_1	0.6e7
vconst_2	0.5
vconst_3	0.16
vconst_4	2.e-8
vconst_5	3
vconst_6	0.6e7
vconst_7	45.0
visc_para	50.0e7
visc_perp	50.0e7

Table A.30: State Namelist Group

Variable Name	*Value*
state_choice	'mwjf'
state_file	'internal'
state_range_freq	100000
state_range_opt	'enforce'

Table A.31: Baroclinic Namelist Group

Variable Name	*Value*
reset_to_freezing	.false.

Table A.32: Ice Namelist Group

Variable Name	*Value*
ice_freq	100000
ice_freq_opt	'coupled'
kmxice	1
lactive_ice	.true.

Table A.33: Pressure_grad Namelist Group

Variable Name	*Value*
lbouss_correct	.false.
lpressure_avg	.true.

Table A.34: Topostress Namelist Group

Variable Name	*Value*
ltopostress	.false.
nsmooth_topo	0

Table A.35: Forcing_ws Namelist Group

Variable Name	*Value*
ws_data_inc	24.
ws_data_renorm	10., 19*1.
ws_data_type	‘none’
ws_file_fmt	‘bin’
ws_filename	‘unknown-ws’
ws_interp_freq	‘every-timestep’
ws_interp_inc	72.
ws_interp_type	‘linear’

Table A.36: Forcing_shf Namelist Group

Variable Name	*Value*
luse_cpl_ifrac	.true.
shf_data_inc	24.
shf_data_renorm(3)	0.94
shf_data_type	‘monthly’
shf_file_fmt	‘bin’
shf_filename	`‘/glade/p/cesm/cseg//inputdata/ocn/pop/tx0.1v2/forcing/shf_20100318.ieeer8’`
shf_formulation	‘partially-coupled’
shf_interp_freq	‘every-timestep’
shf_interp_inc	72.
shf_interp_type	‘linear’
shf_restore_tau	30.
shf_strong_restore	0.0
shf_strong_restore_ms	92.64
shf_weak_restore	0.

Table A.37: Forcing_sfwf Namelist Group

Variable Name	*Value*
ladjust_precip	.true.
lfw_as_salt_flx	.true.
lms_balance	.false.
lsend_precip_fact	.true.
sfwf_data_inc	24.
sfwf_data_renorm	0.001, 19*1.
sfwf_data_type	‘monthly’
sfwf_file_fmt	‘bin’
sfwf_filename	`‘/glade/p/cesm/cseg//inputdata/ocn/pop/tx0.1v2/forcing/sfwf_mm_PHC2_salx_flxio_20100323.ieeer8’`
sfwf_formulation	‘partially-coupled’
sfwf_interp_freq	‘every-timestep’
sfwf_interp_inc	72.
sfwf_interp_type	‘linear’
sfwf_restore_tau	30.
sfwf_strong_restore	0.0
sfwf_strong_restore_ms	0.6648
sfwf_weak_restore	0.0115

Table A.38: Forcing_pt_interior Namelist Group

Variable Name	*Value*
pt_interior_data_inc	24.
pt_interior_data_renorm	20*1.
pt_interior_data_type	‘none’
pt_interior_file_fmt	‘bin’
pt_interior_filename	‘unknown-pt_interior’
pt_interior_formulation	‘restoring’
pt_interior_interp_freq	‘every-timestep’
pt_interior_interp_inc	72.
pt_interior_interp_type	‘linear’
pt_interior_restore_file_fmt	‘bin’
pt_interior_restore_filename	‘unknown-pt_interior_restore’
pt_interior_restore_max_level	0
pt_interior_restore_tau	365.
pt_interior_variable_restore	.false.

Table A.39: Forcing_s_interior Namelist Group

Variable Name	*Value*
s_interior_data_inc	24.
s_interior_data_renorm	20*1.
s_interior_data_type	‘none’
s_interior_file_fmt	‘bin’
s_interior_filename	‘unknown-s_interior’
s_interior_formulation	‘restoring’
s_interior_interp_freq	‘every-timestep’
s_interior_interp_inc	72.
s_interior_interp_type	‘linear’
s_interior_restore_file_fmt	‘bin’
s_interior_restore_filename	‘unknown-s_interior_restore’
s_interior_restore_max_level	0
s_interior_restore_tau	365.
s_interior_variable_restore	.false.

Table A.40: Forcing_ap Namelist Group

Variable Name	*Value*
ap_data_inc	1.e20
ap_data_renorm	20*1.
ap_data_type	‘none’
ap_file_fmt	‘bin’
ap_filename	‘unknown-ap’
ap_interp_freq	‘never’
ap_interp_inc	1.e20
ap_interp_type	‘nearest’

Table A.41: Coupled Namelist Group

Variable Name	*Value*
coupled_freq	6
coupled_freq_opt	‘nhour’
qsw_distrb_opt	‘const’

Table A.42: Sw_absorption Namelist Group

Variable Name	*Value*
chl_file_fmt	‘bin’
chl_filename	`‘/glade/p/cesm/cseg//inputdata/ocn/pop/tx0.1v2/forcing/chlorophyll_1998-2003_monthly_20080418.ieeer8’`
chl_option	‘file’
jerlov_water_type	3
sw_absorption_type	‘chlorophyll’

Table A.43: Transports Namelist Group

Variable Name	*Value*
lat_aux_begin	-90.0
lat_aux_end	90.0
lat_aux_grid_type	‘southern’
moc_requested	.false.
n_heat_trans_requested	.false.
n_lat_aux_grid	180
n_salt_trans_requested	.false.
n_transport_reg	2
transport_reg2_names	‘Atlantic Ocean’, ’Mediterranean Sea’, ’Labrador Sea’, ’GIN Sea’, ’Arctic Ocean’, ’Hudson Bay’

Table A.44: Context Namelist Group

Variable Name	*Value*
b4b_flag	.false.
lccsm	.true.
lccsm_control_compatible	.false.
lcoupled	.true.

Table A.45: Overflows Namelist Group

Variable Name	*Value*
overflows_diag_outfile	`‘/glade/scratch/johnsonb/g.e01.GIAF.T62_t12.003/run/./g.e01.GIAF.T62_t12.003.pop.do’`
overflows_infile	‘unknown_overflow’
overflows_interactive	.false.
overflows_on	.false.
overflows_restart_type	‘ccsm_continue’
overflows_restfile	`‘./g.e01.GIAF.T62_t12.003.pop.ro’`

Table A.46: Niw Namelist Group

Variable Name	*Value*
lniw_mixing	.false.
niw_boundary_layer_absorption	0.7
niw_energy_file	‘unknown_niw_energy’
niw_energy_file_fmt	‘bin’
niw_energy_type	‘blke’
niw_local_mixing_fraction	0.5
niw_mix_max	100.0
niw_mixing_efficiency	0.2
niw_obs2model_ratio	2.0
niw_vert_decay_scale	2000.0e02

Table A.47: Passive_tracers_on Namelist Group

Variable Name	*Value*
cfc_on	.false.
ecosys_on	.false.
iage_on	.true.
moby_on	.false.

Table A.48: Iage Namelist Group

Variable Name	*Value*
init_iage_init_file	‘same_as_TS’
init_iage_option	‘ccsm_continue’

Bibliography

Abernathey, R. P., I. Cerovecki, P. R. Holland, E. Newsom, M. Mazloff, and L. D. Talley, 2016: Water-mass transformation by sea ice in the upper branch of the Southern Ocean overturning. *Nature Geoscience*, **9**, 596–601, doi:10.1038/ngeo2749, URL http://www.nature.com.prox.lib.ncsu.edu/ngeo/journal/vaop/ncurrent/full/ngeo2749.html?WT.feed_name=subjects_astronomy-and-planetary-science.

Adcroft, A., and Coauthors, 2018: MITgcm User Manual. Tech. rep., MIT Department of EAPS, Cambridge, MA, USA, 1–485 pp.

Aguiar, W., M. M. Mata, and R. Kerr, 2017: On deep convection events and Antarctic Bottom Water formation in ocean reanalysis products. *Ocean Science*, **13 (6)**, 851–872, doi:https://doi.org/10.5194/os-13-851-2017, URL https://www.ocean-sci.net/13/851/2017/.

Alory, G., C. Maes, T. Delcroix, N. Reul, and S. Illig, 2012: Seasonal dynamics of sea surface salinity off Panama: The far Eastern Pacific Fresh Pool. *Journal of Geophysical Research: Oceans*, **117 (C4)**, doi:10.1029/2011JC007802, URL https://agupubs.onlinelibrary.wiley.com/doi/abs/10.1029/2011JC007802.

Ambaum, M. H. P., 2010: Significance Tests in Climate Science. *Journal of Climate*, **23 (22)**, 5927–5932, doi:10.1175/2010JCLI3746.1, URL https://journals.ametsoc.org/doi/full/10.1175/2010JCLI3746.1, publisher: American Meteorological Society.

Anderson, J. L., 1996: A Method for Producing and Evaluating Probabilistic Forecasts from Ensemble Model Integrations. *Journal of Climate*, **9 (7)**, 1518–1530, doi:10.1175/1520-0442(1996)009⟨1518:AMFPAE⟩2.0.CO;2, URL https://journals.ametsoc.org/doi/10.1175/1520-0442%281996%29009%3C1518%3AAMFPAE%3E2.0.CO%3B2.

Bailey, D., M. Holland, E. Hunke, B. Lipscomb, B. Briegleb, C. Bitz, and J. Schramm, 2010: Community Ice CodE (CICE) User's Guide. Tech. rep., National Center for Atmospheric Research, Boulder, CO.

Barnett, T. P., 1984: Prediction of the El Niño of 1982–83. *Monthly Weather Review*, **112 (7)**, 1403–1407, doi:10.1175/1520-0493(1984)112⟨1403:POTENO⟩2.0.CO;2, URL https://journals.ametsoc.org/doi/abs/10.1175/1520-0493(1984)112%3C1403:POTENO%3E2.0.CO;2, publisher: American Meteorological Society.

Bayley, G. V., and J. M. Hammersley, 1946: The "Effective" Number of Independent Observations in an Autocorrelated Time Series. *Supplement to the Journal of the Royal Statistical Society*, **8 (2)**, 184–197, doi:10.2307/2983560, URL http://www.jstor.org/stable/2983560.

Behrens, W. U., 1929: Ein Beitrag zur Fehlerberechnung bei wenigen Beobachtungen. *Landwirtschaftliche Jahrbucher*, Wiegandt & Hempel, Berlin, 807–837.

Benjamini, Y., and Y. Hochberg, 1995: Controlling the False Discovery Rate: A Practical and Powerful Approach to Multiple Testing. *Journal of the Royal Statistical Society. Series B (Methodological)*, **57 (1)**, 289–300, URL https://www.jstor.org/stable/2346101.

Bennett, E. B., 1963: An oceanographic atlas of the Eastern Tropical Pacific Ocean, based on data from EASTROPIC Expedition, October-December 1955. *Inter-American Tropical Tuna Commission Bulletin*, **8 (2)**, 31–161, URL http://aquaticcommons.org/3008/.

Bingham, F. M., G. R. Foltz, and M. J. McPhaden, 2012: Characteristics of the seasonal cycle of surface layer salinity in the global ocean. *Ocean Science*, **8 (5)**, 915–929, doi:10.5194/os-8-915-2012, wOS:000310472500013.

Box, J. F., 1987: Guinness, Gosset, Fisher, and Small Samples. *Statistical Science*, **2 (1)**, 45–52, doi:10.1214/ss/1177013437, URL https://projecteuclid.org/euclid.ss/1177013437.

Boyer, T. P., S. Levitus, J. I. Antonov, R. A. Locarnini, and H. E. Garcia, 2005: Linear trends in salinity for the World Ocean, 1955–1998. *Geophysical Research Letters*, **32 (1)**, L01 604, doi:10.1029/2004GL021791, URL http://onlinelibrary.wiley.com/doi/10.1029/2004GL021791/abstract.

Breusch, T. S., and A. R. Pagan, 1979: A Simple Test for Heteroscedasticity and Random Coefficient Variation. *Econometrica*, **47 (5)**, 1287–1294, doi:10.2307/1911963, URL https://www.jstor.org/stable/1911963.

Brown, R. L., J. Durbin, and J. M. Evans, 1975: Techniques for Testing the Constancy of Regression Relationships over Time. *Journal of the Royal Statistical Society. Series B (Methodological)*, **37 (2)**, 149–192, URL https://www.jstor.org/stable/2984889.

Bryan, F., and S. Bachman, 2015: Isohaline Salinity Budget of the North Atlantic Salinity Maximum. *Journal of Physical Oceanography*, **45 (3)**, 724–736, doi:10.1175/JPO-D-14-0172.1, URL http://journals.ametsoc.org/doi/abs/10.1175/JPO-D-14-0172.1.

Bryden, H. L., C. Robinson, and G. Griffiths, 2012: Changing currents: a strategy for understanding and predicting the changing ocean circulation. *Phil. Trans. R. Soc. A*, **370 (1980)**, 5461–5479, doi:10.1098/rsta.2012.0397, URL http://rsta.royalsocietypublishing.org/content/370/1980/5461.

Cane, M. A., A. C. Clement, A. Kaplan, Y. Kushnir, D. Pozdnyakov, R. Seager, S. E. Zebiak, and R. Murtugudde, 1997: Twentieth-Century Sea Surface Temperature Trends. *Science*, **275 (5302)**, 957–960, doi:10.1126/science.275.5302.957, URL https://science-sciencemag-org.proxy-um.researchport.umd.edu/content/275/5302/957.

Carter, L., I. N. McCave, and M. J. M. Williams, 2008: Circulation and Water Masses of the Southern Ocean: A Review. *Developments in Earth and Environmental Sciences*, F. Florindo, and M. Siegert, Eds., Antarctic Climate Evolution, Vol. 8, Elsevier, 85–114, doi:10.1016/S1571-9197(08)00004-9, URL http://www.sciencedirect.com/science/article/pii/S1571919708000049.

Cerovecki, I., and M. R. Mazloff, 2016: The Spatiotemporal Structure of Diabatic Processes Governing the Evolution of Subantarctic Mode Water in the Southern Ocean. *Journal of Physical Oceanography*, **46 (2)**, 683–710, doi:10.1175/JPO-D-14-0243.1, URL http://journals.ametsoc.org/doi/abs/10.1175/JPO-D-14-0243.1.

Chereskin, T. K., 2005: AAIW 2005: Preliminary Cruise Report. Tech. rep., Scripps Institution of Oceanography, Puenta Arenas, Chile - Puerto Montt, Chile, 1–25 pp.

Cochrane, J. D., 1958: The frequency distribution of water characteristics in the Pacific Ocean. *Deep Sea Research (1953)*, **5 (2)**, 111–127, doi:10.1016/0146-6313(58)90002-9, URL http://www.sciencedirect.com/science/article/pii/0146631358900029.

Dai, A., and K. E. Trenberth, 2002: Estimates of freshwater discharge from continents: Latitudinal and seasonal variations. *Journal of Hydrometeorology*, **3 (6)**, 660–687, doi:10.1175/1525-7541(2002)003⟨0660:EOFDFC⟩2.0.CO;2, wOS:000179814100004.

de Boyer Montégut, C., G. Madec, A. S. Fischer, A. Lazar, and D. Iudicone, 2004: Mixed layer depth over the global ocean: An examination of profile data and a profile-based climatology. *Journal of Geophysical Research: Oceans*, **109 (C12)**, doi:10.1029/2004JC002378, URL http://agupubs.onlinelibrary.wiley.com/doi/abs/10.1029/2004JC002378.

Deacon, G. E. R., 1937a: *The Hydrology of the Southern Ocean*, Discovery Reports, Vol. 15. Cambridge University Press, London.

Deacon, G. E. R., 1937b: *Note on the Dynamics of the Southern Ocean*, Discovery Reports, Vol. 15. Cambridge University Press, London.

Deppeler, S. L., and A. T. Davidson, 2017: Southern Ocean Phytoplankton in a Changing Climate. *Frontiers in Marine Science*, **4**, doi:10.3389/fmars.2017.00040, URL https://www.frontiersin.org/articles/10.3389/fmars.2017.00040/full.

Downes, S. M., A. Gnanadesikan, S. M. Griffies, and J. L. Sarmiento, 2011: Water Mass Exchange in the Southern Ocean in Coupled Climate Models. *Journal of Physical Oceanography*, **41 (9)**, 1756–1771, doi:10.1175/2011JPO4586.1, URL https://journals.ametsoc.org/doi/abs/10.1175/2011jpo4586.1.

Downes, S. M., and Coauthors, 2015: An assessment of Southern Ocean water masses and sea ice during 1988–2007 in a suite of interannual CORE-II simulations. *Ocean Modelling*, **94**, 67–94, doi:10.1016/j.ocemod.2015.07.022, URL http://www.sciencedirect.com/science/article/pii/S1463500315001420.

Draper, N. R., and H. Smith, 1998: *Applied Regression Analysis*. Wiley Series in Probability and Statistics, John Wiley & Sons, Inc., Hoboken, NJ.

Durack, P. J., and S. E. Wijffels, 2010: Fifty-Year Trends in Global Ocean Salinities and Their Relationship to Broad-Scale Warming. *Journal of Climate*, **23 (16)**, 4342–4362, doi:10.1175/2010JCLI3377.1, URL http://journals.ametsoc.org/doi/abs/10.1175/2010JCLI3377.1.

Durack, P. J., S. E. Wijffels, and T. P. Boyer, 2013: Long-term salinity challenges and implications for the global water cycle. *Ocean Circulation and Climate*, G. Siedler, S. M. Griffies, J. Gould, and J. A. Church, Eds., Academic Press, 727–758.

Durbin, J., and G. S. Watson, 1950: Testing for Serial Correlation in Least Squares Regression. I. *Biometrika*, **37 (3-4)**, 409–428, doi:10.1093/biomet/37.3-4.409, URL https://academic.oup.com/biomet/article/37/3-4/409/176531.

Durbin, J., and G. S. Watson, 1951: Testing for Serial Correlation in Least Squares Regression. II. *Biometrika*, **38 (1-2)**, 159–178, doi:10.1093/biomet/38.1-2.159, URL https://academic.oup.com/biomet/article/38/1-2/159/245726.

Egan, K. E., R. E. M. Rickaby, K. R. Hendry, and A. N. Halliday, 2013: Opening the gateways for diatoms primes Earth for Antarctic glaciation. *Earth and Planetary Science Letters*, **375**, 34–43, doi:10.1016/j.epsl.2013.04.030, URL http://www.sciencedirect.com/science/article/pii/S0012821X13002185.

Emery, W. J., and J. Meincke, 1986: Global water masses: summary and review. *Oceanologica Acta*, **9 (4)**, 383–391.

Fisher, R. A., 1935: The Fiducial Argument in Statistical Inference. *Annals of Eugenics*, **6 (4)**, 391–398, doi:10.1111/j.1469-1809.1935.tb02120.x, URL https://onlinelibrary.wiley.com/doi/abs/10.1111/j.1469-1809.1935.tb02120.x.

Gauthier, J., 1986: Saurischian Monophyly and the Origin of Birds. *The Origin of Birds and the Evolution of Flight*, K. Padian, Ed., No. 8, Memoirs of the California Academy of Sciences, California Academy of Sciences, San Francisco, CA, USA, 1–55.

Gent, P. R., 2016: Effects of Southern Hemisphere Wind Changes on the Meridional Overturning Circulation in Ocean Models. *Annual Review of Marine Science*, **8 (1)**, 79–94, doi:10.1146/annurev-marine-122414-033929, URL https://doi.org/10.1146/annurev-marine-122414-033929.

Ghil, M., and Coauthors, 2002: Advanced Spectral Methods for Climatic Time Series. *Reviews of Geophysics*, **40 (1)**, 3–1–3–41, doi:10.1029/2000RG000092, URL https://agupubs.onlinelibrary.wiley.com/doi/abs/10.1029/2000RG000092, _eprint: https://agupubs.onlinelibrary.wiley.com/doi/pdf/10.1029/2000RG000092.

Good, S. A., M. J. Martin, and N. A. Rayner, 2013: EN4: Quality controlled ocean temperature and salinity profiles and monthly objective analyses with uncertainty estimates. *Journal of Geophysical Research: Oceans*, **118 (12)**, 6704–6716, doi:10.1002/2013JC009067, URL https://agupubs.onlinelibrary.wiley.com/doi/abs/10.1002/2013JC009067.

Gordon, A., 1971: Antarctic Polar Frontal Zone. *Antarctic Oceanology I*, J. L. Reid, Ed., No. 15, Antarctic Research Series, American Geophysical Union, Washington, D.C., 205–221.

Gordon, A. L., and J. C. Comiso, 1988: Polynyas in the Southern Ocean. *Scientific American*, **258 (6)**, 90–97, URL http://www.jstor.org/stable/24989126.

Gordon, A. L., and C. F. Giulivi, 2014: Ocean eddy freshwater flux convergence into the North Atlantic subtropics. *Journal of Geophysical Research: Oceans*, **119 (6)**, 3327–3335, doi:10.1002/2013JC009596, URL http://agupubs.onlinelibrary.wiley.com/doi/abs/10.1002/2013JC009596.

Gordon, A. L., C. F. Giulivi, J. Busecke, and F. M. Bingham, 2015: Differences Among Subtropical Surface Salinity Patterns. *Oceanography*, **28 (1)**, 32–39, doi:10.5670/oceanog.2015.02, wOS:000353726500003.

Gouretski, V., and K. P. Koltermann, 2004: WOCE Global Hydrographic Climatology. Tech. Rep. 35, Bundesamtes für Seeschifffahrt und Hydrographie, 52 pp.

Griffies, S., M. Winton, B. Samuels, G. Danabasoglu, S. Yeager, S. Marsland, H. Drange, and M. Bentsen, 2012: Datasets and protocol for the CLIVAR WGOMD Coordinated Ocean-sea ice Reference Experiments. Tech. Rep. 21, WCRP, 21 pp.

Griffies, S. M., and Coauthors, 2009: Coordinated Ocean-ice Reference Experiments (COREs). *Ocean Modelling*, **26 (1)**, 1–46, doi:10.1016/j.ocemod.2008.08.007, URL http://www.sciencedirect.com/science/article/pii/S1463500308001182.

Groeskamp, S., J. D. Zika, T. J. McDougall, B. M. Sloyan, and F. Laliberté, 2014: The Representation of Ocean Circulation and Variability in Thermodynamic Coordinates. *Journal of Physical*

Oceanography, **44 (7)**, 1735–1750, doi:10.1175/JPO-D-13-0213.1, URL https://journals.ametsoc.org/doi/10.1175/JPO-D-13-0213.1.

Gu, D., and S. G. H. Philander, 1997: Interdecadal Climate Fluctuations That Depend on Exchanges Between the Tropics and Extratropics. *Science*, **275 (5301)**, 805–807, doi:10.1126/science.275.5301.805, URL https://science-sciencemag-org.proxy-um.researchport.umd.edu/content/275/5301/805.

Hallberg, R., and A. Gnanadesikan, 2006: The Role of Eddies in Determining the Structure and Response of the Wind-Driven Southern Hemisphere Overturning: Results from the Modeling Eddies in the Southern Ocean (MESO) Project. *Journal of Physical Oceanography*, **36 (12)**, 2232–2252, doi:10.1175/JPO2980.1, URL https://journals-ametsoc-org.prox.lib.ncsu.edu/doi/abs/10.1175/JPO2980.1.

Hanawa, K., and L. D. Talley, 2001: Mode Waters. *Ocean Circulation and Climate : Observing and Modelling the Global Ocean*, G. Siedler, J. Church, and W. J. Gould, Eds., International Geophysics, Vol. 77, Academic Press, San Diego, CA, 373–386.

Hartin, C. A., R. A. Fine, B. M. Sloyan, L. D. Talley, T. K. Chereskin, and J. Happell, 2011: Formation rates of Subantarctic mode water and Antarctic intermediate water within the South Pacific. *Deep Sea Research Part I: Oceanographic Research Papers*, **58 (5)**, 524–534, doi:10.1016/j.dsr.2011.02.010, URL http://www.sciencedirect.com/science/article/pii/S0967063711000549.

Harvey, A. C., and P. Collier, 1977: Testing for functional misspecification in regression analysis. *Journal of Econometrics*, **6 (1)**, 103–119, doi:10.1016/0304-4076(77)90057-4, URL http://www.sciencedirect.com/science/article/pii/0304407677900574.

Hautala, S. L., and D. H. Roemmich, 1998: Subtropical mode water in the Northeast Pacific Basin. *Journal of Geophysical Research: Oceans*, **103 (C6)**, 13 055–13 066, doi:10.1029/98JC01015, URL https://agupubs.onlinelibrary.wiley.com/doi/abs/10.1029/98JC01015.

Held, I. M., and B. J. Soden, 2006: Robust Responses of the Hydrological Cycle to Global Warming. *Journal of Climate*, **19 (21)**, 5686–5699, doi:10.1175/JCLI3990.1, URL https://journals.ametsoc.org/doi/full/10.1175/JCLI3990.1.

Helland-Hansen, B., 1916: Nogen hydrografiske metoder. *Naturforsker möte*, Kristiania (present-day Oslo).

Helm, K. P., N. L. Bindoff, and J. A. Church, 2010: Changes in the global hydrological-cycle inferred from ocean salinity. *Geophysical Research Letters*, **37 (18)**, L18 701, doi:10.1029/2010GL044222, URL http://onlinelibrary.wiley.com.prox.lib.ncsu.edu/doi/10.1029/2010GL044222/abstract.

Hieronymus, M., J. Nilsson, and J. Nycander, 2014: Water Mass Transformation in Salinity–Temperature Space. *Journal of Physical Oceanography*, **44 (9)**, 2547–2568, doi:10.1175/JPO-D-13-0257.1, URL https://journals.ametsoc.org/doi/citedby/10.1175/JPO-D-13-0257.1.

Holte, J., and L. Talley, 2009: A New Algorithm for Finding Mixed Layer Depths with Applications to Argo Data and Subantarctic Mode Water Formation. *Journal of Atmospheric and Oceanic Technology*, **26 (9)**, 1920–1939, doi:10.1175/2009JTECHO543.1, URL http://journals.ametsoc.org.prox.lib.ncsu.edu/doi/abs/10.1175/2009JTECHO543.1.

Hosoda, S., T. Suga, N. Shikama, and K. Mizuno, 2009: Global surface layer salinity change detected by Argo and its implication for hydrological cycle intensification. *Journal of Oceanography*, **65 (4)**, 579, doi:10.1007/s10872-009-0049-1, URL https://link-springer-com.prox.lib.ncsu.edu/article/10.1007/s10872-009-0049-1.

Huffman, G. J., and Coauthors, 1997: The Global Precipitation Climatology Project (GPCP) Combined Precipitation Dataset. *Bulletin of the American Meteorological Society*, **78 (1)**, 5–20, doi:10.1175/1520-0477(1997)078⟨0005:TGPCPG⟩2.0.CO;2, URL https://journals.ametsoc.org/doi/abs/10.1175/1520-0477%281997%29078%3C0005%3ATGPCPG%3E2.0.CO%3B2.

Iudicone, D., G. Madec, B. Blanke, and S. Speich, 2008: The Role of Southern Ocean Surface Forcings and Mixing in the Global Conveyor. *Journal of Physical Oceanography*, **38 (7)**, 1377–1400, doi:10.1175/2008JPO3519.1, URL http://journals.ametsoc.org/doi/abs/10.1175/2008JPO3519.1.

Jackett, D. R., and T. J. McDougall, 1995: Minimal Adjustment of Hydrographic Profiles to Achieve Static Stability. *Journal of Atmospheric and Oceanic Technology*, **12 (2)**, 381–389, doi:10.1175/1520-0426(1995)012⟨0381:MAOHPT⟩2.0.CO;2, URL https://journals.ametsoc.org/doi/10.1175/1520-0426%281995%29012%3C0381%3AMAOHPT%3E2.0.CO%3B2.

Johnson, B. K., F. O. Bryan, S. A. Grodsky, and J. A. Carton, 2016: Climatological Annual Cycle of the Salinity Budgets of the Subtropical Maxima. *Journal of Physical Oceanography*, **46 (10)**, 2981–2994, doi:10.1175/JPO-D-15-0202.1, wOS:000386330000002.

Johnson, G. C., 2006: Generation and Initial Evolution of a Mode Water θ–S Anomaly. *Journal of Physical Oceanography*, **36 (4)**, 739–751, doi:10.1175/JPO2895.1, URL https://journals.ametsoc.org/doi/full/10.1175/JPO2895.1.

Jolliffe, I. T., 2004: P stands for .... *Weather*, **59 (3)**, 77–79, doi:10.1256/wea.132.03, URL https://rmets.onlinelibrary.wiley.com/doi/abs/10.1256/wea.132.03, _eprint: https://rmets.onlinelibrary.wiley.com/doi/pdf/10.1256/wea.132.03.

Joyce, T. M., J. R. Luyten, A. Kubryakov, F. B. Bahr, and J. S. Pallant, 1998: Meso- to Large-Scale Structure of Subducting Water in the Subtropical Gyre of the Eastern North Atlantic Ocean. *Journal of Physical Oceanography*, **28 (1)**, 40–61, doi:10.1175/1520-0485(1998)028⟨0040:MTLSSO⟩2.0.CO;2, URL https://journals.ametsoc.org/doi/full/10.1175/1520-0485%281998%29028%3C0040%3AMTLSSO%3E2.0.CO%3B2.

Kalnay, E., and Coauthors, 1996: The NCEP/NCAR 40-Year Reanalysis Project. *Bulletin of the American Meteorological Society*, **77 (3)**, 437–472, doi:10.1175/1520-0477(1996)077⟨0437:TNYRP⟩2.0.CO;2, URL https://journals.ametsoc.org/doi/abs/10.1175/1520-0477%281996%29077%3C0437%3ATNYRP%3E2.0.CO%3B2.

Karspeck, A. R., S. Yeager, G. Danabasoglu, T. Hoar, N. Collins, K. Raeder, J. Anderson, and J. Tribbia, 2013: An Ensemble Adjustment Kalman Filter for the CCSM4 Ocean Component. *Journal of Climate*, **26 (19)**, 7392–7413, doi:10.1175/JCLI-D-12-00402.1, URL https://journals.ametsoc.org/doi/full/10.1175/JCLI-D-12-00402.1.

Katz, R. W., and B. G. Brown, 1991: The problem of multiplicity in research on teleconnections. *International Journal of Climatology*, **11 (5)**, 505–513, doi:10.1002/joc.3370110504, URL https://rmets.onlinelibrary.wiley.com/doi/abs/10.1002/joc.3370110504.

Kerr, Y., P. Waldteufel, J.-P. Wigneron, J. Martinuzzi, J. Font, and M. Berger, 2001: Soil moisture retrieval from space: the Soil Moisture and Ocean Salinity (SMOS) mission. *IEEE Transactions on Geoscience and Remote Sensing*, **39 (8)**, 1729–1735, doi:10.1109/36.942551.

Kessler, W. S., 2002: Mean Three-Dimensional Circulation in the Northeast Tropical Pacific. *Journal of Physical Oceanography*, **32 (9)**, 2457–2471, doi:10.1175/1520-0485-32.9.2457, URL https://journals.ametsoc.org/doi/full/10.1175/1520-0485-32.9.2457.

Kessler, W. S., 2006: The circulation of the eastern tropical Pacific: A review. *Progress in Oceanography*, **69 (2)**, 181–217, doi:10.1016/j.pocean.2006.03.009, URL http://www.sciencedirect.com/science/article/pii/S0079661106000310.

Kirtman, B. P., 1997: Oceanic Rossby Wave Dynamics and the ENSO Period in a Coupled Model. *Journal of Climate*, **10 (7)**, 1690–1704, doi:10.1175/1520-0442(1997)010⟨1690:ORWDAT⟩2.0.CO;2, URL https://journals.ametsoc.org/doi/full/10.1175/1520-0442%281997%29010%3C1690%3AORWDAT%3E2.0.CO%3B2, publisher: American Meteorological Society.

Kolodziejczyk, N., and F. Gaillard, 2013: Variability of the Heat and Salt Budget in the Subtropical Southeastern Pacific Mixed Layer between 2004 and 2010: Spice Injection Mechanism. *Journal of Physical Oceanography*, **43 (9)**, 1880–1898, doi:10.1175/JPO-D-13-04.1, URL https://journals.ametsoc.org/doi/full/10.1175/JPO-D-13-04.1.

Kolodziejczyk, N., G. Reverdin, and A. Lazar, 2015: Interannual Variability of the Mixed Layer Winter Convection and Spice Injection in the Eastern Subtropical North Atlantic. *Journal of Physical Oceanography*, **45 (2)**, 504–525, doi:10.1175/JPO-D-14-0042.1, URL https://journals.ametsoc.org/doi/10.1175/JPO-D-14-0042.1.

Käse, R. H., W. Zenk, T. B. Sanford, and W. Hiller, 1985: Currents, fronts and eddy fluxes in the Canary Basin. *Progress in Oceanography*, **14**, 231–257, URL http://oceanrep.geomar.de/32814/.

Kållberg, P., P. Berrisford, B. Hoskins, A. Simmons, S. Uppala, S. Lamy-Thépaut, and R. Hine, 2005: ERA-40 Atlas. Tech. Rep. 19, ECMWF, Reading, U.K., 191 pp.

Ladd, C., and L. A. Thompson, 2000: Formation Mechanisms for North Pacific Central and Eastern Subtropical Mode Waters. *Journal of Physical Oceanography*, **30 (5)**, 868–887, doi:10.1175/1520-0485(2000)030⟨0868:FMFNPC⟩2.0.CO;2, URL https://journals.ametsoc.org/doi/full/10.1175/1520-0485%282000%29030%3C0868%3AFMFNPC%3E2.0.CO%3B2.

Large, W., J. Mcwilliams, and S. Doney, 1994: Oceanic Vertical Mixing - a Review and a Model with a Nonlocal Boundary-Layer Parameterization. *Reviews of Geophysics*, **32 (4)**, 363–403, doi:10.1029/94RG01872, wOS:A1994PT55700002.

Large, W. G., and S. G. Yeager, 2004: Diurnal to decadal global forcing for ocean and sea-ice models. Tech. Rep. TN-460+STR, NCAR, Boulder, CO, USA, 1–105 pp.

Large, W. G., and S. G. Yeager, 2009: The global climatology of an interannually varying air–sea flux data set. *Climate Dynamics*, **33 (2-3)**, 341–364, doi:10.1007/s00382-008-0441-3, URL https://link.springer.com/article/10.1007/s00382-008-0441-3.

Leith, C. E., 1974: Theoretical Skill of Monte Carlo Forecasts. *Monthly Weather Review*, **102 (6)**, 409–418, doi:10.1175/1520-0493(1974)102⟨0409:TSOMCF⟩2.0.CO;2, URL https://journals.ametsoc.org/doi/abs/10.1175/1520-0493%281974%29102%3C0409%3ATSOMCF%3E2.0.CO%3B2.

Lindstrom, E., F. Bryan, and R. Schmitt, 2015: SPURS: Salinity Processes in the Upper-ocean Regional Study The North Atlantic Experiment Introduction. *Oceanography*, **28 (1)**, 14–19, doi:10.5670/oceanog.2015.01, wOS:000353726500001.

Linnaeus, C., 1758: *Systema Naturae*. 10th ed., Laurentius Salvius, Stockholm.

Liu, Z., 1994: A Simple Model of the Mass Exchange between the Subtropical and Tropical Ocean. *Journal of Physical Oceanography*, **24 (6)**, 1153–1165, doi:10.1175/1520-0485(1994)024⟨1153:ASMOTM⟩2.0.CO;2, URL https://journals.ametsoc.org/doi/abs/10.1175/1520-0485(1994)024%3C1153%3AASMOTM%3E2.0.CO%3B2.

Livezey, R. E., and W. Y. Chen, 1983: Statistical Field Significance and its Determination by Monte Carlo Techniques. *Monthly Weather Review*, **111 (1)**, 46–59, doi:10.1175/1520-0493(1983)111⟨0046:SFSAID⟩2.0.CO;2, URL http://journals.ametsoc.org/doi/abs/10.1175/1520-0493(1983)111%3C0046%3ASFSAID%3E2.0.CO%3B2.

Lorenz, E. N., 1963: Deterministic Nonperiodic Flow. *Journal of the Atmospheric Sciences*, **20 (2)**, 130–141, doi:10.1175/1520-0469(1963)020⟨0130:DNF⟩2.0.CO;2, URL https://journals.ametsoc.org/doi/abs/10.1175/1520-0469%281963%29020%3C0130%3ADNF%3E2.0.CO%3B2.

Margulies, D., 1993: Assessment of the nutritional condition of larval and early juvenile tuna and Spanish mackerel (Pisces: Scombridae) in the Panamá Bight. *Marine Biology*, **115 (2)**, 317–330, doi:10.1007/BF00346350, URL https://doi.org/10.1007/BF00346350.

Marra, J., P. H. Wiebe, J. K. B. Bishop, and J. C. Stepien, 1987: Primary production and grazing in the plankton of the Panama Bight. *Bulletin of Marine Science*, **40**, 255–270, URL https://www.ingentaconnect.com/content/umrsmas/bullmar/1987/00000040/00000002/art00009.

Marshall, J., A. Adcroft, C. Hill, L. Perelman, and C. Heisey, 1997: A finite-volume, incompressible Navier Stokes model for studies of the ocean on parallel computers. *Journal of Geophysical Research: Oceans*, **102 (C3)**, 5753–5766, doi:10.1029/96JC02775, URL http://onlinelibrary.wiley.com/doi/10.1029/96JC02775/abstract.

Marshall, J., D. Jamous, and J. Nilsson, 1999: Reconciling thermodynamic and dynamic methods of computation of water-mass transformation rates. *Deep Sea Research Part I: Oceanographic Research Papers*, **46 (4)**, 545–572, doi:10.1016/S0967-0637(98)00082-X, URL http://www.sciencedirect.com/science/article/pii/S096706379800082X.

Matalas, N. C., and W. B. Langbein, 1962: Information content of the mean. *Journal of Geophysical Research*, **67 (9)**, 3441–3448, doi:10.1029/JZ067i009p03441, URL http://onlinelibrary.wiley.com.prox.lib.ncsu.edu/doi/10.1029/JZ067i009p03441/abstract.

Mazloff, M. R., P. Heimbach, and C. Wunsch, 2010: An Eddy-Permitting Southern Ocean State Estimate. *Journal of Physical Oceanography*, **40 (5)**, 880–899, doi:10.1175/2009JPO4236.1, URL http://journals.ametsoc.org/doi/abs/10.1175/2009JPO4236.1.

McCartney, M. S., 1977: Subantarctic Mode Water. *A Voyage of Discovery, George Deacon 70th Anniversary Volume*, M. Angel, Ed., Pergamon Press, Oxford, U.K., 103–119.

McCreary, J. P., and P. Lu, 1994: Interaction between the Subtropical and Equatorial Ocean Circulations: The Subtropical Cell. *Journal of Physical Oceanography*, **24 (2)**, 466–497, doi:10.1175/1520-0485(1994)024⟨0466:IBTSAE⟩2.0.CO;2, URL https://journals.ametsoc.org/doi/10.1175/1520-0485%281994%29024%3C0466%3AIBTSAE%3E2.0.CO%3B2.

McDougall, T. J., D. R. Jackett, D. G. Wright, and R. Feistel, 2003: Accurate and Computationally Efficient Algorithms for Potential Temperature and Density of Seawater. *Jour-*

nal of Atmospheric and Oceanic Technology, **20 (5)**, 730–741, doi:10.1175/1520-0426(2003)20⟨730:AACEAF⟩2.0.CO;2, URL http://journals.ametsoc.org/doi/abs/10.1175/1520-0426(2003)20%3C730:AACEAF%3E2.0.CO%3B2.

Meredith, M. P., and Coauthors, 2011: Sustained Monitoring of the Southern Ocean at Drake Passage: Past Achievements and Future Priorities. *Reviews of Geophysics*, **49 (4)**, doi:10.1029/2010RG000348, URL https://agupubs.onlinelibrary.wiley.com/doi/abs/10.1029/2010RG000348.

Monterey, G., and S. Levitus, 1997: Seasonal Variability of Mixed Layer Depth for the World Ocean. NOAA Atlas NESDIS 14, National Oceanic and Atmospheric Administration, Washington, D.C., 102 pp.

Montgomery, R. B., 1958: Water characteristics of Atlantic Ocean and of world ocean. *Deep Sea Research (1953)*, **5 (2)**, 134–148, doi:10.1016/0146-6313(58)90004-2, URL http://www.sciencedirect.com/science/article/pii/0146631358900042.

Mosby, H., 1934: The Waters of the Atlantic Antarctic Ocean. Norwegian Antarctic Expedition 1927-1928 11, Norske Videnskaps-Akademi, Oslo, 131 pp.

Murray, R. J., 1996: Explicit Generation of Orthogonal Grids for Ocean Models. *Journal of Computational Physics*, **126 (2)**, 251–273, doi:10.1006/jcph.1996.0136, URL http://www.sciencedirect.com/science/article/pii/S0021999196901369.

Murtugudde, R., and A. J. Busalacchi, 1998: Salinity effects in a tropical ocean model. *Journal of Geophysical Research: Oceans*, **103 (C2)**, 3283–3300, doi:10.1029/97JC02438, URL https://agupubs.onlinelibrary.wiley.com/doi/abs/10.1029/97JC02438.

Naveira Garabato, A. C., 2012: A perspective on the future of physical oceanography. *Phil. Trans. R. Soc. A*, **370 (1980)**, 5480–5511, doi:10.1098/rsta.2012.0400, URL http://rsta.royalsocietypublishing.org/content/370/1980/5480.

Nicholls, N., 2001: The Insignificance of Significance Testing. *Bulletin of the American Meteorological Society*, **82 (5)**, 981–986.

Nurser, A. J. G., R. Marsh, and R. G. Williams, 1999: Diagnosing Water Mass Formation from Air–Sea Fluxes and Surface Mixing. *Journal of Physical Oceanography*, **29 (7)**, 1468–1487, doi:10.

1175/1520-0485(1999)029⟨1468:DWMFFA⟩2.0.CO;2, URL http://journals.ametsoc.org/doi/abs/10.1175/1520-0485%281999%29029%3C1468%3ADWMFFA%3E2.0.CO%3B2.

Oka, E., and B. Qiu, 2012: Progress of North Pacific mode water research in the past decade. *Journal of Oceanography*, **68 (1)**, 5–20, doi:10.1007/s10872-011-0032-5, URL https://doi.org/10.1007/s10872-011-0032-5.

Olbers, D., and M. Visbeck, 2005: A Model of the Zonally Averaged Stratification and Overturning in the Southern Ocean. *Journal of Physical Oceanography; Boston*, **35 (7)**, 1190–1205, URL https://search.proquest.com/docview/223935313/abstract/4AA2DD722E074044PQ/1.

Orsi, A. H., T. Whitworth, and W. D. Nowlin, 1995: On the meridional extent and fronts of the Antarctic Circumpolar Current. *Deep Sea Research Part I: Oceanographic Research Papers*, **42 (5)**, 641–673, doi:10.1016/0967-0637(95)00021-W, URL http://www.sciencedirect.com/science/article/pii/096706379500021W.

Owen, R., 1842: Report of British Fossil Reptiles. Part II. Tech. Rep. Eleventh Meeting, British Association for the Advancement of Science, London, UK, 60–204 pp.

O'Connor, B. M., R. A. Fine, K. A. Maillet, and D. B. Olson, 2002: Formation rates of subtropical underwater in the Pacific Ocean. *Deep Sea Research Part I: Oceanographic Research Papers*, **49 (9)**, 1571–1590, doi:10.1016/S0967-0637(02)00087-0, URL http://www.sciencedirect.com/science/article/pii/S0967063702000870.

Pollak, M. J., 1958: Frequency distribution of potential temperatures and salinities in the Indian Ocean. *Deep Sea Research (1953)*, **5 (2)**, 128–133, doi:10.1016/0146-6313(58)90003-0, URL http://www.sciencedirect.com/science/article/pii/0146631358900030.

Post, A. L., and Coauthors, 2014: Environmental Setting. *Biogeographic Atlas of the Southern Ocean*, C. De Broyer, P. Koubbi, H. J. Griffiths, B. Raymond, C. d'Udekem d'Acoz, A. Van de Putte, B. Danis, B. David, S. Grant, J. Gutt, C. Held, G. Hosie, F. Huettmann, A. L. Post, and Y. R. Coudert, Eds., 1st ed., Scientific Committee on Antarctic Research, 46–64.

Provost, C., C. Escoffier, K. Maamaatuaiahutapu, A. Kartavtseff, and V. Garçon, 1999: Subtropical mode waters in the South Atlantic Ocean. *Journal of Geophysical Research: Oceans*,

104 (C9), 21 033–21 049, doi:10.1029/1999JC900049, URL http://onlinelibrary.wiley.com/doi/10.1029/1999JC900049/abstract.

Qu, T., S. Gao, and I. Fukumori, 2011: What governs the North Atlantic salinity maximum in a global GCM? *Geophysical Research Letters*, **38 (7)**, doi:10.1029/2011GL046757, URL https://agupubs.onlinelibrary.wiley.com/doi/abs/10.1029/2011GL046757.

Radko, T., 2013: *Double-Diffusive Convection*. Cambridge University Press, Cambridge, England.

Ramsey, J. B., 1969: Tests for Specification Errors in Classical Linear Least-Squares Regression Analysis. *Journal of the Royal Statistical Society. Series B (Methodological)*, **31 (2)**, 350–371, URL https://www.jstor.org/stable/2984219.

Rao, R. R., and R. Sivakumar, 2003: Seasonal variability of sea surface salinity and salt budget of the mixed layer of the north Indian Ocean. *Journal of Geophysical Research: Oceans*, **108 (C1)**, 9–1–9–14, doi:10.1029/2001JC000907, URL https://agupubs.onlinelibrary.wiley.com/doi/abs/10.1029/2001JC000907.

Reverdin, G., E. Kestenare, C. Frankignoul, and T. Delcroix, 2007: Surface salinity in the Atlantic Ocean (30°S–50°N). *Progress in Oceanography*, **73 (3)**, 311–340, doi:10.1016/j.pocean.2006.11.004, URL http://www.sciencedirect.com/science/article/pii/S0079661107000821.

Rintoul, S., R., C. Hughes, W., and D. Olbers, 2001: The Antarctic Circumpolar Current System. *Ocean Circulation and Climate: Observing and Modelling the Global Ocean*, G. Siedler, J. Church, and J. Gould, Eds., Vol. 77, Academic Press, San Diego, CA, 271–302.

Roemmich, D., and Coauthors, 2009: The Argo Program Observing the Global Ocean with Profiling Floats. *Oceanography*, **22 (2)**, 34–43, doi:10.5670/oceanog.2009.36, wOS:000266964200010.

Ruddick, B., 1983: A Practical Indicator of the Stability of the Water Column to Double-Diffusive Activity. *Deep-Sea Research Part a-Oceanographic Research Papers*, **30 (10)**, 1105–1107, doi:10.1016/0198-0149(83)90063-8, wOS:A1983RW85600005.

Saenko, O. A., and A. J. Weaver, 2001: Importance of wind-driven sea ice motion for the formation of Antarctic Intermediate Water in a global climate model. *Geophysical Research Letters*, **28 (21)**, 4147–4150, doi:10.1029/2001GL013632, URL http://onlinelibrary.wiley.com.prox.lib.ncsu.edu/doi/10.1029/2001GL013632/abstract.

Sallee, J.-B., E. Shuckburgh, N. Bruneau, A. J. S. Meijers, T. J. Bracegirdle, Z. Wang, and T. Roy, 2013: Assessment of Southern Ocean water mass circulation and characteristics in CMIP5 models: Historical bias and forcing response. *Journal of Geophysical Research: Oceans*, **118 (4)**, 1830–1844, doi:10.1002/jgrc.20135, URL https://agupubs.onlinelibrary.wiley.com/doi/abs/10.1002/jgrc.20135.

Schmidtko, S., G. C. Johnson, and J. M. Lyman, 2013: MIMOC: A global monthly isopycnal upper-ocean climatology with mixed layers. *Journal of Geophysical Research: Oceans*, **118 (4)**, 1658–1672, doi:10.1002/jgrc.20122, URL https://agupubs.onlinelibrary.wiley.com/doi/abs/10.1002/jgrc.20122.

Schmitt, R., and Coauthors, 2015: From Salty to Fresh—Salinity Processes in the Upper-ocean Regional Study-2 (SPURS-2): Diagnosing the Physics of a Rainfall-Dominated Salinity Minimum. *Oceanography*, **28 (1)**, 150–159, doi:10.5670/oceanog.2015.15, URL https://tos.org/oceanography/article/from-salty-to-freshsalinity-processes-in-the-upper-ocean-regional-study-2-s.

Schmitt, R. W., 1981: Form of the Temperature-Salinity Relationship in the Central Water: Evidence for Double-Diffusive Mixing. *Journal of Physical Oceanography*, **11 (7)**, 1015–1026, doi:10.1175/1520-0485(1981)011⟨1015:FOTTSR⟩2.0.CO;2, URL https://journals.ametsoc.org/doi/abs/10.1175/1520-0485%281981%29011%3C1015%3AFOTTSR%3E2.0.CO%3B2.

Schneider, N., 2004: The Response of Tropical Climate to the Equatorial Emergence of Spiciness Anomalies. *Journal of Climate*, **17 (5)**, 1083–1095, doi:10.1175/1520-0442(2004)017⟨1083:TROTCT⟩2.0.CO;2, URL https://journals.ametsoc.org/doi/full/10.1175/1520-0442%282004%29017%3C1083%3ATROTCT%3E2.0.CO%3B2.

Siedler, G., J. A. Church, and W. J. Gould, Eds., 2001: *Ocean Circulation and Climate*, International Geophysics Series, Vol. 77. Academic Press, London, UK.

Siedler, G., A. Kuhl, and W. Zenk, 1987: The Madeira Mode Water. *Journal of Physical Oceanography*, **17 (10)**, 1561–1570, doi:10.1175/1520-0485(1987)017⟨1561:TMMW⟩2.0.CO;2, URL https://journals.ametsoc.org/doi/abs/10.1175/1520-0485(1987)017%3C1561:TMMW%3E2.0.CO%3B2.

Skliris, N., R. Marsh, S. A. Josey, S. A. Good, C. Liu, and R. P. Allan, 2014: Salinity changes in the World Ocean since 1950 in relation to changing surface freshwater fluxes. *Climate Dynamics*,

43 (3-4), 709–736, doi:10.1007/s00382-014-2131-7, URL https://link-springer-com.prox.lib.ncsu.edu/article/10.1007/s00382-014-2131-7.

Sloyan, B. M., and S. R. Rintoul, 2000: Estimates of Area-Averaged Diapycnal Fluxes from Basin-Scale Budgets. *Journal of Physical Oceanography*, **30 (9)**, 2320–2341, doi:10.1175/1520-0485(2000)030⟨2320:EOAADF⟩2.0.CO;2, URL https://journals-ametsoc-org.prox.lib.ncsu.edu/doi/abs/10.1175/1520-0485(2000)030%3C2320:EOAADF%3E2.0.CO%3B2.

Sloyan, B. M., and S. R. Rintoul, 2001a: Circulation, Renewal, and Modification of Antarctic Mode and Intermediate Water. *Journal of Physical Oceanography*, **31 (4)**, 1005–1030, doi:10.1175/1520-0485(2001)031⟨1005:CRAMOA⟩2.0.CO;2, URL http://journals.ametsoc.org.prox.lib.ncsu.edu/doi/abs/10.1175/1520-0485(2001)031%3C1005:CRAMOA%3E2.0.CO;2.

Sloyan, B. M., and S. R. Rintoul, 2001b: The Southern Ocean Limb of the Global Deep Overturning Circulation. *Journal of Physical Oceanography*, **31 (1)**, 143–173, doi:10.1175/1520-0485(2001)031⟨0143:TSOLOT⟩2.0.CO;2, URL http://journals.ametsoc.org.prox.lib.ncsu.edu/doi/abs/10.1175/1520-0485(2001)031%3C0143:TSOLOT%3E2.0.CO;2.

Sloyan, B. M., L. D. Talley, T. K. Chereskin, R. Fine, and J. Holte, 2010: Antarctic Intermediate Water and Subantarctic Mode Water Formation in the Southeast Pacific: The Role of Turbulent Mixing. *Journal of Physical Oceanography*, **40 (7)**, 1558–1574, doi:10.1175/2010JPO4114.1, URL http://journals.ametsoc.org.prox.lib.ncsu.edu/doi/abs/10.1175/2010JPO4114.1.

Smith, R., and Coauthors, 2010: The Parallel Ocean Program (POP) Reference Manual Ocean Component of the Community Climate System Model (CCSM) and Community Earth System Model (CESM). National Center for Atmospheric Research, URL http://www.cesm.ucar.edu/models/cesm1.0/pop2/doc/sci/POPRefManual.pdf.

Snowden, D. P., and R. L. Molinari, 2003: Subtropical cells in the Atlantic ocean: An observational summary. *Interhemispheric Water Exchange in the Atlantic Ocean*, G. J. Goni, and P. Malanotte-Rizzoli, Eds., Vol. 68, Elsevier Science Bv, Amsterdam, 287–312, wOS:000189295500011.

Speer, K., S. R. Rintoul, and B. Sloyan, 2000: The Diabatic Deacon Cell. *Journal of Physical Oceanography*, **30 (12)**, 3212–3222, doi:10.1175/1520-0485(2000)030⟨3212:TDDC⟩2.0.CO;2, URL http://journals.ametsoc.org.prox.lib.ncsu.edu/doi/abs/10.1175/1520-0485%282000%29030%3C3212%3ATDDC%3E2.0.CO%3B2.

Speer, K., and E. Tziperman, 1992: Rates of Water Mass Formation in the North Atlantic Ocean. *Journal of Physical Oceanography*, **22 (1)**, 93–104, doi:10.1175/1520-0485(1992)022⟨0093:ROWMFI⟩2.0.CO;2, URL http://journals.ametsoc.org/doi/abs/10.1175/1520-0485%281992%29022%3C0093%3AROWMFI%3E2.0.CO%3B2.

Spencer, R. W., 1993: Global Oceanic Precipitation from the MSU during 1979—91 and Comparisons to Other Climatologies. *Journal of Climate*, **6 (7)**, 1301–1326, doi:10.1175/1520-0442(1993)006⟨1301:GOPFTM⟩2.0.CO;2, URL https://journals.ametsoc.org/doi/abs/10.1175/1520-0442%281993%29006%3C1301%3AGOPFTM%3E2.0.CO%3B2.

Sprintall, J., and M. Tomczak, 1993: On the formation of central water and thermocline ventilation in the southern hemisphere. *Deep Sea Research Part I: Oceanographic Research Papers*, **40 (4)**, 827–848, doi:10.1016/0967-0637(93)90074-D, URL http://www.sciencedirect.com/science/article/pii/096706379390074D.

St. Laurent, L., and R. W. Schmitt, 1999: The Contribution of Salt Fingers to Vertical Mixing in the North Atlantic Tracer Release Experiment. *Journal of Physical Oceanography*, **29 (7)**, 1404–1424, doi:10.1175/1520-0485(1999)029⟨1404:TCOSFT⟩2.0.CO;2, URL https://journals.ametsoc.org/doi/10.1175/1520-0485%281999%29029%3C1404%3ATCOSFT%3E2.0.CO%3B2.

Stern, M. E., 1960: The “Salt-Fountain” and Thermohaline Convection. *Tellus*, **12 (2)**, 172–175, doi:10.1111/j.2153-3490.1960.tb01295.x, URL https://onlinelibrary.wiley.com/doi/abs/10.1111/j.2153-3490.1960.tb01295.x.

Student, 1908: The probable error of a mean. *Biometrika*, **6**, 1–25.

Suga, T., and L. D. Talley, 1995: Antarctic Intermediate Water Circulation in the Tropical and Subtropical South Atlantic. *Journal of Geophysical Research: Oceans*, **100 (C7)**, 13 441–13 453, URL https://agupubs.onlinelibrary.wiley.com/doi/abs/10.1029/95JC00858.

Sugimoto, S., and K. Hanawa, 2007: Further evidence for non-reemergence of winter SST anomalies in the North Pacific eastern subtropical mode water area. *Journal of Oceanography*, **63 (4)**, 625–635, doi:10.1007/s10872-007-0055-0, URL https://link-springer-com.prox.lib.ncsu.edu/article/10.1007/s10872-007-0055-0.

Sverdrup, H. U., M. W. Johnson, and R. H. Fleming, 1942: *The Oceans,: Their Physics, Chemistry, and General Biology*. Fifteenth impression edition ed., Prentice-Hall, inc.

Talley, L. D., G. L. Pickard, W. J. Emery, and J. H. Swift, 2011: *Descriptive Physical Oceanography*. 6th ed., Academic Press, San Diego, CA.

Tamsitt, V., L. D. Talley, M. R. Mazloff, and I. Cerovečki, 2016: Zonal Variations in the Southern Ocean Heat Budget. *Journal of Climate*, **29 (18)**, 6563–6579, doi:10.1175/JCLI-D-15-0630.1, URL https://journals-ametsoc-org.prox.lib.ncsu.edu/doi/10.1175/JCLI-D-15-0630.1.

Tamura, T., K. I. Ohshima, S. Nihashi, and H. Hasumi, 2011: Estimation of Surface Heat/Salt Fluxes Associated with Sea Ice Growth/Melt in the Southern Ocean. *SOLA*, **7**, 17–20, doi:10.2151/sola.2011-005, URL https://www.jstage.jst.go.jp/article/sola/7/0/7_0_17/_article.

Tesdal, J.-E., R. P. Abernathey, J. I. Goes, A. L. Gordon, and T. W. N. Haine, 2018: Salinity Trends within the Upper Layers of the Subpolar North Atlantic. *Journal of Climate*, **31 (7)**, 2675–2698, doi:10.1175/JCLI-D-17-0532.1, URL https://journals.ametsoc.org/doi/10.1175/JCLI-D-17-0532.1.

Toyama, K., and T. Suga, 2010: Vertical structure of North Pacific mode waters. *Deep Sea Research Part II: Topical Studies in Oceanography*, **57 (13–14)**, 1152–1160, doi:10.1016/j.dsr2.2009.12.004, URL http://www.sciencedirect.com/science/article/pii/S096706451000007X.

Tseng, Y.-h., and Coauthors, 2016: North and equatorial Pacific Ocean circulation in the CORE-II hindcast simulations. *Ocean Modelling*, **104**, 143–170, doi:10.1016/j.ocemod.2016.06.003, URL http://www.sciencedirect.com/science/article/pii/S146350031630052X.

Tsuchiya, M., 1989: Circulation of the Antarctic Intermediate Water in the North Atlantic Ocean. *Journal of Marine Research*, **47 (4)**, 747–755.

Tsuchiya, M., and L. D. Talley, 1996: Water-property distributions along an eastern Pacific hydrographic section at 135W. *Journal of Marine Research*, **54 (3)**, 541–564, doi:10.1357/0022240963213583.

Tsuchiya, M., and L. D. Talley, 1998: A Pacific hydrographic section at 88°W: Water-property distribution. *Journal of Geophysical Research: Oceans*, **103 (C6)**, 12 899–12 918, doi:10.1029/97JC03415, URL http://onlinelibrary.wiley.com/doi/10.1029/97JC03415/abstract.

Turner, J. S., 1973: *Buoyancy effects in fluids*. Cambridge University Press, Cambridge, England.

Ventura, V., C. J. Paciorek, and J. S. Risbey, 2004: Controlling the Proportion of Falsely Rejected Hypotheses when Conducting Multiple Tests with Climatological Data. *Journal of Climate*, **17 (22)**, 4343–4356, doi:10.1175/3199.1, URL https://journals.ametsoc.org/doi/10.1175/3199.1.

Vossepoel, F. C., and D. W. Behringer, 2000: Impact of Sea Level Assimilation on Salinity Variability in the Western Equatorial Pacific. *Journal of Physical Oceanography*, **30 (7)**, 1706–1721, doi:10.1175/1520-0485(2000)030⟨1706:IOSLAO⟩2.0.CO;2, URL https://journals.ametsoc.org/doi/full/10.1175/1520-0485%282000%29030%3C1706%3AIOSLAO%3E2.0.CO%3B2.

Walin, G., 1977: A theoretical framework for the description of estuaries. *Tellus*, **29 (2)**, 128–136, doi:10.1111/j.2153-3490.1977.tb00716.x, URL https://onlinelibrary.wiley.com/doi/abs/10.1111/j.2153-3490.1977.tb00716.x.

Walin, G., 1982: On the relation between sea-surface heat flow and thermal circulation in the ocean. *Tellus*, **34 (2)**, 187–195, doi:10.1111/j.2153-3490.1982.tb01806.x, URL http://onlinelibrary.wiley.com/doi/10.1111/j.2153-3490.1982.tb01806.x/abstract.

Walker, G., 1914: Correlation in seasonal variations of weather. III. On the criterion for the reality of relationships or periodicities. *Memoirs of the Indian Meteorology Department*, **21 (9)**, 13–15.

Weller, R. A., A. S. Fischer, D. L. Rudnick, C. C. Eriksen, T. D. Dickey, J. Marra, C. Fox, and R. Leben, 2002: Moored observations of upper-ocean response to the monsoons in the Arabian Sea during 1994–1995. *Deep Sea Research Part II: Topical Studies in Oceanography*, **49 (12)**, 2195–2230, doi:10.1016/S0967-0645(02)00035-8, URL http://www.sciencedirect.com/science/article/pii/S0967064502000358.

White, H., 1982: Maximum Likelihood Estimation of Misspecified Models. *Econometrica*, **50 (1)**, 1–25.

Whitworth, T., and W. D. Nowlin, 1987: Water masses and currents of the Southern Ocean at the Greenwich Meridian. *Journal of Geophysical Research: Oceans*, **92 (C6)**, 6462–6476, doi:10.1029/JC092iC06p06462, URL http://onlinelibrary.wiley.com/doi/10.1029/JC092iC06p06462/abstract.

Whitworth, T., A. H. Orsi, S.-J. Kim, W. D. Nowlin, and R. A. Locarnini, 1998: Water Masses and Mixing Near the Antarctic Slope Front. *Ocean, Ice, and Atmosphere: Interactions at the Antarctic*

Continental Margin, S. S. Jacobs, and R. F. Weiss, Eds., American Geophysical Union (AGU), 1–27, doi:10.1029/AR075p0001, URL https://agupubs.onlinelibrary.wiley.com/doi/abs/10.1029/AR075p0001.

Wilks, D. S., 2006: On "Field Significance" and the False Discovery Rate. *Journal of Applied Meteorology and Climatology*, **45 (9)**, 1181–1189, doi:10.1175/JAM2404.1, URL https://journals.ametsoc.org/doi/full/10.1175/JAM2404.1.

Wilks, D. S., 2011: *Statistical Methods in the Atmospheric Sciences*. 3rd ed., No. 100, International Geophysics, Academic Press, Waltham, MA.

Wilks, D. S., 2016: "The Stippling Shows Statistically Significant Grid Points": How Research Results are Routinely Overstated and Overinterpreted, and What to Do about It. *Bulletin of the American Meteorological Society*, **97 (12)**, 2263–2273, doi:10.1175/BAMS-D-15-00267.1, URL https://journals.ametsoc.org/doi/abs/10.1175/BAMS-D-15-00267.1.

Willett, C. S., R. R. Leben, and M. F. Lavín, 2006: Eddies and Tropical Instability Waves in the eastern tropical Pacific: A review. *Progress in Oceanography*, **69 (2)**, 218–238, doi:10.1016/j.pocean.2006.03.010, URL http://www.sciencedirect.com/science/article/pii/S0079661106000322.

Wong, A. P. S., N. L. Bindoff, and A. Forbes, 1998: Ocean-Ice Shelf Interaction and Possible Bottom Water Formation in Prydz Bay, Antarctica. *Ocean, Ice, and Atmosphere: Interactions at the Antarctic Continental Margin*, S. S. Jacobs, and R. F. Weiss, Eds., American Geophysical Union, 173–187, doi:10.1029/AR075p0173, URL http://onlinelibrary.wiley.com/doi/10.1029/AR075p0173/summary.

Wong, A. P. S., and G. C. Johnson, 2003: South Pacific Eastern Subtropical Mode Water. *Journal of Physical Oceanography*, **33 (7)**, 1493–1509, doi:10.1175/1520-0485(2003)033⟨1493:SPESMW⟩2.0.CO;2, URL http://journals.ametsoc.org/doi/full/10.1175/1520-0485%282003%29033%3C1493%3ASPESMW%3E2.0.CO%3B2.

Wong, B., 2011: Points of view: Color blindness. *Nature Methods*, **8 (6)**, 441, doi:doi:10.1038/nmeth.1618.

Worthington, L., 1959: The 18-Degree Water in the Sargasso Sea. *Deep-Sea Research*, **5 (4)**, 297–305, doi:10.1016/0146-6313(58)90026-1, wOS:A1959WU90100005.

Wust, G., 1935: *The Stratosphere of the Atlantic Ocean (1978 Translation)*. Amerind, New Delhi.

Wyrtki, K., 1964: Upwelling in the Costa Rica Dome. *Fishery Bulletin*, **63**, 355–372.

Xie, P., and P. A. Arkin, 1996: Analyses of Global Monthly Precipitation Using Gauge Observations, Satellite Estimates, and Numerical Model Predictions. *Journal of Climate*, **9 (4)**, 840–858, doi:10.1175/1520-0442(1996)009⟨0840:AOGMPU⟩2.0.CO;2, URL https://journals.ametsoc.org/doi/abs/10.1175/1520-0442%281996%29009%3C0840%3AAOGMPU%3E2.0.CO%3B2.

Yeager, S. G., and W. G. Large, 2004: Late-Winter Generation of Spiciness on Subducted Isopycnals. *Journal of Physical Oceanography*, **34 (7)**, 1528–1547, doi:10.1175/1520-0485(2004)034⟨1528:LGOSOS⟩2.0.CO;2, URL http://journals.ametsoc.org/doi/abs/10.1175/1520-0485(2004)034%3C1528%3ALGOSOS%3E2.0.CO%3B2.

You, Y., 2002: A global ocean climatological atlas of the Turner angle: implications for double-diffusion and water-mass structure. *Deep Sea Research Part I: Oceanographic Research Papers*, **49 (11)**, 2075–2093, doi:10.1016/S0967-0637(02)00099-7, URL http://www.sciencedirect.com/science/article/pii/S0967063702000997.

Yu, L., 2011: A global relationship between the ocean water cycle and near-surface salinity. *Journal of Geophysical Research: Oceans*, **116 (C10)**, doi:10.1029/2010JC006937, URL https://agupubs.onlinelibrary.wiley.com/doi/abs/10.1029/2010JC006937.

Yu, L., 2014: Coherent evidence from Aquarius and Argo for the existence of a shallow low-salinity convergence zone beneath the Pacific ITCZ. *Journal of Geophysical Research: Oceans*, **119 (11)**, 7625–7644, doi:10.1002/2014JC010030, URL https://agupubs.onlinelibrary.wiley.com/doi/abs/10.1002/2014JC010030.

Yu, L., 2015: Sea-surface salinity fronts and associated salinity-minimum zones in the tropical ocean. *Journal of Geophysical Research: Oceans*, **120 (6)**, 4205–4225, doi:10.1002/2015JC010790, URL https://agupubs.onlinelibrary.wiley.com/doi/abs/10.1002/2015JC010790.